Evaluation of Gold Nanoparticle-Doxorubicin Conjugates for their Use in Drug Delivery

by

Dennis Curry

A thesis

presented to the University of Waterloo

in fulfillment of the

thesis requirement for the degree of

Master of Science

in

Biology

Waterloo, Ontario, Canada, 2016

AUTHOR'S DECLARATION

I hereby declare that I am the sole author of this thesis. This is a true copy of the thesis, including any required final revisions, as accepted by my examiners.

I understand that my thesis may be made electronically available to the public.

Abstract

Since the seminal work on spherical nucleic acids (SNAs) by Mirkin and co-workers in 1996, substantial research investment has been devoted to gold nanoparticle (AuNP)-based biotechnology advancement. AuNPs have several unique attributes, making them ideal for a wide variety of applications ranging from medicinal diagnostics and cancer therapy to environmental and chemical sensing. First, AuNPs are known to exhibit high surface area-to-volume ratios leading to rapid reaction kinetics and enhanced drug and polymer loading capabilities. Additionally, gold nanoparticles offer a high degree of biocompatibility, controllable synthesis, and near covalent-strength interactions with thiolated molecules. Moreover, gold nanomaterials embody fascinating and unique optical properties derived from the interaction between surface electrons and electromagnetic radiation. By tuning the nanoparticle shape, size and ligand density, these optical properties can be altered, leading to an impressive diversity of technological and medicinal applications.

Doxorubicin is an effective chemotherapeutic used to treat a variety of cancers including solid masses and leukemia. Clinically, its mechanism of action involves the intercalation of double-stranded DNA and the inhibition of important cellular replication enzymes. Typically, doxorubicin is administered in liposomal forms in order to mitigate the harsh cardiotoxicity associated with its use. Despite advances in this field, many side effects still exist and innovative delivery mechanisms remain highly desirable. Drug delivery studies employing doxorubicin often rely on the molecule's fluorescent region for effective quantification, despite previously-reported issues related to non-specific adsorption of the drug molecule to container surfaces.

Here, several research questions related to AuNPs and doxorubicin are addressed. First, the extent to which doxorubicin non-specifically adsorbs to plastic vessels in drug delivery studies is examined and a simple blocking technique using trace amounts of polyethylene glycol is reported and systematically characterized. Through the inclusion of trace amounts of polyethylene glycol in fluorescence measurement buffer, quantitative errors can be inhibited, ensuring accurate drug loading for downstream experimental application. Second, the chemical adsorption mechanism between doxorubicin and AuNPs is systematically studied. Traditionally, the interaction was believed to be dominated by an electrostatic attraction between the protonated moiety of the drug and the negatively-charged citrate-capping agent coating the nanoparticle surface. Here, that theory is challenged upon the proposal of a multifaceted adsorption process, whereby coordination and cation-π-based interactions between the drug and nanoparticle are dominant.

The investigations described above help to advance the fields of nanotechnology and drug delivery by first providing a robust doxorubicin quantification method and second by providing insights into the chemical nature of doxorubicin-gold conjugates. Together, these discoveries may influence future drug delivery research studies that utilize both doxorubicin and gold nanomaterials.

Acknowledgements

Special thanks are owed to my co-supervisors, Dr. Xu Zhang, Dr. Mark Servos and Dr. Ken Oakes for their research expertise, knowledge, understanding, encouragement and compassion. The effect of research on my development as a thinker, rivaled only by philosophy, has been life-changing. I can't thank you enough for taking me on as a student and for providing me with such exciting and invigorating scholastic opportunities. I want to extend particular thanks and consideration to Dr. Zhang for his limitless energy, powerful discussions about both research and life and for constantly reminding and encouraging me to think outside of my system- an ideal I'm working to pursue. I want to thank my committee members- Dr. Brian Dixon of the University of Waterloo, for your feedback, encouragement and support and Dr. Runqing Jiang of the Grand River Cancer Centre for your feedback, expertise and a tremendously exciting introduction to the world of medical physics-one I hope to revisit in some capacity down the road.

Specific to the work presented in Chapter 3 of this document, I want to extend thanks to the Mkandawire Research Group at Cape Breton University for assistance with theoretical and computational modeling and the Liu Lab at the University of Waterloo, particularly Biwu Liu, Dr. Feng Wang and Dr. Juewen Liu for your assistance with nanoparticle synthesis, inspiring discussion and kind nature. In addition I would like to thank Dr. David Irwin of Cape Breton University and the entire Servos Lab at the University of Waterloo, who have been tremendously helpful and inclusive during my stays in Southern Ontario. In terms of Chapter 3, the work was financially supported by Canadian Institutes of Health Research (CIHR), the Nova Scotia Health Research Foundation (NSHRF), the Sydney Tar Ponds Agency, as well as Public Works and

Government Services of Canada (formerly part of ECBC) through grants supporting the Industrial Research Chairs and ACENet undergraduate Fellowship. Finally I would like to thank Dr. Dale Keefe and Judy MacInnis of Cape Breton University for access to FTIR instrumentation. All computational work in Chapter 3 was completed using ACENet and other Compute Canada cluster and facilities.

In terms of funding, I would like to thank the Verschuren Centre for Sustainability in Energy and the Environment at Cape Breton University in Sydney, Nova Scotia as well as the University of Waterloo's Departments of Physics and Biology. I would like to thank the Beatrice Hunter Cancer Research Institute in Halifax, Nova Scotia for a trainee award with funds provided by the Breast Cancer Society of Canada/QEII Foundation/BHCRHI Traineeship for Breast Cancer Research as part of the Cancer Research Training Program. I would like to thank the Waterloo Institute for Nanotechnology (WIN) for the prestigious Nanofellowship Award as well as the Canadian Institutes of Health Research for their support with a Canadian Graduate Scholarship (CGS).

Finally, I wish to thank my family, friends and lab mates- thanks to Bruce MacDonald for your chemistry expertise and philosophical conversation- we can never say it was boring in the lab. Last but not least, great thanks and appreciation to the patient and empowering, Erica Campbell- to whom much of my joy and sanity is owed.

> "The essence of the independent mind lies not in what it thinks, but in how it thinks."
> —Christopher Hitchens, Letters to a Young Contrarian

> "You see, one thing is, I can live with doubt and uncertainty and not knowing. I think it's much more interesting to live not knowing than to have answers which might be wrong."
> — Richard Feynman

Table of Contents

AUTHOR'S DECLARATION ii

Abstract iii

Acknowledgements v

List of Figures x

Chapter 1 General Introduction 1

1.1 Introduction 1

1.2 Nanotechnology 1

1.2.1 Gold Nanoparticles 2

1.3 Cancer 3

1.3.1 Theories of Origin 5

1.3.2 Treatment 7

1.3.3 Impact of Cancer on Canadians 10

1.4 Active and Passive Drug Targeting 11

1.5 Doxorubicin 12

1.5.1 Chemical Structure 12

1.5.2 Applications in Nanomedicine 14

1.6 Polyethylene Glycol 15

1.6.1 Applications in Nanomedicine 15

1.7 Objectives 16

Chapter 2 Prevention of doxorubicin sorptive losses in drug delivery studies using polyethylene glycol 18

2.1 Summary 19

2.2 Introduction 19

2.3 Materials and Methods 21

2.3.1 Chemicals 21

2.3.2 Doxorubicin Adsorption Kinetics and Isotherm 22

2.3.3 Microcentrifuge Tubes 23
2.3.4 Doxorubicin Degradation Studies 23
2.4 Results and Discussion 24
2.4.1 Sorptive Losses of DOX 24
2.4.2 PEG Effect on Sorptive Losses of DOX 26
2.4.3 PEG Effect on DOX Loading on Gold Nanoparticles 30
2.4.4 PEG Effect on Photo-Degradation of DOX 34
2.5 Conclusions 35
Chapter 3 Adsorption of Doxorubicin on Citrate-Capped Gold Nanoparticles: Insights into Engineering Potent Chemotherapeutic Delivery Systems 36
3.1 Summary 37
3.2 Introduction 37
3.2.1 Doxorubicin 37
3.2.2 Gold Nanoparticles 38
3.2.3 Doxorubicin Loading onto Nanoscale Gold 39
3.3 Materials and Methods 41
3.3.1 Chemicals 41
3.3.2 Doxorubicin Quantification 41
3.3.3 Adsorption Kinetics and AuNP Aggregation 42
3.3.4 DOX Adsorption Isotherm 42
3.3.5 Adsorption of DOX Analogs 43
3.3.6 Desorption Studies 44
3.3.7 Citrate Assay 45
3.3.8 Infrared Spectroscopy 45
3.3.9 X-Ray Photoelectron Spectroscopy 46
3.3.10 Transmission Electron Spectroscopy 46
3.3.11 Theoretical Investigations 46

3.4 Results and Discussion 47
3.4.1 Adsorption of DOX on AuNPs 47
3.4.2 Identification of the molecular functionalities contributing to DOX AuNP interaction 54
3.4.3 Modelling of the DOX-AuNP Interaction 57
3.5 Conclusions 64
Chapter 4 Conclusions 66
References 71
Appendix A Supporting Information For Chapter 2 83
Appendix B Supporting Information for Chapter 3 85

List of Figures

Figure 1.1 Near-infrared absorbing hollow gold nanoparticles (left) and commonly-used 13 nm-citrate-capped AuNP (right). TEM images found below respective nanomaterials with scale bars included. 4
Figure 1.2 Nanoparticle deposition within a tumorous environment via the enhanced permeation and retention (EPR) effect. Nanoparticles travel throughout the blood stream and enter the tumor environment through perforations in blood vessels around cancerous tissue. Figure created using components courtesy of Servier (2016). 6
Figure 1.3 Chemical structure of Doxorubicin 13
Figure 1.4 Chemical structure of polyethylene glycol. 15
Figure 2.1 Schematic representation of DOX sorptive losses via non-specific adsorption to plate wells (A) and prevention of non-specific sorptive losses of DOX by inclusion of PEG (B). 25
Figure 2.2 Sorptive losses of doxorubicin to polypropylene micro-centrifuge tubes (A) and polystyrene 96-well plates (B and C). (A) The effect of salt and/or PEG 20K on DOX sorption onto microcentrifuge tube surfaces. In the control tube, no chemicals other than DOX aqueous solution were added. (B) Decrease in the fluorescence of various DOX concentrations (from 0.25 to 3.5 mM) within plate wells over time; (C) the Langmuir isotherm for non-specific sorption to plate-well surfaces. 27
Figure 2.3 The effects of PEG (various concentrations and molecular weights) on DOX adsorption onto 96 well plate surfaces. In the control wells, no chemicals other DOX aqueous solution were added. 29
Figure 2.4 Comparison of several surface-blocking agents with 10% (v/v) ethylene glycol and ethanol. In the control wells, no chemicals other than DOX aqueous solution were added. 32
Figure 2.5 Inhibition of DOX loading to AuNPs by several surface blocking reagents (BSA, Triton X-100, Tween 20, and PEG 20K). AuNPs were introduced after 240 s; no surface blocking agents were added to control wells. 33
Figure 2.6 Relative effectiveness of surface-blocking agents as assessed by monitoring DOX fluorescence in plate wells pre-coated with the various surface-blocking agents. 33
Figure 2.7 DOX photodegradation kinetics in solutions containing various concentrations of PEG 20K. The control sample was not exposed to blue light. 35
Figure 3.1 Schematic highlighting the various techniques used to load DOX to AuNP in drug delivery systems. 40
Figure 3.2 (A) DOX–AuNP isotherm including Langmuir Fit (solid line). See Fig. S7A† for original data with standard errors. (B) DOX fluorescence decrease upon addition of AuNP. 48
Figure 3.3 Citrate displacement from AuNP surface upon addition of DOX. 50
Figure 3.4 Adsorption of DOX onto AuNP in presence of varying NaCl concentrations (A) and pH environments (B) 51

Figure 3.5 DOX desorption from AuNP in presence of varying pH (A), solvent (B) and thermal (C) conditions. (D) DOX desorption from AuNP upon addition of competitive molecules ([Glu], [urea] = 45 mM, [GSH] = 182 μM. 53
Figure 3.6 Chemical compounds used in this work mimicking potential DOX functional groups of interest in AuNP adsorption. 55
Figure 3.7 (A) Fluorescence intensity of DOX from DOX–AuNP conjugates upon addition of anthracene. (B) Fluorescence intensity of compounds structurally analogous or with relevant functional groups to DOX molecules upon addition of AuNP. 56
Figure 3.8 (A) Structure of doxorubicin and (B) Doxorubicin with gold nanoparticles. 59
Figure 3.9 The IR spectrum showing the peak shifts in DOX in ground state at room temperature (A), excited state with increased temperature (B) and DOX–AuNP conjugates (C). Features are labelled in the figure. 60
Figure 3.10 (A) Electrostatic interaction (+-) and hydrogen bonding (—) between adsorbed citrate and adsorbed DOX molecules on AuNP surfaces. (B) Hydrogen bonding between adsorbed DOX molecules on AuNP surface. (C) Cation–π and coordination chemistry between DOX and AuNP. 62
Figure 3.11 BSA (A) and GSH (B) induced DOX fluorescence signal increase via desorption from AuNP surface. 63
Figure 4.1 Effect of reagent addition order on DOX adsorption and DOX-AuNP stability..... 68
Figure 4.2 Effect of PEG polymer length on DOX adsorption and DOX-AuNP stability. 69
Figure A.1 The effect of PEG 4K and PEG 8K (various concentrations) on DOX adsorption to plate-well surfaces. In control wells, no chemicals other than DOX aqueous solution were added. 83
Figure A.2 Comparison of DOX adsorption onto AuNP in the presence and absence of 10 ppm PEG 20K. AuNP-DOX conjugates were dissolved with 2 uL of 1 M KCN solution into 100 uL of AuNP-DOX solution with released DOX quantified by fluorescence. The data demonstrate no significant impact of PEG 20K on DOX loading to AuNP (p=0.065; one-way ANOVA). 83
Figure A.3 Optical absorbance of 1% PEG 20K in 5 mM HEPES buffer..... 84
Figure B.1 AuNP absorbance spectra upon addition of increasing [DOX] (Inset: AuNP color change upon addition of DOX, DOX:AuNP molar concentration ratio from right to left: 0, 385, 769, 1538). 85
Figure B.2 TEM micrograph of ~13 nm citrate-capped AuNP used in this work using TEM (above) and HR-TEM (bottom). (Scale bars included in figures). 86
Figure B.3 TEM micrograph of DOX-AuNP conjugates. DOX:AuNP molar concentration ratio = 307:1 (Scale bar: 20 nm). 87
Figure B.4 TEM micrograph of DOX-AuNP conjugates. DOX:AuNP molar concentration ratio = 307:1 (Scale bar: 200 nm). 87
Figure B.5 Citrate displaced per AuNP quantified via DOX fluorescence signal measured in supernatant solution ($p<0.5$). 88
Figure B.6 FTIR spectra of DOX-AuNP conjugate and AuNP. 88

Figure B.7 (A)Original DOX-AuNP loading isotherm including standard error bars. (B) Desorption of DOX from AuNP surface after treatment with MgCl2 ([62.5 mM]), EtOH (31.25% v/v) and EtOH-MgCl2. DOX:AuNP ratio = 317:1. (C) Adsorption of DOX to AuNP surface after EDTA ([3.84 µM]) treatment of AuNP. DOX:AuNP ratio = 308:1. 89
Figure B.8 XPS N 1s (A) and C 1s (B) deconvoluted spectra for DOX-AuNP conjugate solutions. 90
Figure B.9 Molecular orbital (MO) of DOX showing localised electron sites in (A) first excited and (B) ground states. The first excited state is sampled between 200 - 400 °K at the PM7 level of theory in MOPAC2012 with PCM water. The first 6 energy level state of the alpha orbital are displayed. The ground state MO of the HOMO is located at the first benzene ring, which is the highly hydrophobic region of DOX. In contrast, the MO of LUMO is delocalised around the hydrophobic site of DOX. At HUMO 1, the -OH group is involved in MO while in HUMO 4 the carbonyl contributed to the delocalisation of the MO. In LUMO 1, the MO was delocalized from the ring 4 containing -OH to the ring 1. However, LUMO 4 MO does not involve a hydrophobic electronic site. This suggests a possible transition that involves either the carbonyl or the hydroxyl functional group. Regarding the particular transition of HOMO 1 to LUMO 1, the MO migrated from -OH site to C=O site. Moreover, the delocalisation of the MO of the hydrophobic site (ring 30) to the acceptor hydrophobic site at the rings 1 and 2. However, HOMO 4 showed a migration of MO from hydrophobic electronic transition to a localised highly electrophilic site. The HOMO 5 displayed the MO delocalised around the hydrophobic electronic sites in ring 1, 2 and 3 towards HOMO 5 localised electrophilic site. The main observation was the absence of MO in ring 5 ground state HOMO to LUMO 5. The thermochemistry calculation demonstrated the contribution of the ring 5 (ether) in the electronic transition is an intra-thermochemistry reaction that involved the amine functional group. As for the ground state, the hydrophobic electronic transitions are partially delocalized. 91
Figure B.10 (A) Modelling of IR spectrum of DOX without ring 1 connected to amine moiety with a 0.5 nm AuNP. (B) Modelling of IR spectrum of the DOX-like anthracene with 0.5 nm AuNP 92
Figure B.11 Calculation of electrostatic potential of the surface at PM7 level of theory: (A) DOX-like anthracene-AuNP, and (B) DOX without ring 1 AuNP. The potential energy surface of the last 1ns of 12 ns MD demonstrated DOX bent and formed an Au-N bond (Model 1). Further QM calculation of DOX alone with high level of theory in gas phase as well as with continuum water (B3LYP/6-31G(d)) had depicted a bent formation. Increasing the theory level did not change the bend. This highlights the hypothesis that the bent formation between ring 5 containing N and the ring 1 to 4 may be due to the π - σ attraction that dominated the edge to face interaction (Hunter and Sanders, 1990). Therefore, the bending of ring 5 is likely to be independent of the presence of AuNP. To refine the interaction mechanism between DOX – AuNP, we further analysed two models, model 2 was DOX lacking ring 5, which provided insight of the carbonyl interaction with the AuNP surface. 93

Chapter 1 General Introduction

1.1 Introduction

Within the research field of nanotechnology, the feasible delivery of potent chemotherapeutics using nanomaterials has received a substantial amount of interest in recent years. Doxorubicin (DOX) is a frontline anthracycline chemotherapeutic used to treat a variety of cancers including lung, breast and ovarian forms (Duggan and Keating, 2011; Green and Rose, 2006; Lv et al., 2014). Its effectiveness has stood the test of time, being discovered in the 1950's, approved for clinical use by the Food and Drug Administration (FDA) over 30 years ago and still finding applicability in chemotherapeutic cocktails and research laboratories today (Judson et al.; Prados et al., 2012).

Of the nanomaterials currently being surveyed for utility in clinical drug delivery system development, gold nanoparticles have become ubiquitous. Since the seminal work of Mirkin and co-workers on spherical nucleic acid (SNA) development, numerous research groups have built expertise in using nano-sized gold spheres and rods to combat disease and fast track diagnostics (Akiyama et al., 2009; Mirkin et al., 1996; Williams, 2013). This thesis contributes to advancing the field of nanotechnology by focusing on gold nanoparticle-based therapeutics and targeting platforms for use in the treatment of cancer.

1.2 Nanotechnology

Under the broad umbrella of biomedical research lies the field of nanotechnology and specifically within the context of cancer treatment, nanomedicine, where nanoscale

systems are developed and manipulated to kill cancer cells and tissues. Over the course of the past two decades, nanoparticle-related research has seen the development of several novel drug delivery system designs and continued future investment will undoubtedly help to fully realize the potential nanoscale applications have in medicine (Chen et al., 2011). Nanomaterials are generally defined as those between 1-100 nm; however, drug delivery carriers and nanosensors are often larger in size (Liu et al., 2012; Rengan et al., 2014).

1.2.1 Gold Nanoparticles

Gold nanoparticles (AuNP) are aqueous suspensions of nano-sized gold core particles that are extensively used in the field of nanotechnology research. Their ease and control of synthesis, optical properties, biocompatibility and high surface area to volume ratios make their use in biotechnology and drug delivery increasingly attractive. Traditional spherical AuNP are most commonly synthesized by the routine citrate-reduction method popularized over 40 years ago, (Frens, 1973) where gold salt is boiled before the addition of citric acid solution. Upon citrate addition, the solution changes from a yellow color to wine red over the course of ~ 15-30 minutes, signifying the growth of nanometer-sized gold particles. By altering the concentrations of the reagents in the reaction, the size and concentration of the prepared nanoparticles can be tuned with precise control. Upon competition, the as-synthesized particles are capped by the negatively-charged citrate ions used to reduce the gold salt. These ions provide repulsive electrostatic stabilization of the nanoparticles in solution. Changes in the solution properties such as increasing ionic strength or varying pH will screen the negative charges on the surface of the particles and cause rapid and irreversible aggregation

witnessed by wine red to blue color change and a shift in the optical absorbance of the nanoparticle solution. This instability, or aggregation, leads to the clumping of nanoparticles in solution, driven by van der Waals interactions between the dense cores of the nanoparticles.

At the nanoscale, unique physical phenomena allow for the development of useful biomedical systems. For example, the ways in which surface electrons on gold nanoparticles of different shapes and morphologies interact with light to produce surface plasmon resonance (SPR) effects have formed the basis of commercialized disease-diagnostic systems (Figure 1.1). Nano-sized delivery systems rely on the enhanced permeation and retention (EPR) effect (Figure 1.2) *in vivo*, whereby nanoconjugates <200 nm in size are optimal for particle deposition from leaky vasculature into the tumor microenvironment (Kobayashi et al., 2014). Therefore, considerations such as size, stability and biocompatibility are of the utmost importance when designing nanoscale drug delivery systems and much effort is being spent designing optimal systems within the field today (Farokhzad and Langer, 2009).

1.3 Cancer

In broad terms, cancer is defined as the uncontrollable division and proliferation of cells within the body. Eventually these abnormal cells form masses known as tumors, which can lead to disturbances in organ function and death if left untreated. In reality, the disease is much more complicated than this general definition suggests. In 2000, Hanahan and Weinberg published their seminal work entitled, *The Hallmarks of Cancer* (Hanahan and Weinberg, 2000). The authors identify six landmark features to better explain the

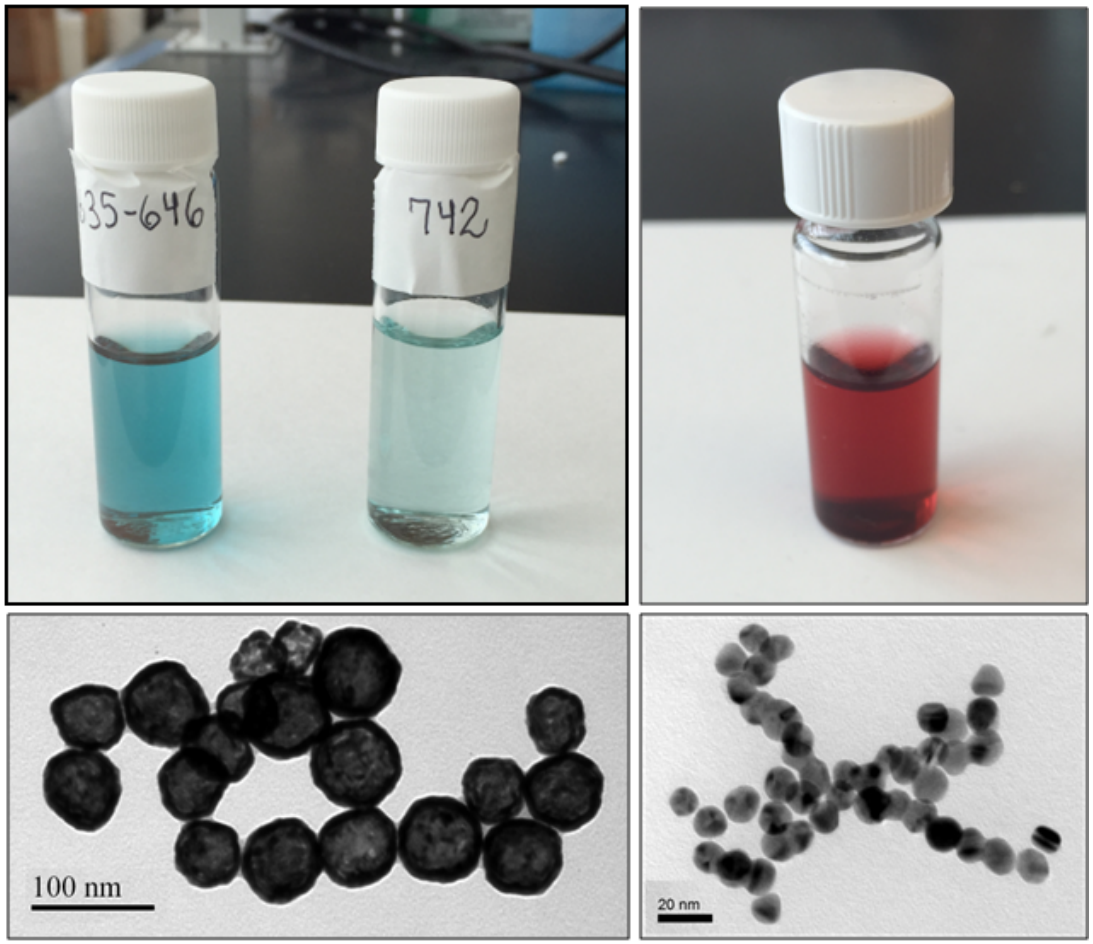

Figure 1.1 Near-infrared absorbing hollow gold nanoparticles (left) and commonly-used 13 nm-citrate-capped AuNP (right). TEM images found below respective nanomaterials with scale bars included.

intricacies associated with a disease encompassing over 200 varieties. In 2011, the authors updated their work in light of a decade of scientific advancement in the understanding and characterization of each of the six hallmarks: sustaining proliferative signaling, evading growth suppressors, activating invasion and metastasis, enabling replicative immortality, inducing angiogenesis and resisting cell death (Hanahan and Weinberg, 2011). The extent to which each of these hallmarks is propagated in the body correlates strongly with the overall success and progression of cancer.

1.3.1 Theories of Origin

One well-supported hypothesis describing the nature of the disease is known as the monoclonal theory of cancer origin. Under this theory, cancer is understood as the product of compounding mutations in a normal cell lineage which are referred to as clonal expansions (Weinberg, 2014). These mutations, being passed from one generation to the next, allow for increased fitness relative to non-mutated populations. After a specific number and combination of mutations is acquired, a malignant status is reached. Recent advances in cancer stem cell (CSC) theory have underscored the complexity associated with cancer origins (Kalluri and Weinberg, 2009). Research has shown that only a very low percentage of transplanted tumor cells are actually able to form tumors in a new host organism (Bonnet and Dick, 1997). These results provide evidence of the existence of tumorigenic CSCs among neoplastic cell populations and have driven investment in CSC-specific therapeutic research (Gupta et al., 2009).

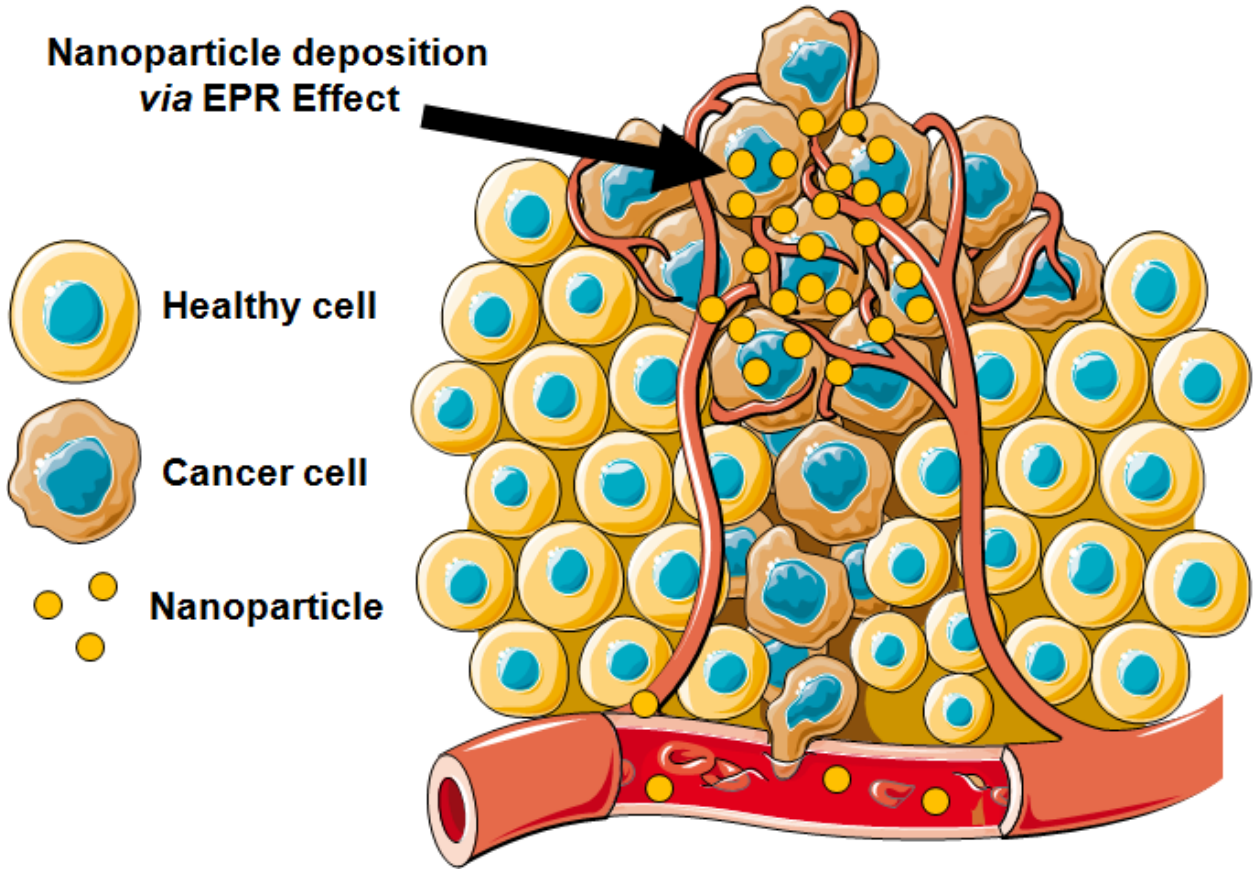

Figure 1.2 Nanoparticle deposition within a tumorous environment via the enhanced permeation and retention (EPR) effect. Nanoparticles travel throughout the blood stream and enter the tumor environment through perforations in blood vessels around cancerous tissue. Figure created using components courtesy of Servier (2016).

1.3.2 Treatment

Modern clinically-approved cancer treatments exist as one of four major interventions: chemotherapy, radiotherapy (RT), hormonal therapy and surgical procedures. When one or more of these treatments is combined with the primary mode of treatment, those therapies are referred to as adjunctive (Cunningham, 2000). Technological advancements have led to improved efficiencies but much work remains to be done, especially in the diagnostic and targeted therapy research realms (Baumann et al., 2016; Helleday et al., 2008; Ramaswamy et al., 2001). Below is a general description of clinically-available and experimental cancer treatment options.

1.3.2.1 Chemotherapy and Hormonal Therapy

Chemotherapy uses drug formulations to combat complications due to cancer growth and spread. Chemotherapeutic drugs are tailored to inhibit cell proliferation by directly attacking reproduction capabilities (Nitiss, 2009). Research has also been devoted to targeting the vasculature supplies tumor growth depends on in conjunction with traditional chemotherapy (Ma and Waxman, 2008). Typically, chemotherapy treatments are administered intravenously; however oral supplements are also used in certain therapy regimens (Findlay et al., 2008). Hormonal therapy relies on inhibition of hormones (*i.e.* estrogen, progesterone) associated with cancer cell proliferation (Swain et al., 2013).

1.3.2.2 Surgery

Depending on the location and size of a tumor, surgical excision may be a viable treatment option. In advanced cases of breast cancer, surgeons may be forced to complete

a mastectomy, where the entire breast is removed along with the primary tumor. In more ideal cases, tumor proliferation is limited and the breast may be spared. Recent technological advancements have made tumor removal easier and more efficient. Olson and co-workers (Veiseh et al., 2007) have developed a method for surgeons to differentiate between cancerous and non-cancerous solid tissue intra-operatively through use of a near-infrared-emitting fluorescent compound (Veiseh et al., 2007). In more extreme cases where tumors reside in locations such as the brainstem, effective surgery becomes increasingly difficult and treatment may be limited to medicinal and radiation-based palliative therapies (Lamm et al., 2013).

1.3.2.3 Radiation Therapy

Radiation therapy (RT) uses targeted beams of radiation to deposit energy into tumor tissue, resulting in severe biological effects in and around the dosage site. RT relies on either direct or indirect action to induce double strand breaks in target DNA, leading to replication inhibition (Lomax et al., 2013). Direct RT directly interferes with the atomic structure of the target molecule. The atoms of the target molecule are either ionized or excited and this results in biological change (Hall and Giaccia, 2012). Conversely, indirect radiation produces reactive species from molecules other than the target molecule (*i.e.* water), which in turn disrupt the target's atomic structure. As with the action radiation carries out, ionizing radiation also comes in direct and indirect forms. Directly ionizing radiation refers to the fact that the radiation source is itself charged (*i.e.*, proton or electron beam sources). Alternatively, indirectly ionizing radiation refers to radiation sources wherein the source is charge-neutral (*i.e.*, neutron and X-ray beam sources) (Hall and Giaccia, 2012) . Direct and indirect ionizing radiation forms are able

to cause DNA damage by both direct and indirect actions. RT doses are typically quantified in the SI unit, Gray (Gy), defined as Joules (J) of energy absorbed per Kilogram (Kg) mass (Agency, 2010). Side effects associated with radiation therapy depend on the treatment area as well as intensity and duration of exposure but may include swelling, bone marrow suppression, radiation fibrosis, cognitive impairment and a decreased chance of successful reconstructive breast surgery (Acharya et al., 2009; Hall et al., 2004; Hojan and Milecki, 2014; Kronowitz and Robb, 2009; Li et al., 2011).

1.3.2.4 Photothermal Therapy

Photothermal therapy (PTT) utilizes substances or metallic nanoparticles that produce heat upon photon irradiation, leading to the destruction of nearby cells and tissues. The process is largely dependent on the nanoparticle's surface plasmon resonance (SPR), defined as the oscillation capability of surface electrons upon irradiation with light having a corresponding frequency. When irradiated with a range of wavelengths, peaks associated with maximum electron oscillation or amplitude emerge in absorbance spectra (Newhouse et al., 2011). These SPR peaks can be tuned by changing the shape, size and chemical make-up of the particular nanomaterial in question. The heat-producing phenomenon has been the subject of in-depth investigation by El-Sayed and co-workers (Huang and El-Sayed, 2010). Changes in electron oscillations upon irradiation result in electron-electron collisions and subsequent energy transfer from affected electrons to nearby phonons. Recent studies have highlighted efforts to target PTT-active nanomaterials to cancer cells and tumor sites with hollow gold nanospheres (HNGs), gold nanorods (AuNRs) and gold nanocages (AuNCs) being among the most commonly used

(Dykman and Khlebtsov, 2012; Lu et al., 2009; Melancon et al., 2008; Yang et al., 2013; You et al., 2010).

In 2003, Hirsch and co-workers used silica-based gold nanoshells to complete PTT studies on breast carcinoma *in vitro* and *in vivo* (Hirsch et al., 2003). Cancer cells were incubated with nanoparticle-containing media for 1 hour then exposed to near-infrared light (820 nm, 35 W/cm) for 7 min. Cell samples treated with nanoparticles and NIR underwent local temperature increases, resulting in irreversible cellular damage. Subsequent studies have demonstrated effective targeting strategies to deliver high concentrations of HGN and AuNR to cancer sites through use of ligands including RNA and DNA-based aptamers and protein antibodies. When designing these nanoparticles, SPR peaks are optimally tuned to the near infrared wavelengths (800-950 nm) where tissue penetration is optimal and where absorbance by biological molecules is low. In 2014, one report highlighted the enhanced tumor killing potential of a HGN-based treatment using RT, PTT and chemotherapeutics (Jeong, 2014). Targeting ligands were not utilized in the study and systematic experimentation into the enhanced response was not completed. Subsequent research into combinational RT-PTT therapy against cancer is scarce despite the potential advantages such tandem therapy may offer.

1.3.3 Impact of Cancer on Canadians

The socio-economic and emotional impacts attributable to cancer are far-reaching and well understood. In 2000, cancer diagnosis and treatment cost Canadians 2.6 billion in health care coverage and another 14.8 billion in lost wages and productivity. Over 200,000 Canadians were projected to receive a cancer diagnosis in 2014, making treatment of the disease an expensive and formidable health-care task (Statistics, 2015).

Recent studies have reported increasing treatment costs and have cited the stressful atmosphere in which healthcare policy-makers must make decisions (de Oliveira et al., 2013; Meropol et al., 2009). Changes in chemotherapy and radiotherapy use among breast cancer patients are particularly startling, with dramatic increases witnessed in all age categories (de Oliveira et al., 2013). Today, the probability of a Canadian dying from cancer is 1 in 3.8, accounting for about 9 deaths per hour (Statistics, 2015).

1.4 Active and Passive Drug Targeting

Nanoscale drug delivery platforms rely on either active or passive targeting methods to attack and kill cancer in the body. Passive targeting relies on the previously-mention EPR effect. Here, the so-called "leaky" vasculature leading into the tumor microenvironment is taken advantage of. The integrity of the vasculature within the tumor microenvironment suffers from ~400 nm-sized holes and when a targeting ligand or delivery vehicle is smaller than the aperture, enhanced deposition of nanoconjugates will be evident, increasing the local concentration of drugs around the tumor.

Active targeting relies in part on the EPR effect in order to reach the tumor microenvironment but also in specific targeting ligand interactions with cancer cells within the tumor. Antibodies and nucleic acid aptamers are widely recognized for this purpose. Frequently, these ligands bind with high affinity to over-expressed proteins found on the surface of cancer cells in order to carry drugs or nanoparticles to the cancerous site. While antibodies have advanced further at present in terms of clinical use and development, there are a number of advantages to employing aptamers for drug targeting in medicine. Aptamers are smaller than antibodies and are chemically synthesized, therefore there is no need for complicated *in vivo* preparation methods

(Jayasena, 1999). Furthermore aptamers show higher stability in harsh conditions and can be easily chemically modified with specific functional groups. Still, aptamers are sensitive to nuclease degradation, a major roadblock for *in vivo* application. With respect to this issue, DNA-based aptamers are recognized to have enhanced stability over their RNA-based counterparts (Kim and Paeng, 2014).

1.5 Doxorubicin

The anti-cancer characteristics of Doxorubicin (DOX) were discovered in the 1950's and the drug was first approved for clinical use over 30 years ago (Judson et al.). Since then a host of new cancer drugs have been developed and range in their utility in the clinic depending on the type of cancer as well as to what extent acquired and inherent chemo-resistance are displayed by the patient (Voulgari and Pintzas, 2009). DOX has stood the test of time as a clinical agent and remains a frontline chemotherapeutic in many cancer therapy regimens (Gabizon et al., 2003). Likewise, its use as a model drug in delivery system design research has been sustained over the past three decades, owing in large part to its water solubility and fluorescence characteristics, which make it exceptionally easy to use in research applications (Ahmad et al., 1993; Aryal et al., 2009; Wang et al., 2013).

1.5.1 Chemical Structure

DOX (Figure 1.2) is chemically defined as an anthracycline molecule owing to its tetracyclic anthracene-like group being linked to an amine-containing sugar moiety (Arcamone et al., 1972). The planar tetracyclic portion of the molecule is a chromophore with fluorescence in the UV-Vis region of the electromagnetic spectrum and is active in

DNA intercalation. DOX has a pKa of 8.3 and is therefore protonated at physiological pH due to its amine moiety, which has been proposed to facilitate electrostatic interactions with various nanomaterials. The carbonyl groups of ring 2 provide potential sites of coordination with metallic nanomaterials and hydrogen bonding, as does the nitrogen-containing amine moiety of ring 5. The electron-rich tetracyclic system of the drug also provides the potential for π- π stacking and hydrophobic interactions (Liu et al., 2007).

Taken together, DOXs complex structural features lead to a number of interaction possibilities with nanomaterials currently used in biomedical and nanotechnology research. Better understanding the nature of DOX interaction and adsorption mechanisms as well as the accompanying release mechanisms will help to enhance and justify future drug delivery system development and investigation at the nanoscale.

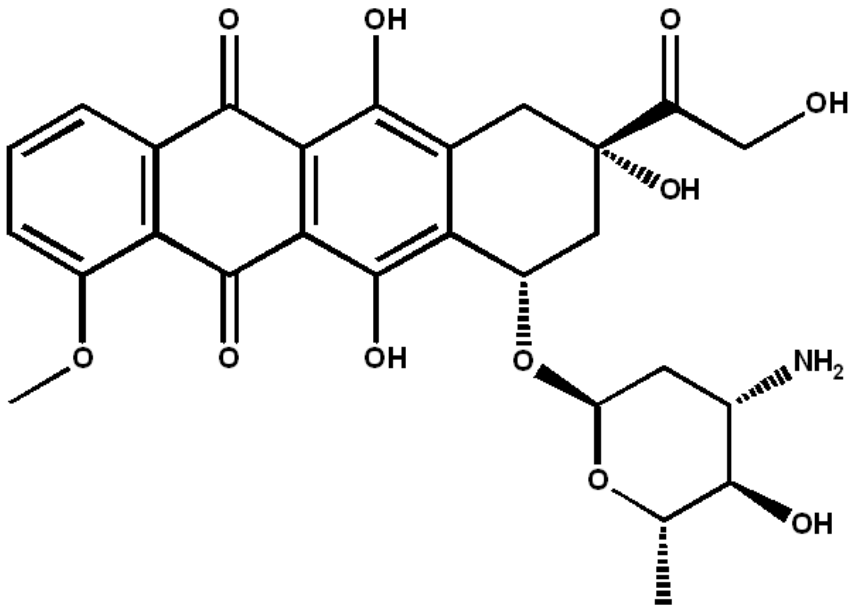

Figure 1.3 Chemical structure of Doxorubicin

1.5.2 Applications in Nanomedicine

Over the course of the last decade, numerous nanoscale-DOX formulations have demonstrated increased therapeutic efficiency both *in vitro* and *in vivo*. These formulations have proven novel in terms of their loading efficiencies as well as in the ways they evade difficult clinical impediments. Multi-drug resistance (MDR) remains a major hindrance for many therapeutic agents and nanotechnology has allowed for the development of 'stealth' vehicles in order to evade rapid drug efflux (Li et al., 2009). Further, many nanoparticle-delivery systems, through their ease of functionalization, are able to accommodate co-adsorption of polymers such as polyethylene glycol (PEG) for increased *in vivo* circulation times (Maruyama et al., 1992). In 2011, Wang and co-workers (Wang et al., 2011) demonstrated a gold nanoparticle-based doxorubicin delivery system wherein a pH-sensitive tethering technique was used to link DOX to the nanoparticle. The system was able to evade MDR and efficiently kill MDR+ cells through enhanced cellular uptake and drug release within acidic organelles. Moreover, the authors employed the fluorescent character of doxorubicin to probe drug release within the cells by monitoring the enhanced fluorescence upon release from the nanoparticle.

In 2009, Park and co-workers (Park et al., 2009) employed a dual-therapy platform wherein DOX was encapsulated within the core structure of poly(lactic-co-glycolic acid-gold shell nanoparticles. Upon irradiation with NIR light corresponding to the absorbance maximum of the gold shell, photothermal and chemotherapeutic cell killing was facilitated by increased local temperature and nanoparticle degradation-induced drug release. This study, and others like it, shed light on the therapeutic potential

hyperthermia-chemotherapy platforms embody following intelligent conjugate design. The authors demonstrate that the combinatory platform exceeded the additive cell killing potential attributable to the independent therapies, thereby demonstrating a synergistic therapeutic effect.

1.6 Polyethylene Glycol

Polyethylene glycol (PEG) is chemically defined as a long-chain polyether compound having both hydrophobic and hydrophilic components (Hu et al., 2007) (Figure 1.4). Polyether portions of the molecule allow for some degree of hydrophobic interactions, while the oxygen atoms and hydroxyl moieties allow for hydrogen bonding giving the compound a high degree of water solubility of up to 20% *w/w* for even high molecular weight PEG (20,000 g/mol). These components lead to interesting application potentials in fields of research such as drug delivery (Knop et al., 2010), spinal cord injury repair (Luo et al., 2002) and biosensor development (Liu et al., 2013).

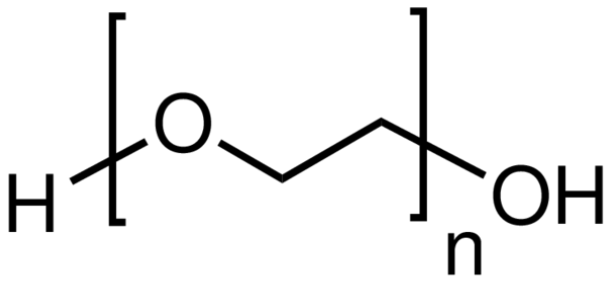

Figure 1.4 Chemical structure of polyethylene glycol.

1.6.1 Applications in Nanomedicine

PEG has been extensively used in drug delivery studies owing to its unique chemical properties in solution (Knop et al., 2010). Depending on the application of

interest, different weight-PEG molecules may be employed whereby extension of the repeating polyether unit, leads to increased molecular weight. PEG has found much success in the development of liposomal-based drug delivery systems (Gabizon, 2001). Perhaps most notably is liposomal doxorubicin, which comes in both PEGylated and un-PEGylated forms. Lipid molecules that make up the high molecular weight PEG can be conjugated to the hydrophilic terminal end of the lipid molecules used to form the liposomal drug vehicle. PEGylation results in increases in the effective size, weight and blood circulation time of the nanocarrier *in vivo*. In turn this has resulted in PEGylated nanoparticles being referred to as so-called 'stealth' delivery vehicles (Knop et al., 2010; Lasic and Needham, 1995).

1.7 Objectives

The thesis explores several important questions related to the use doxorubicin and gold nanoparticles in cancer therapy research. The specific objectives of the thesis were to:

1. Develop a novel method for the accurate quantification of DOX in drug delivery studies using polyethylene glycol.
2. Investigate the nature of the interaction between DOX and citrate-capped AuNPs and survey the feasibility of simple DOX-AuNP conjugates in therapeutic applications.

In chapter 2, doxorubicin adsorption to plate well surfaces is characterized and the inclusion of several polymer and protein-based reagents is studied as a means to decrease non-specific adsorption of the drug molecule to the plate surface. Trace amounts of

polyethylene glycol of high molecular weight are shown to adequately prevent such nonspecific adsorption and ensure both simple and robust quantitative methods. In chapter 3, a systematic study of the adsorption profile of doxorubicin onto citrate-capped gold nanoparticles is completed by varying chemical and physical parameters. In addition to systematic experimental evidence, theoretical modeling is provided to substantiate a cation-π- based interaction theory.

Chapter 2 Prevention of doxorubicin sorptive losses in drug delivery studies using polyethylene glycol

This chapter was published in the journal *RSC Advances:*

Dennis Curry,[a,b,c] Hope Scheller,[a,b] Mingsheng Lu,[a] Martin Mkandawire,[a,d] Mark R. Servos,[c] Shufen Cui,[e] Xu Zhang*[a,c,d] and Ken D. Oakes[a,b]. 2015. Prevention of doxorubicin sorptive losses in drug delivery studies using polyethylene glycol. *RSC Advances* 5, 25693-25698.

[a]Verschuren Centre for Sustainability in Energy and the Environment, Cape Breton University
[b]Department of Biology, Cape Breton University,
[c]Department of Biology, University of Waterloo
[d]Department of Chemistry, Cape Breton University
[e]Department of Biological Applied Engineering, Shenzhen Key Laboratory of Fermentation, Purifcation and Analysis, Shenzhen Polytechnic, Shenzhen, China.

Role of the co-authors:

- Dennis Curry: MSc candidate who researched, collected and analyzed data and wrote the paper
- Hope Scheller: assisted with data collection
- Mingsheng Lu, Martin Mkandawire, Shufen Cui: assisted with scientific ideas, editing and provided general advice.
- Xu Zhang, Mark R. Servos and Ken D. Oakes: Co-supervisors of Dennis Curry who assisted with scientific ideas, research direction, editing and provided general advice.

2.1 Summary

The non-specific sorption of hydrophobic pharmaceuticals on reaction vessel surfaces raises serious analytical challenges for their accurate quantification. Systematic error due to sorptive loss of analytes may result in significant overestimation of drug loading on nanomaterial-based drug delivery systems (DDS), leading to inaccurate determinations of dosage and DDS efficiency. We evaluated sorptive losses of doxorubicin (DOX), an effective chemotherapeutic, in polystyrene based 96-well plates, and proposed a simple but effective method to prevent the non-specific sorption of DOX using trace concentrations of polyethylene glycol (PEG). Relative to widely-used proteinaceous and surfactant surface blocking agents, PEG is effective, easy to use, and does not interfere with drug loading to the DDS.

2.2 Introduction

Doxorubicin (DOX) is widely employed as an effective chemotherapeutic for treatment of various solid tumors, but is associated with significant adverse side effects including cardiomyopathy, potentially resulting in congestive heart failure. (Chatterjee et al., 2010; Singal and Iliskovic, 1998). To address this issue, research into drug delivery systems (DDSs) that use nanomaterial-based drug carriers designed with targeting functionality could enhance DOX effectiveness by delivering high drug concentrations directly to cancerous tissues (Kong et al., 2014). Such a DDS would decrease both required concentrations, and by being targeted, reduce adverse side effects in blood and other organs (Allen and Cullis, 2004; Bagalkot et al., 2006; Hrubý et al., 2005; Kataoka et al., 2001; Kwon et al., 1997). Accurate quantification of drug loading capacity to nanomaterials is not only critical to evaluate the efficacy of the nano-drug carriers in

DDS development research, but also important to determine the dosage of the DDS for clinical trials. However, quantitative evaluations of DDS efficacy have been significantly hampered by the non-specific sorption of DOX to various plastic containers during storage and analysis (Tomlinson and Malspeis, 1982; Wood et al., 1990b; Wu and Ofner, 2013), with photo-degradation further deteriorating data quality (Beijnen et al., 1986; Janssen et al., 1985; Wood et al., 1990a). Gold nanoparticles (AuNPs) are an example of nano-drug carriers for DDS development. When evaluating the loading capacity of DOX onto AuNPs, there are three experimental steps: drug loading to AuNPs, separation of free DOX from bound fractions (*i.e.,* DOX-AuNP conjugates), and instrumental quantification of the free fraction. The loading capacity of DOX to each AuNP is measured by the optical signal difference (absorbance or fluorescence) before and after DOX loads to the nanoparticles, as shown in Eq. 1.

$$N_{Loading} = (C_{total} - C_{free}) / C_{AuNP} \qquad (1)$$

Where $N_{Loading}$ is the number of DOX adsorbed to each AuNP, C_{total} and C_{free} are the total and free concentration of DOX, and C_{AuNP} is the concentration of AuNPs in the drug loading system. Any DOX adsorbed to the container surfaces (*e.g.,* microcentrifuge tubes, micropipette tips, or 96 well plates), is attributed by Eq.1 to the loading capacity of AuNPs for DOX, which can overestimate the loading capacity of the drug carriers. The assumption underlying such calculations is a negligible sorptive loss of DOX, which in reality has been disproven in several studies (Tomlinson and Malspeis, 1982; Wood et al., 1990b; Wu and Ofner, 2013).

To date, the adsorption of DOX to various material surfaces including glass, siliconized glass, polyethylene, polypropylene, polytetrafluoroethylene, polyvinylchloride, and cellulose dialysis membranes has been well documented (Tomlinson and Malspeis, 1982; Wood et al., 1990b; Wu and Ofner, 2013). However, there is no data for the adsorption of DOX on polystyrene 96-well plates, which are routinely used for laboratory fluorescence quantification. Systematic non-specific sorption experimental error, if present, would seriously affect fluorescence measurements, leading to false conclusions. Further, there is little research on approaches to prevent DOX sorptive losses and ensure analytical accuracy, despite the drug's widespread use in this context (Fan et al., 2014; Mohan and Rapoport, 2010; Ren and Wei, 2004). To address these problems, we propose a simple but effective method to prevent sorptive losses by incorporating trace (part-per-million) concentrations of polyethylene glycol (PEG) into the buffer used to dissolve DOX (shown in Figure 2.1). Critically, the addition of PEG does not interfere with the loading of DOX to nanoparticle surfaces, thereby ensuring accurate quantification of drug loading capacity.

2.3 Materials and Methods

2.3.1 Chemicals

PEG, Bovine Serum Albumin (BSA), Tween-40, Triton X-100, HEPES and doxorubicin hydrochloride were purchased from Sigma-Aldrich. Ethylene glycol was purchased from Alfa Aesar (Ward Hill, MA) while polystyrene 96-well plates were purchased from Corning Inc. (NY) and microcentrifuge tubes (Cat. No. 02-681-284; Lot

No.: 13300434) and ethanol were purchased from Fisher Scientific (Ottawa, ON, Canada). Nanopure 18.2 MΩ-cm water was used in all experimentation.

2.3.2 Doxorubicin Adsorption Kinetics and Isotherm

In all experiments, doxorubicin was quantified by fluorescence measurement (excitation/emission: 480 nm/580 nm) using a TECAN Infinite M10000 PRO micro-plate reader. Polystyrene 96-well plates (Costar 3915, Lot No.: 26313022) were used in all quantification experiments with working volumes of 100 μL in each well, with the exception of isotherm determination where sample volume was increased to 150 μL to offset evaporation during extended measurement times (90 min, n=3).

Doxorubicin stock solution (5 μM in Nanopure water stored in a 1.5-mL amber tube at -20^{o}C) were added to wells containing varying volumes of HEPES buffer (5 mM, pH 7.6 to a final volume of 150 μL in each well) to achieve DOX concentrations ranging from 0.25 to 2.5 μM. DOX adsorbed onto the plate surface was determined by recording the decrease in fluorescence over 90 min. The calibration was performed against a standard curve whose solutions included 10 ppm of PEG 20K.

To determine the role of blocking agents on non-specific DOX adsorption to 96-well plate surfaces, DOX adsorption kinetics were monitored in the presence of various molecular weights (1K, 2K, 4K, 8K, and 20K) and concentrations of PEG. DOX aqueous solutions without any blocking agents added served as the control. Typically, 80 μL of HEPES buffer (5 mM, pH 7.6) were mixed with 10 μL of PEG solution in each well, followed by 10 μL of doxorubicin solution for a final volume in each well of 100 μL. The mixture was gently mixed before recording fluorescent signals over defined intervals

(*i.e.,* 6 - 10 min). The identical procedure was repeated for other surface blocking reagents including BSA, Tween-40, and Triton X-100.

The kinetics and capacity of citrate-stabilized AuNPs for DOX adsorption in the presence or absence of blocking reagents (n = 3) was evaluated by fluorescence change over time before and after blocker addition. The final volume of solution in each well was 100 μL, comprising 70 μL of 5 mM HEPES buffer, 10 μL of surface-blocking reagent solution (PEG, BSA, Tween-40, or Triton X-100), 10 μL of DOX stock solution (5 μM in Nanopure water) and 10 μL of (10 nM) AuNP solution.

2.3.3 Microcentrifuge Tubes

PEG was evaluated as a blocking agent against doxorubicin adsorption onto surfaces of microcentrifuge tubes (n = 3). Briefly, 10 μL of PEG 20K (1000 ppm) was added to 80 μL of Nanopure water with varying concentrations of NaCl (0, 15, 30, 60, 90, 120, 150 mM) and gently mixed by shaking (control tubes contained an additional 10 μL of HEPES buffer instead of PEG solution). To this mixture, 10 μL of doxorubicin stock solution (75 μM) was added into the tubes and gently mixed again. After 10 min, 10 μL of this mixture was combined with 90 μL of HEPES-PEG buffer (PEG 20K: 10 ppm) in the 96-well plate for fluorescence measurements. In this experiment, the HEPES-PEG buffer was used to prevent DOX adsorption to the plate wells, so our results only reflect adsorption to microcentrifuge tube surfaces.

2.3.4 Doxorubicin Degradation Studies

The potential protective ability of PEG to inhibit the photodegradation of DOX was evaluated using a Safe Imager™ Blue Light Transilluminator. Briefly 1 mL of DOX

stock solution was added to a 10 mL clear glass vial (n = 3). Increasing concentrations of PEG 20K were added to achieve a final volume of 1.5 mL before solutions were mixed and capped. Vials containing DOX-PEG were then exposed to the blue light source (λ = 470 nm) from the Transilluminator for increasing time intervals with doxorubicin fluorescence measured kinetically (10 μL of sample solution and 90 μL of HEPES-PEG buffer in the plate well).

2.4 Results and Discussion

2.4.1 Sorptive Losses of DOX

The sorptive loss of DOX onto various experimental plastic containers might seriously compromise quantitative evaluations of drug delivery system (DDS) performance (Tomlinson and Malspeis, 1982; Wood et al., 1990b; Wu and Ofner, 2013). For example, if loading 10 μM DOX to gold nanoparticles (AuNPs), the DOX concentration is normally 10^2-10^5 times that of the concentration of the nanomaterials for experimental use (for example, the concentration of widely used 13 nm AuNPs is about 10 nM). Under these conditions, 20-50% (2-5 μM) cumulative sorptive losses could be expected during multi-step-experiments (including drug loading, centrifugation in polypropylene microcentrifuge tubes, and during quantification in 96-well plates). Consequently, the total available concentration of DOX in the solution would be 50-80% (*i.e.*, 5-8 μM) of the originally added concentrations. If we assume the real loading capacity is 500 DOX/AuNP, the calculated loading capacity would be 700-1000 DOX/AuNP, which would be 40-100% overestimated; such overestimates result in unreliable conclusions.

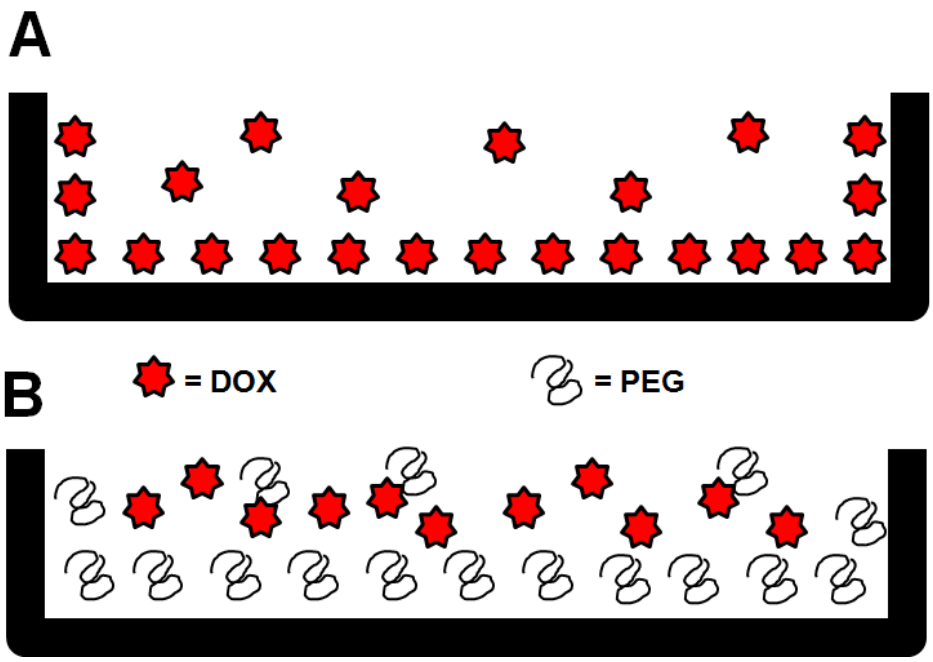

Figure 2.1 Schematic representation of DOX sorptive losses via non-specific adsorption to plate wells (A) and prevention of non-specific sorptive losses of DOX by inclusion of PEG (B).

The non-specific sorption of DOX to polypropylene microcentrifuge tubes was evaluated as these tubes are among the most frequently used plastic vessels in laboratory experiments. The adsorption of DOX (7.5 µM DOX in 100 µL 5 mM HEPES buffer, pH 7.6) onto polypropylene tube surfaces decreased fluorescent signal intensities ~ 20% over 30 min; lower DOX concentrations (0.25 µM) experienced relatively greater sorptive losses of 40% over 10 min (Figure 2.2B), which is consistent with previously published data (Tomlinson and Malspeis, 1982). To elucidate the mechanism of DOX adsorption, the influence of NaCl, ethanol, and ethylene glycol on the amount of DOX adsorbed to the tube was evaluated. Adsorption would be essentially attributable to electrostatic interactions if the addition of NaCl decreased adsorption due to the charge screening effect, while adsorption would be primarily driven by hydrophobic interactions if the

presence of organic solvents (EtOH and EG) decreased sorptive losses of DOX. Sorptive DOX losses were in fact unaffected by NaCl concentrations (Figure 2.2A) but reduced by ethanol and ethylene glycol (EG, as discussed later) indicating DOX adsorption to container surfaces is governed by hydrophobic rather than electrostatic interactions.

We next evaluated DOX sorptive losses in polystyrene 96-well plates, which are again widely used for fluorescence-based DOX quantification. DOX loading capacity, as observed by Langmuir isotherm, was determined as 520 nM per well on 96-well plates (Figure 2.2C). At 520 nM, assuming the size of each DOX molecule is about 3.17 nm^2 with a diameter of 1 nm, (based on the theoretical estimation of DOX molecule size of 1.026 nm in diameter using the Global Minimum approach at the lowest energy) we can determine each 100 µL well working volume can adsorb 3 X 10^{13} DOX molecules on each 95 mm^2 useable well surface. The Langmuir isotherm and aforementioned calculations support a monolayer adsorption model. The adsorption of DOX to plate well surfaces is a relatively fast process with the adsorption-desorption equilibrium achieved within 40 min (Figure 2.2B), a typical time interval for drug adsorption experiments with nanomaterials (Wang et al., 2013; Wang et al., 2011).

2.4.2 PEG Effect on Sorptive Losses of DOX

Currently, there are several established agents used for surface blocking including BSA and the surfactants Tween and Triton X-100, which are efficacious in preventing sorptive losses in various bioassays (Liu et al., 2013). However, these traditional blocking methods have limitations such as additional and time-consuming plate treatment steps (*e.g.,* 0.5-12 h for BSA blocking), generating air bubbles in the sample solution during mixing, and potential for interference with DOX loading onto nanomaterials. All of these

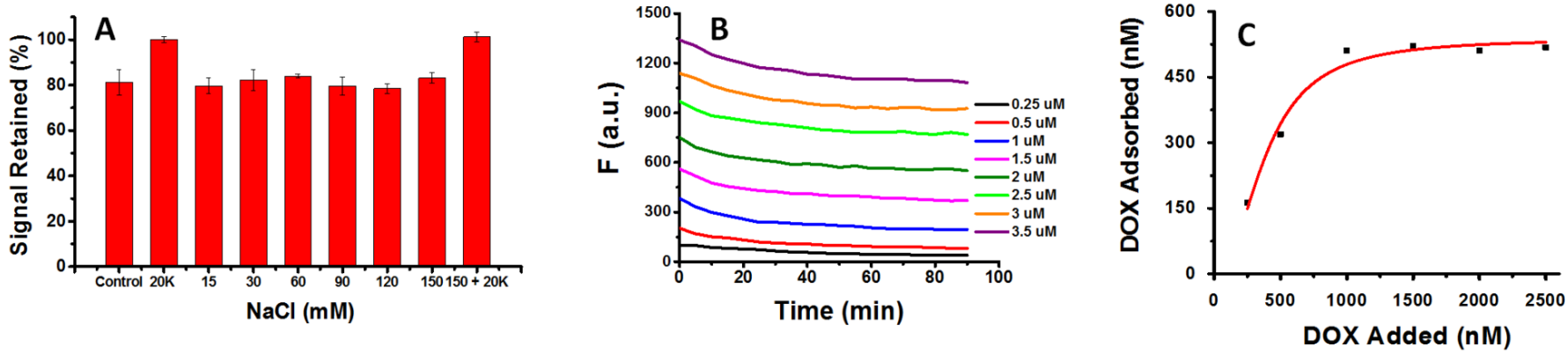

Figure 2.2 Sorptive losses of doxorubicin to polypropylene micro-centrifuge tubes (A) and polystyrene 96-well plates (B and C). (A) The effect of salt and/or PEG 20K on DOX sorption onto microcentrifuge tube surfaces. In the control tube, no chemicals other than DOX aqueous solution were added. (B) Decrease in the fluorescence of various DOX concentrations (from 0.25 to 3.5 µM) within plate wells over time; (C) the Langmuir isotherm for non-specific sorption to plate-well surfaces.

technical issues can be overcome by using low concentrations of PEG as the blocking agent. The presence of 10 ppm of PEG 20K in the plate wells produces neither air bubbles nor inhibition of DOX loading, as evidenced by retention (of around 100%) of DOX fluorescence intensity (Figure 2.3). Initially, we tested the effects of PEG molecular weight (MW) and concentration on DOX adsorption to the surfaces of polystyrene plate wells (Figures 2.3 and A.1). This trial demonstrated that although PEG 1000 is helpful (~ 98% of DOX was retained, only 2% sorptive loss), PEG of larger MW were more effective. For example, only 10 ppm of PEG 20K (0.5 μM) demonstrated comparable blocking efficacy as 100 ppm of PEG 4K or 1000 ppm of PEG 1K (Figures 2.3 and A.1). Consequently, the role of PEG MW and concentration on sorptive loss of DOX was systematically evaluated (Figure A.1), producing the conclusion that 10 ppm of PEG 8000 is generally effective in addressing sorptive DOX losses in 96 well plates. Similar blocking protection for DOX in the presence of 10 ppm of PEG 20K within polypropylene microcentrifuge tubes was observed (Figure 2.2A), indicating the universality of PEG blocking in plastic vessels, which is consistent with results demonstrated in homogeneous biosensor development (Liu et al., 2013).

There are two potential mechanisms contributing to PEGs' reduction of sorptive losses of hydrophobic drugs such as DOX from the drug loading solution (Figure 2.1). First, PEG molecules, especially those of higher molecular weight (*i.e.*, ≥ 4K), can adsorb to plate surfaces, preventing DOX adsorption as evidenced by the Langmuir adsorption isotherm (Figure 2.2C) (Liu et al., 2013; Zhang et al., 2012b, c). The second possible mechanism is that the addition of PEG decreases the aqueous buffer polarity, thereby increasing DOX solubility, as observed and utilized in organic synthesis by other groups

(Chen et al., 2005; Herrmann et al., 1983; Hirano et al., 2012). If PEG was in fact modifying the polarity of the solution, we would expect molecules with similar properties to exert similar effects. Our results with ethanol and EG also support this mechanism, as 10% ethanol or EG significantly alleviated sorptive losses of DOX relative to a control lacking ethanol or EG, albeit less effective than 10 ppm of Tween 40, Triton X-100, or PEG 20K (Figure 2.4).

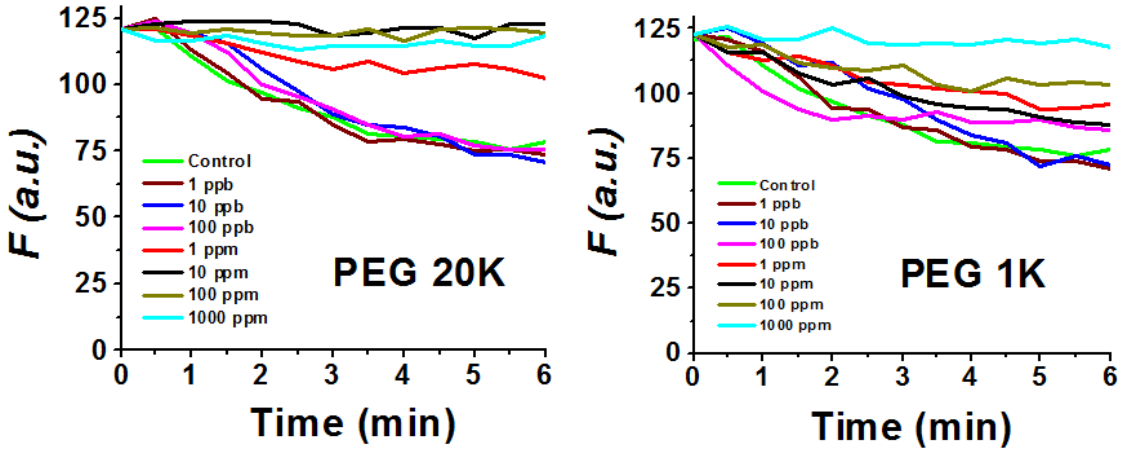

Figure 2.3 The effects of PEG (various concentrations and molecular weights) on DOX adsorption onto 96 well plate surfaces. In the control wells, no chemicals other DOX aqueous solution were added.

Additionally, it is also possible DOX could bind to PEG molecules, reducing DOX molecule polarity and thereby increasing solubility. We tested this potential mechanism by studying if DOX was adsorbed to PEG-coated AuNPs (pre-functionalized with thiolated PEG 2K). Since AuNP is an excellent fluorescence quencher (based on nanoparticle surface-energy transfer (NSET), it would quench the fluorescence of DOX upon binding (Daniel and Astruc, 2004; Dulkeith et al., 2002; Mayilo et al., 2009). However, after DOX solution was added to the PEG-SH-AuNP solution and incubated

under room temperature for 30 min, no DOX adsorption (as evidenced by fluorescence quenching) was observed by monitoring the fluorescence intensity of the supernatants. All DOX signals were recovered by centrifugation, demonstrating DOX does not adsorb to PEG (data not shown).

2.4.3 PEG Effect on DOX Loading on Gold Nanoparticles

As mentioned previously, many surface blocking agents, when employed to prevent sorptive losses of DOX to plastic vessel surfaces, may also block the surface of the drug carrier (*i.e.,* gold nanoparticles in the current work), significantly affecting drug-loading capacity. We compared several surface blocking reagents (*i.e.,* BSA, Triton X-100, Tween 20, and PEG 20K) for their capacity to prevent sorption of DOX to polystyrene plate wells (as shown in Figure 2.4) but also their interference of DOX loading to AuNPs. DOX solution fluorescence in plate wells was recorded over 10 min in the presence of these various blocking reagents (10 ppm) with AuNPs added into each well after 240 s. Over the first 240 s, there was a 19% decrease in DOX fluorescence (as indicated by the distance *a*) for the control sample (no blocking reagent) in the plate wells; in contrast, Triton X-100, Tween and PEG 20K maintained a near constant fluorescence level, indicating they effectively prevented sorptive losses of DOX to plate well surfaces (Figure 2.5). However, 10 ppm BSA did not prevent the DOX adsorption to the plate surface, which is reasonable considering the hydrodynamic diameter of BSA (~7 nm) and the high protein binding affinity of DOX (~75%). Presumably, DOX adsorbed to plate well surfaces between adjacent BSA molecules, and/or to BSA itself, forming BSA-DOX conjugates.

Interference of DOX loading to AuNP surfaces was evaluated by comparing fluorescence quenching after addition of AuNPs in the system after 240 s. These results demonstrate 10 ppm of PEG 20K and Triton X-100 did not block DOX loading to AuNPs any more than the control (lacking blocking agents), while Tween and BSA inhibited DOX loading to the greatest degree. Additional evidence was obtained by directly comparing the number of DOX molecules sorbed onto AuNP surfaces in the presence or absence of PEG 20K (Figure A.2); critically, the amount of DOX loaded to AuNPs was independent of the presence of PEG 20K ($p = 0.0647$). Conversely, Tween and BSA may inhibit DOX loading to AuNPs by directly blocking AuNP surfaces, or by decreasing free DOX available to bind AuNPs by binding to DOX themselves.

Unlike BSA, which is commonly pre-coated to block non-specific adsorption in biochemical assays such as enzyme-linked immunosorbent assays (ELISAs), PEG 20K must be added into the system concurrent with other reagents (DOX and AuNPs). This was evident from our experiment directly testing the effectiveness of PEG 20K and other surface-blocking agents to pre-coat plate wells in a separate step similar to that where BSA is used as a blocking agent of ELISA plates. In our experiment, plate wells were treated with 1% (*v/v*) BSA, PEG 20K, Tween 40, and Triton X-100 (100 ppm) in HEPES buffer (5 mM, pH 7.6) for 30 min at room temperature. After incubation, these pre-coated plate wells were rinsed twice with HEPES buffer prior to DOX fluorescence measurement in HEPES buffer. Two controls were included in this experiment; the first, a positive control, for which the plate wells were treated only with HEPES buffer and the DOX solution contained 10 ppm of PEG 20K. The negative control plate wells contained only HEPES and DOX buffer solutions. DOX sorptive losses remained significant in the

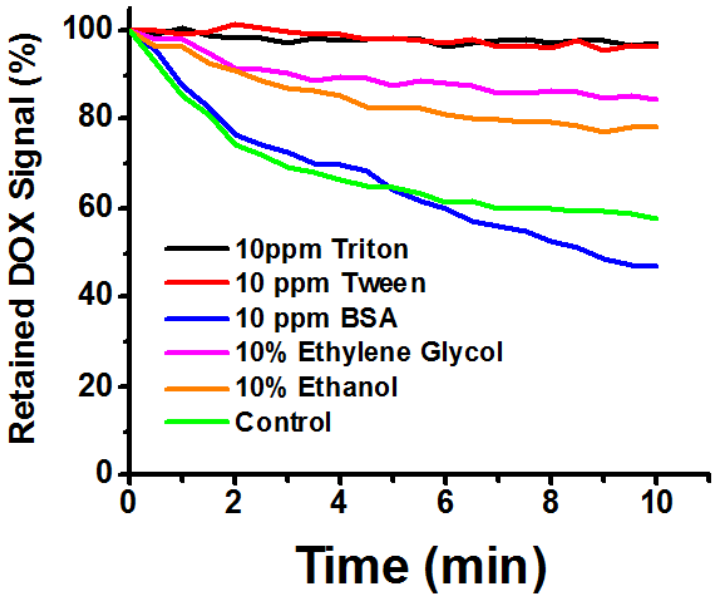

Figure 2.4 Comparison of several surface-blocking agents with 10% (v/v) ethylene glycol and ethanol. In the control wells, no chemicals other than DOX aqueous solution were added.

PEG-treated plate wells, similar to those not receiving any pre-treatment, presumably as PEG binding to the plate surface was weak, and PEG was unable to adhere to the well surfaces during plate rinsing (Figure 2.6). Consequently, the simplest and most effective means of PEG preventing DOX sorptive losses is by including 10 ppm of PEG 20K into the buffer used to prepare DOX solutions. Similar to BSA, Tween and Triton X-100 are also unsuitable blocking agents for pre-treating plate wells. Although BSA did not reduce DOX's sorptive losses when concurrently added (Figure 2.4) but rather interfered with DOX loading to AuNPs (Figure 2.5), it was however an effective pre-treatment blocker to prevent sorptive losses of DOX, although quite time-consuming and requiring extra steps.

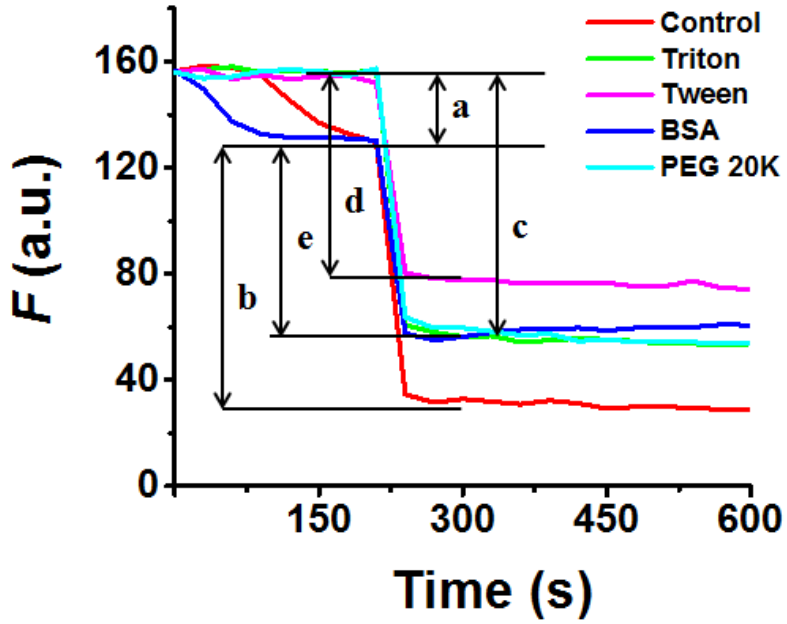

Figure 2.5 Inhibition of DOX loading to AuNPs by several surface blocking reagents (BSA, Triton X-100, Tween 20, and PEG 20K). AuNPs were introduced after 240 s; no surface blocking agents were added to control wells.

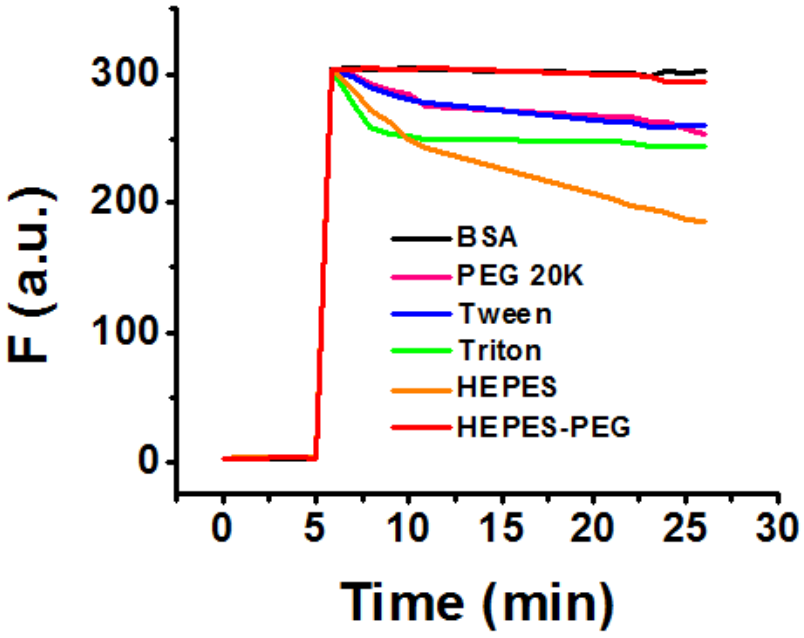

Figure 2.6 Relative effectiveness of surface-blocking agents as assessed by monitoring DOX fluorescence in plate wells pre-coated with the various surface-blocking agents.

2.4.4 PEG Effect on Photo-Degradation of DOX

In addition to sorptive losses, DOX can be photodegraded during storage or analysis upon light exposure (Beijnen et al., 1986; Janssen et al., 1985; Tomlinson and Malspeis, 1982; Wood et al., 1990a, b; Wu and Ofner, 2013). Previous studies demonstrated PEG-coated liposomes reduced UVA-induced photodegradation of encapsulated DOX (Bandak et al., 1999); consequently, we investigated if PEG 20K could protect DOX from blue light (λ = ~ 470 nm) degradation. Photodegradation of DOX was reduced to less than 2% following a 1 min exposure in buffer containing 8000 ppm (or 0.8%) PEG 20K (Figure 2.7). Even in the presence of only 10 ppm PEG 20K, 74% of intact DOX remained after 1 min light exposure, in contrast to 58% remaining when PEG was absent. Notably, even if 8000 ppm PEG 20K was present, photodegradation continued increasing over time. The protective mechanism of PEG 20K is presumably via decreasing DOX adsorption onto the inner vial surfaces, where the distance between DOX molecules and photons is minimal and photodegradation of DOX is maximized.

Interestingly, the protective effect of PEG 20K increased with increased PEG concentrations, a phenomena for which the underlying mechanism is not yet clear but deserving of future investigation. There are several facts contradictory to established mechanisms for PEG enhancing DOX photo-stability; first, PEG 20K does not absorb blue light (Figure A.3). Second, the DOX concentrations are low (5 µg/mL) and insufficient for concentration-induced self-protection. Third, the PEG 20 K buffer pH was 7.6, while it is acidic buffer that facilitates the ready degradation of DOX (Janssen et al., 1985; Wood et al., 1990b; Wu and Ofner, 2013).

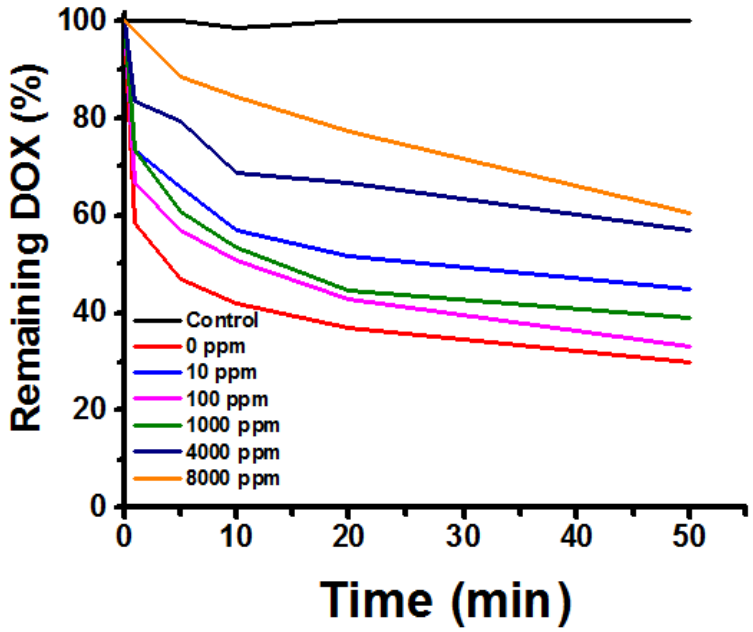

Figure 2.7 DOX photodegradation kinetics in solutions containing various concentrations of PEG 20K. The control sample was not exposed to blue light.

2.5 Conclusions

In summary, this work demonstrates small amounts of PEG (ppm level) can effectively protect DOX from sorptive losses, and to a limited extent, from photodegradation. Collectively, our data suggests PEG holds promise for use in storage, transportation, and accurate evaluations of drug delivery systems by reducing non-specific adsorption, a common experimental artifact and analytical challenge in drug analysis. Therefore, this work has wide implications for drug analysis in the pharmaceutical industry and has additional application for environmental scientists.

Chapter 3 Adsorption of Doxorubicin on Citrate-Capped Gold Nanoparticles: Insights into Engineering Potent Chemotherapeutic Delivery Systems

This chapter was published in the journal *Nanoscale*

Dennis Curry[a,c], Amanda Cameron[a] ,Bruce MacDonald[b], Collins Nganou[a], Hope Scheller[a,f], James Marsh[b], Stefanie Beale[d], Mingsheng Lu[a], Zhi Shan[a], Rajendran Kaliaperumal[a], Heping Xu[e], Mark Servos[c], Craig Bennett[d], Stephanie MacQuarrie[b], Ken D. Oakes[a,f], Martin Mkandawire[a], and Xu Zhang[a*] 2015. Adsorption of doxorubicin on citrate-capped gold nanoparticles: insights into engineering potent chemotherapeutic delivery systems. Nanoscale 7, 19611-19619.

[a]Verschuren Centre for Sustainability in Energy and the Environment, Cape Breton University
[b]Department of Biology, Cape Breton University,
[c]Department of Biology, University of Waterloo
[d]Department of Chemistry, Cape Breton University
[e]Department of Biological Applied Engineering, Shenzhen Key Laboratory of Fermentation, Purifcation and Analysis, Shenzhen Polytechnic, Shenzhen, China.

Role of the co-authors:

- Dennis Curry: MSc candidate who researched, collected, analyzed data and wrote the paper.
- Hope Scheller: assisted with data collection.
- Martin Mkandawire, Amanda Cameron and Collins Nganou: designed experiments, collected and analyzed data and wrote the results and discussion for the theoretical modeling portion of the manuscript in addition to assisting with editing and providing general advice.
- Stephanie MacQuarrie, Bruce MacDonald and James Marsh: performed organic synthesis, characterization and purification of organic drug analog molecules and assisted with editing.
- Rajendran Kaliaperumal: assisted with data collection and provided general advice.
- Mingsheng Lu, Zhi Shan and Heping Xu: assisted with ideas, research direction and general advice.
- Craig Bennett and Stefanie Beale: completed sample preparation and TEM imaging and editing.
- Xu Zhang, Mark R. Servos and Ken D. Oakes: Co-supervisors of Dennis Curry, who assisted with ideas, research direction, editing and provided general advice.

3.1 Summary

Gold nanomaterials have received great interest for their use in cancer theranostic applications over the past two decades. Many gold nanoparticle-based drug delivery system designs rely on adsorbed ligands such as DNA or cleavable linkers to load therapeutic cargo. The heightened research interest was recently demonstrated in the simple design of nanoparticle-drug conjugates wherein drug molecules are directly adsorbed onto the as-synthesized nanoparticle surface. The potent chemotherapeutic, doxorubicin often serves as a model drug for gold nanoparticle-based delivery platforms; however, the specific interaction facilitating adsorption in this system remains understudied. Here, for the first time, we propose empirical and theoretical evidence suggestive of the main adsorption process where 1) hydrophobic forces drive doxorubicin towards the gold nanoparticle surface before 2) cation- π interactions and gold-carbonyl coordination between the drug molecule and the cations on AuNP surface facilitate DOX adsorption. In addition, biologically relevant compounds, such as serum albumin and glutathione, were shown to enhance desorption of loaded drug molecules from AuNP at physiologically relevant concentrations, providing insight into the drug release and *in vivo* stability of such drug conjugates.

3.2 Introduction

3.2.1 Doxorubicin

Doxorubicin (DOX), an anthracycline chemotherapeutic, remains at the forefront of malignant breast, leukemic and sarcoma cancer treatment more than 30 years after its clinical inception and FDA approval (Judson et al., 2014) Despite its widespread usage,

DOX is often associated with multidrug resistance as well as adverse side effects such as nausea, hair loss and acute and chronic cardiotoxicity, the latter potentially leading to congestive heart failure (Anderson et al., 1981; Chatterjee et al., 2010; Gottesman et al., 2002; Hesketh and Sanz-Altamira, 2012). Liposomal formulations of DOX have led to improvements in the drug's efficiency but the development of advanced targeted drug delivery system (DDS) platforms for DOX remains a worthwhile research endeavor receiving substantial investment (Allen and Martin, 2004; Bagalkot et al., 2006; Gabizon et al., 1994; Gabizon et al., 2003; Kim et al., 2010). An ideal targeted DOX delivery platform would decrease required concentrations as well as the prevalence and intensity of side effects associated with the drug, all while utilizing its potent anti-cancer properties (Jean et al., 2015).

3.2.2 Gold Nanoparticles

Gold nanoparticles (AuNPs) have become an increasingly popular DDS development in recent years (Cheng et al., 2008; Ghosh et al., 2008a; Ghosh et al., 2008b; Paciotti et al., 2006; Zhang et al., 2011). High biocompatibility, tunable surface chemistry, and unique optical properties make nanogold a desirable platform for many biomedical applications (Arvizo et al., 2010; Saha et al., 2012; Shukla et al., 2005; Zhao and Liu, 2014). Further, AuNPs have been commercialized for use in diagnostic applications and are involved in clinical-phase trials (Jans and Huo, 2012; Libutti et al., 2010; Park et al., 2009). Numerous studies have highlighted AuNPs promise in the targeted delivery of anticancer drugs including DOX to cancerous cells and tissue (Cheng et al., 2008; Wang et al., 2011). Gold nanorods (AuNRs) and hollow gold nanoparticles (HGNs) allowing for the absorption of tissue-penetrating near-infrared (NIR) light have

been successfully used in combinational chemo-photothermal therapy (PTT) and imaging applications (Huang and El-Sayed, 2010; Kong et al., 2015; Lu et al., 2009; You et al., 2010).

3.2.3 Doxorubicin Loading onto Nanoscale Gold

Currently, there are two mechanisms for loading DOX to nanogold delivery vehicles (Figure 3.1). The first approach is through indirect attachment with thiolated anchor molecules such as methoxy-poly ethylene glycol (mPEG), (Aryal et al., 2009) double-stranded DNA rich with G-C base-pairs (Kim et al., 2010), and copolymers (Prabaharan et al., 2009). In this system, controlled release of DOX can be efficiently achieved via either temperature induced DNA melting or pH-sensitive cleavage (i.e., acid-cleavable hydrazone linkage) (Wang et al., 2011). The second approach is the direct adsorption of DOX onto gold surfaces (Elbialy et al., 2014; Mirza and Shamshad, 2011; You et al., 2010). DOX has been demonstrated to have high affinity for various gold nanomaterials such as solid AuNPs, AuNRs and HGNs. HGNs showed exceptionally high loading of DOX due to their high surface area (You et al., 2010). In contrast to the elegant, controllable, yet complicated indirect DOX loading procedure, direct adsorption is simple and straightforward, but the physiochemical interaction mechanism between DOX and AuNPs remains largely understudied, with only limited reports discussing potential interaction mechanisms available at present. In these reports, an electrostatic interaction between the positively-charged amine moiety of DOX and the negatively-charged citrate that serves as the capping ligand on the surface of AuNPs is proposed to facilitate DOX adsorption, (Elbialy et al., 2014; Mirza and Shamshad, 2011) but, to date, such salt-bridging interactions have not been substantiated by systematic

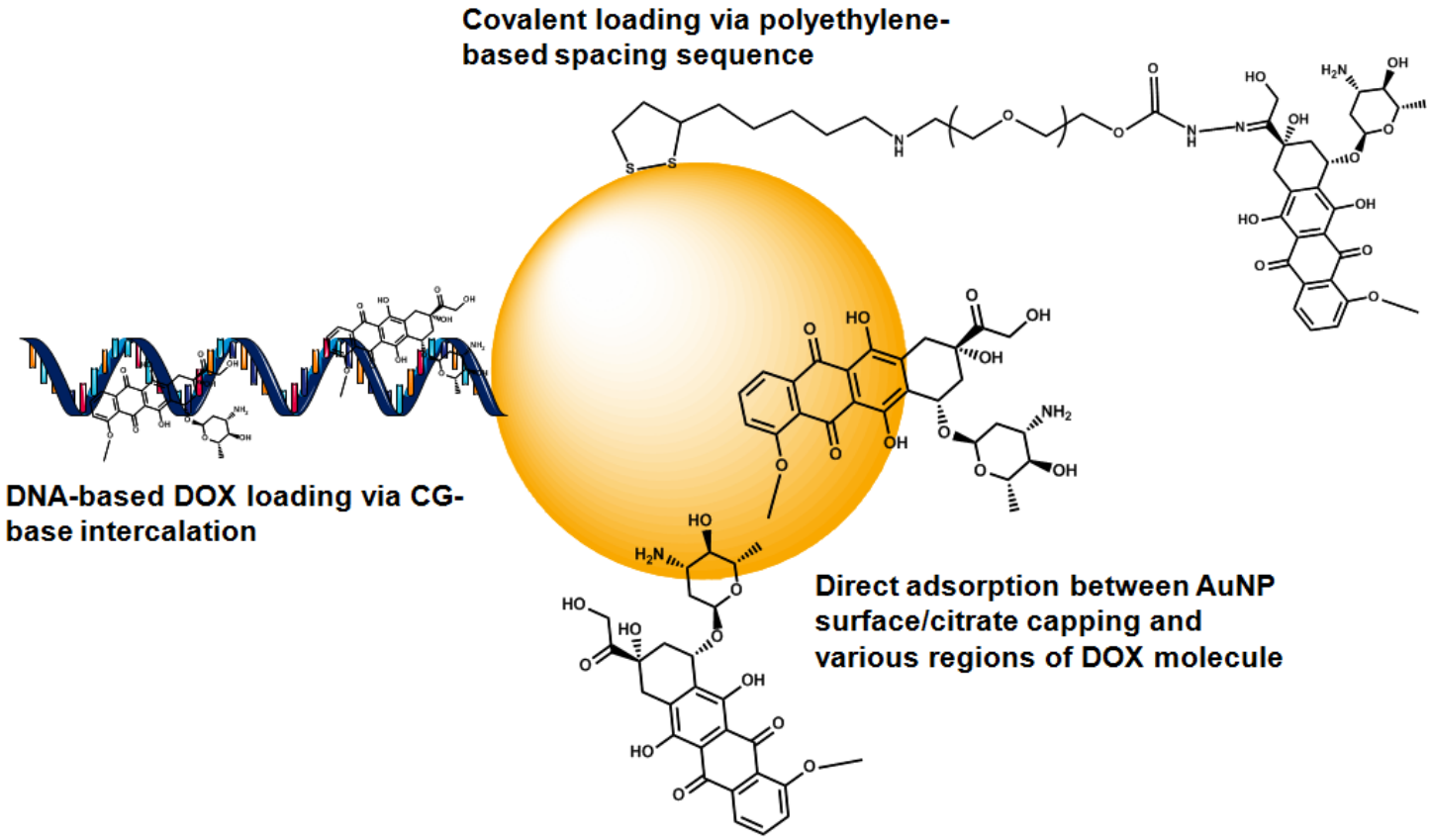

Figure 3.1 Schematic highlighting the various techniques used to load DOX to AuNP in drug delivery systems.

experimentation. The immense interest in AuNP-DOX based DDS development, together with limited mechanistic understanding of the system, motivated us to conduct more rigorous investigations better defining the physiochemical interactions driving DOX adsorption onto AuNP surfaces.

3.3 Materials and Methods

3.3.1 Chemicals

Doxorubicin hydrochloride, glutathione, bovine serum albumin and the citrate assay kit were purchased from Sigma-Aldrich (St. Louis, MO). Polystyrene 96-well plates were purchased from Corning Inc. (NY) and microcentrifuge tubes (cat. no. 02-681-284), ethanol, methanol, and NaCl were purchased from Fisher Scientific (Ottawa, ON, Canada). KBr spectrograde powder was purchased from International Crystal Labs (Garfield, NJ). HEPES salt and trisodium citrate were purchased from Alfa Aesar (Parkridge Rd Ward Hill, MA). 7-Deoxy doxorubicin aglycone was purchased from Toronto Research Chemicals Inc. and anthracene was supplied by J.T.Baker chemicals. DOX-M was synthesized following reported protocols and confirmed with NMR and mass spectrometry (Liang et al., 2014). AuNPs were synthesized via the well-established citrate reduction method (Frens, 1973). Nanopure 18.2MΩ cm water was used in all experimentation.

3.3.2 Doxorubicin Quantification

Un-adsorbed or “free” doxorubicin was quantified by fluorescence measurement in all experimentation using excitation/emission wavelengths of 480/580 nm. These “free” values were subsequently converted to molar concentrations using calibration

curves for doxorubicin to determine the number of loaded or desorbed drug molecules per AuNP. Fluorescent measurements were carried out in 96-well plates. For quantitative studies, polyethylene glycol was included in the plate well buffer to inhibit non-specific sorptive loss of DOX as recently reported on by our group (Curry et al., 2015). In all experimentation, doxorubicin fluorescence (excitation/emission: 480/580 nm) and AuNP UV-Vis absorbance was quantified using a TECAN infinite M10000 PRO micro-plate reader.

3.3.3 Adsorption Kinetics and AuNP Aggregation

In order to study the kinetics of DOX adsorption onto the nanoparticle surface, fluorescence of a DOX sample (90 μL) was measured for six minutes before the addition of AuNP (10 μL, ~10 nM or ~30 nM). To study the effect of DOX on AuNP aggregation, DOX solutions of various concentrations were added to wells containing a constant volume of AuNP (10 nM) before recording the absorbance spectra.

3.3.4 DOX Adsorption Isotherm

For all adsorption studies, equal volumes of DOX solution (dissolved in nanopure H_2O with different concentrations) and gold nanoparticles were used to ensure uniform surface coverage (Darby and Le Ru, 2014). Typically, the DOX and AuNP solutions were mixed in 1.5 mL microcentrifuge tubes and centrifuged at 12,700 rpm for 4 minutes to form DOX-AuNP conjugate precipitates. Thereafter, 20 μL of the supernatant solution (containing "free" DOX) was carefully transferred to plate wells each containing 80 μL of HEPES-PEG 20K buffer solution (final PEG 20K concentration: ~50 mM, final HEPES concentration: 4-80 mM, where 80 mM HEPES buffer was used to maintain the

sample pH to avoid pH dependent fluorescence variation). To test the effect of pH on adsorption, 3 μL of pH citrate buffer (0.3 M, various pH values) was added to DOX solutions prior to mixing with the AuNP solution. To evaluate the effect of salt on adsorption, NaCl (up to 5 μL) was added to the DOX solution prior to mixing with the AuNP solution. In these studies, AuNPs were first rinsed with Nanopure water to remove residual salt during AuNP synthesis. This step helped to prevent AuNP aggregation due to solvent-salt synergistic effects (Han et al., 2011). For EDTA effect on DOX adsorption, EDTA (2 μL, 100 μM) was added to AuNP (25 μL, 13 nM) prior to the addition of DOX (25 μL, 4 μM). Adsorbed DOX was calculated using DOX fluorescence in the supernatant. The calibration was performed using freshly prepared DOX standard solutions with the HEPES-PEG buffer.

3.3.5 Adsorption of DOX Analogs

To study the adsorption kinetics of DOX analogs onto AuNPs, fluorescence kinetic measurements were conducted. Briefly, 88 μL of HEPES buffer (5 mM, pH 7.6) was added to a 96-well plate followed by 2 μL of stock analog solution in EtOH. Fluorescence measurements were recorded every 30 sec, and after 150 sec, 10 μL of AuNP (10 nM) was added and gently mixed into the wells using a pipette. Nanopure water rather than AuNP was added to the control wells. All data were normalized to 100% fluorescence representing the initial fluorescence intensity measured in each well prior to the addition of AuNP. Fluorescence spectra were measured using the following excitation/emission wavelengths (nm): DOX: 480/580, DOX-M: 490/586, DeoxyDOX: 490/576, Anthracene: 252/376.

3.3.6 Desorption Studies

To evaluate the effects of pH, temperature, salt, and solvent concentrations on DOX desorption, drug-nanoparticle conjugates were prepared in equal volumes (as mentioned previously). In desorption studies, a drug-to-nanoparticle concentration ratio of ~300:1 was used to ensure ~100% adsorption of DOX onto AuNP (as evidenced by the near total quenching of DOX at this ratio). After mixing AuNP and DOX (both prepared in nanopure water without buffer) in 1.5 mL tubes, the conjugate samples were treated with pH buffer (2 μL, 0.35 M, various pH values), solvent (ethanol, methanol, 25 μL), or temperature (15 min exposure). For the temperature effect studies, high temperature samples were submerged in a water bath with water temperature monitored using a thermocouple. Samples treated at 4°C and 25°C were achieved by keeping conjugate solutions in a refrigerator (4°C) or bench top (room temperature:~ 25°C) for 15 min, respectively. For $MgCl_2$ –ethanol desorption studies, AuNP were rinsed prior to treatment to decrease previously mentioned solvent-salt synergistic effects. Conjugate samples were again centrifuged at 12,700 RPM to form AuNP precipitates and resultant supernatant samples were analyzed for DOX concentration as outlined above. To study the displacement of DOX from AuNPs by anthracene, increasing concentrations of aqueous anthracene solutions were added to wells containing DOX-AuNP conjugates with equivalent volumes of nanopure water used in control groups. DOX-AuNP conjugate fluorescence measurements were taken for several min prior to the addition of anthracene. For both GSH and BSA-induced DOX desorption studies, DOX and AuNP were mixed in 96-well plates prior to fluorescence measurements. Different concentrations of GSH and BSA solutions were then added to plate wells and mixed by

pipetting before subsequent fluorescent measurements at excitation/emission: 480/580 nm.

3.3.7 Citrate Assay

DOX-AuNP conjugate mixtures (1153:1 drug-to-nanoparticle molar concentration ratio) and AuNP controls were prepared as outlined above. The mixtures were centrifuged and the citrate concentration in the resulting supernatant solution was quantified using a citrate assay kit as per manufacturer's directions (Sigma Aldrich, Catalog Number: MAK057). Following an enzymatic reaction, the concentration of free citrate in solution correlated to the production of a fluorescent marker dye. The resultant citrate concentrations in the supernatant solutions were calculated by comparing the sample fluorescence to fluorescence values obtained from known citrate standard solutions provided in the kit.

3.3.8 Infrared Spectroscopy

Fourier Transform Infrared Absorption Spectra were obtained by a Thermo Nicolet 6700 FT-IR Spectrometer. DOX-AuNP conjugate mixtures (1538:1 concentration ratio) and AuNP mixtures were prepared in microcentrifuge tubes (n=12). Following repeated centrifugation and rinsing steps, precipitate solutions were combined and allowed to dry in light-protected weigh boats for 48 h. Subsequently, 150 mg of KBr was added to each of the samples before being pressed into round pellets and dehydrated. The samples were analyzed using the infrared spectrometer (samples measured against KBr, 256 scans per sample, 4 cm^{-1} resolution). Spectra baselines were corrected using OMNIC software.

3.3.9 X-Ray Photoelectron Spectroscopy

Silicon substrates were sonicated in acetone for 10 minutes prior to drying. For AuNP samples, AuNP were concentrated via centrifugation and directly dropped onto the surface of the silicon substrate. For DOX-AuNP sample, AuNP were mixed with aqueous DOX and concentrated via centrifugation. To maximize the amount of sample recovered, DOX-AuNP conjugates were briefly sonicated to remove adsorbed conjugates from the microcentrifuge tube surface before being directly dropped onto the silicon substrate. Prior to analysis, samples were allowed to dry in a fume hood overnight. XPS analyses were performed using a Thermo-VG Scientific ESCALab 250 Microprobe equipped with a monochromatic Al Ka X-Ray source (1486.6 eV). All spectra were processed and analyzed using CasaXPS software.

3.3.10 Transmission Electron Spectroscopy

TEM micrographs were obtained using a Phillips CM30 microscope operated with an accelerating voltage of 250 kV. As-prepared AuNP and DOX-AuNP conjugate solutions were dropped onto lacey carbon-coated TEM grids and imaged at various magnifications.

3.3.11 Theoretical Investigations

To thoroughly understand interactions between DOX and AuNP observed empirically, we modeled molecular dynamics (MD) varying influences of functional groups under experimental conditions. The DOX pdb file was obtained from the Drug Data Bank and the hydrogens were added using MarvinSketch software (version 15.6.29.0, 2015, ChemAxon (http://www.chemaxon.com)). The AuNP pdb file was made

with OpenMD nanoparticle builder with forcefield SuttonChen along the lattice constant of gold, 4.08 Å. The AuNP pdb and DOX pdb were imported into MarvinSketch and merged into one system. The modelling was made using MOPAC2012 at PM7 level of theory (Maia et al., 2012). The visualization and analysis of quantum calculations were made using Gabedit (Allouche, 2011). The obtained geometry optimization output file was used for 10 ns molecular dynamic (MD) modelling of the ground state geometry with universal forcefield (UFF) (Rappe et al., 1992). MarvinSketch was used for drawing, displaying and characterizing chemical structures, substructures and reactions.

3.4 Results and Discussion

3.4.1 Adsorption of DOX on AuNPs

The adsorption of DOX on AuNP surfaces was studied by fluorescence measurement, where AuNPs serve as an excellent quencher of the fluorescence signal of DOX upon adsorption via nanoparticle surface energy transfer (NSET). Isotherm data in Figure 3.2A depicts a Langmuir adsorption behavior with maximum DOX loading of ~ 550 drug molecules per AuNP (citrate capped, ~13 nm in diameter), indicating monolayer adsorption of DOX on the AuNP surface (Zhang et al., 2012c). The adsorption process was complete in less than 30 seconds (Figure 3.2B), suggestive of diffusion-limited kinetics.

Meanwhile, DOX adsorption was accompanied by an aggregation of AuNPs, characterized by color change of the AuNP solution from wine red to purple, as shown in the red-shifted absorbance spectra (Figure B.1) and TEM images of DOX-AuNP conjugates (Figures B.2-4). One explanation may be that when DOX adsorbs onto the

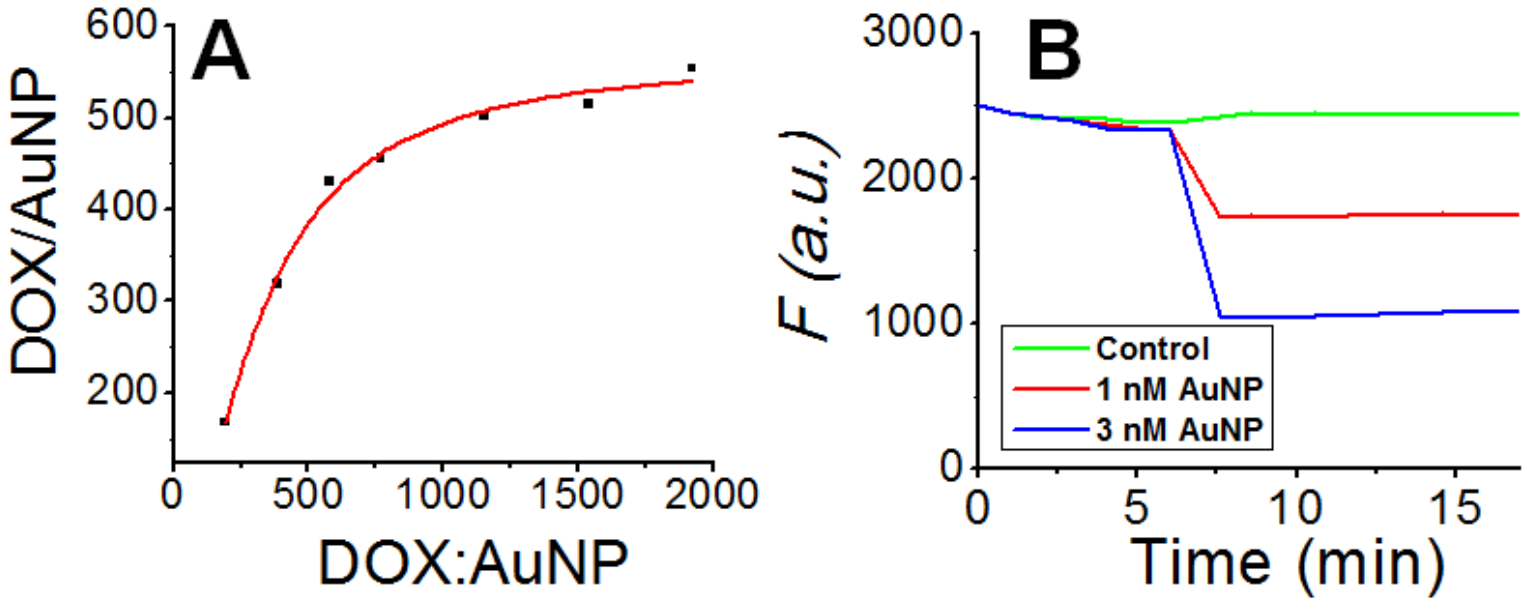

Figure 3.2 (A) DOX–AuNP isotherm including Langmuir Fit (solid line). See Fig. S7A† for original data with standard errors. (B) DOX fluorescence decrease upon addition of AuNP.

surface of the AuNPs, the negatively charged citrate anions, originally adsorbed on AuNP surfaces and providing electrostatic stabilization, are replaced by DOX. Such replacement may destabilize AuNPs in solution by decreasing repulsive forces, resulting in AuNP aggregation due to gold's high density and strong van der Waals forces between particles in solution (Doane and Burda, 2013). Another mechanism may be due to salt-bridging of the negatively charged citrate-coated AuNPs by DOX via its amine group, which is positively charged under neutral pH regimes. To verify these hypotheses, we monitored the displacement of citrate from AuNP surface by DOX using fluorescence spectroscopy. The results indicated that ~ 505 citrate ions were replaced by DOX molecules from each AuNP surface (Figure B.5). Considering the size and charge of citrate and the surface area of each AuNP, most of the adsorbed citrate molecules were replaced by DOX molecules. Despite the persistent existence of citrate on the surface of AuNPs, as pointed out by J. Park *et al.* (Park and Shumaker-Parry, 2015), essentially most DOX molecules were adsorbed directly on AuNP surfaces, discrediting the salt-bridge mechanism.

The replacement of citrate by DOX (Figure 3.3) was further supported by the results obtained with Fourier Transform Infrared Spectroscopy (FTIR). Spectral analysis of the DOX-AuNP conjugates and citrate-AuNP reveals the existence of much more free citrate (a pronounced peak at 1394 cm^{-1}) in the DOX-AuNP samples than in the citrate-AuNP sample (Figure B.6) (Park and Shumaker-Parry, 2014) In addition, the adsorption of DOX on AuNP surfaces was distinctive, as evidenced by a larger peak at 1589 cm^{-1}, assigned to the C=O bond at the 13-keto position of DOX (Barick et al., 2010).

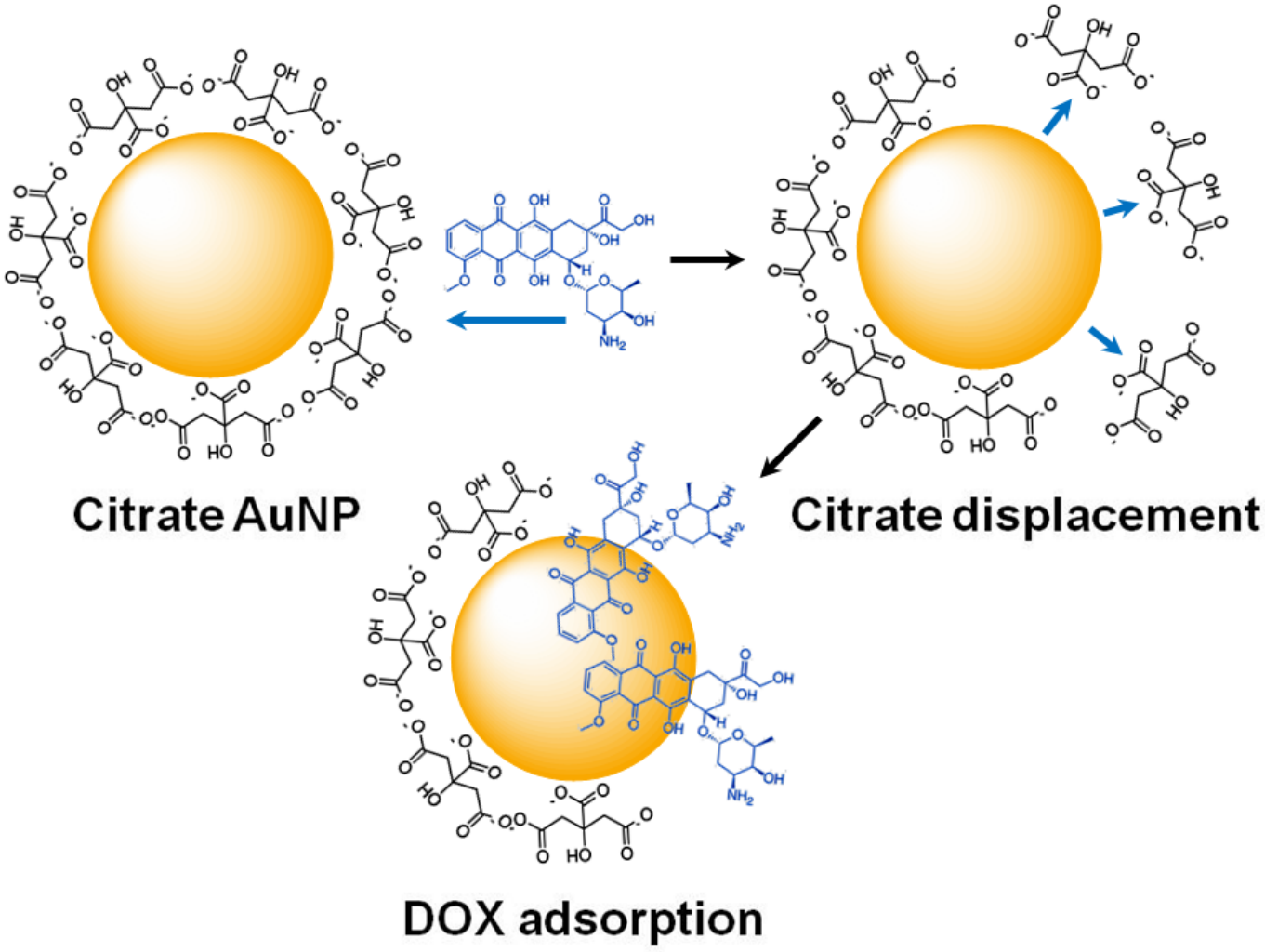

Figure 3.3 Citrate displacement from AuNP surface upon addition of DOX.

A further question is to identify the driving force underlying DOX adsorption. We assume that electrostatic attraction (between the citrate anions on AuNPs and the positively charged amine group in DOX) may drive the DOX to approach AuNP surfaces, thus facilitating their adsorption even though the DOX-AuNP interaction itself was not based on a salt-bridging mechanism (Zhang et al., 2012a; Zhang et al., 2012b, c). To evaluate this hypothesis, we studied the effect of NaCl concentrations and solution pH on DOX adsorption. When adding DOX solution spiked with various NaCl concentrations into the AuNP solution (volume ratio 1:1 which is critical to ensure fast mixing and even DOX adsorption onto each AuNP), the results indicated no decrease in DOX adsorption capacity even with 136 mM NaCl in the solution (Figure 3.4A), suggesting high Na^+ concentrations did not interfere with DOX adsorption, confirming adsorption was not driven by electrostatic attraction (Darby and Le Ru, 2014).

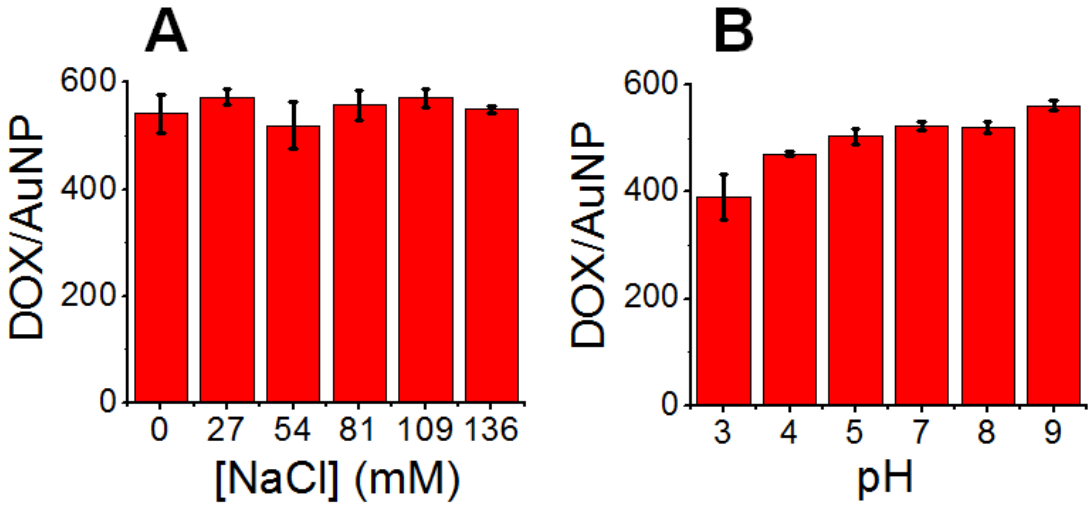

Figure 3.4 Adsorption of DOX onto AuNP in presence of varying NaCl concentrations (A) and pH environments (B).

As shown in Figure 3.4B, similar results were observed with pH influences. Lower pH values (e.g., pH 3) promote complete protonation of DOX, decreasing DOX adsorption slightly (< 10%), while providing further evidence against the salt-bridging electrostatic mechanism. These findings were further confirmed with the results of desorption experiments, where the increase in DOX fluorescence signal due to dissociation of DOX-AuNP conjugates was monitored under various pH conditions. Herein, low pH environments facilitated more desorption (~10%) than alkaline environments (Figure 3.5A). Since adjusting pH is an effective means to alter the charge states of the species involved, again, our results disfavor the electrostatic attraction-based adsorption theory. Instead, the pH effect could be explained if DOX adsorption was driven by hydrophobic forces, where at lower pH, DOX molecules were completely ionized and displayed less hydrophobicity, resulting in lower adsorption and higher desorption, similar to the effect of pH on DOX adsorption onto carbon nanotubes (Liu et al., 2007).

As shown in Figure 3.5B, when using solvents with decreasing polarity (pure water, 33% methanol, and ethanol aqueous solutions), more DOX molecules were desorbed from AuNP surfaces to the solvent, suggesting DOX hydrophobic functional groups are involved in the interaction with AuNPs, consistent with the pH effect. Next, DOX-AuNP conjugates were subject to increasing temperatures, which enhanced DOX desorption from AuNP surface (Figure 3.5C). These results suggest desorption of DOX from AuNP surfaces is an endothermic process; conversely, adsorption is exothermic and spontaneous in nature, consistent with previous work on anthracene and benzene adsorption onto AuNP surfaces (Kumar et al., 2002). All experimental results indicate

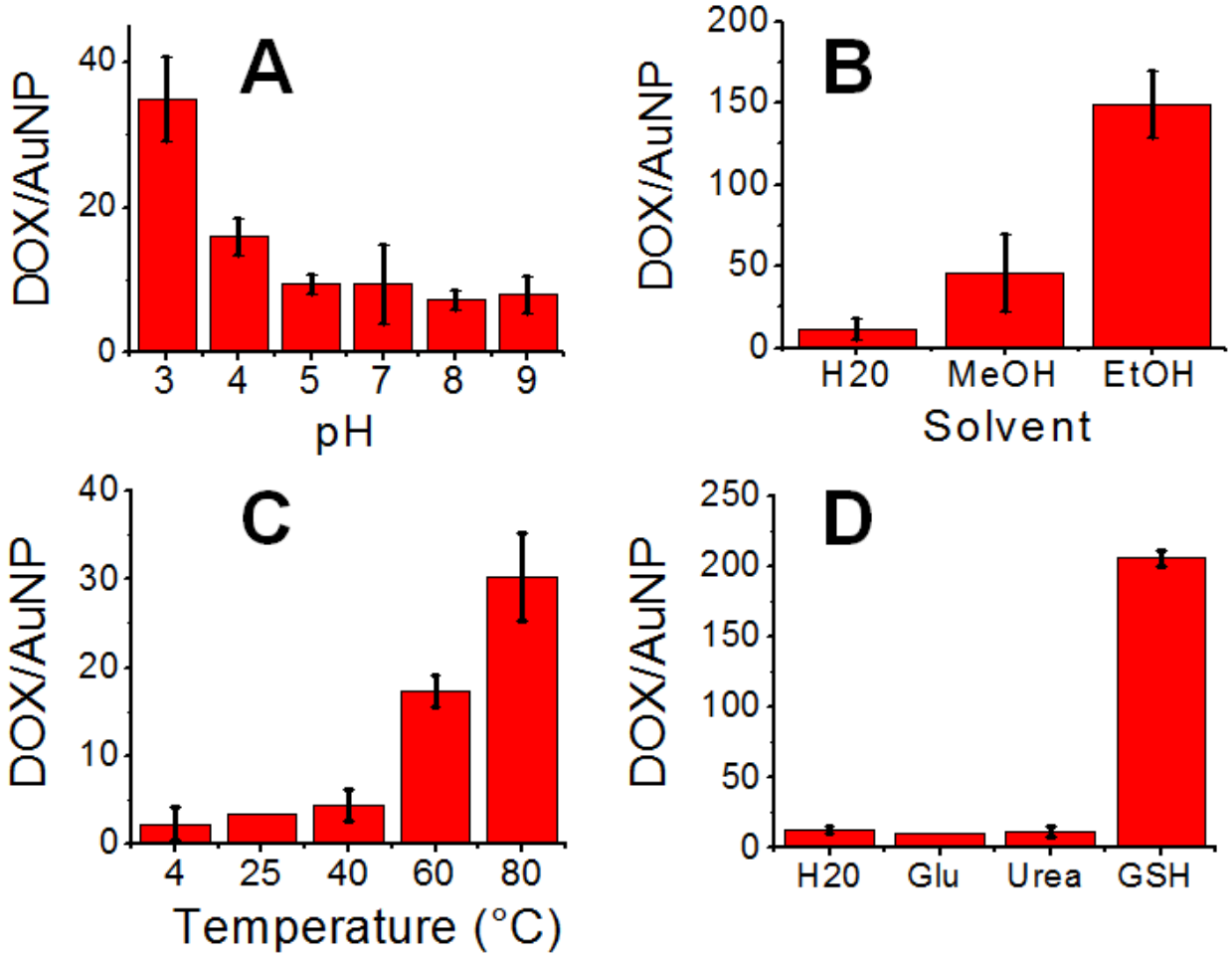

Figure 3.5 DOX desorption from AuNP in presence of varying pH (A), solvent (B) and thermal (C) conditions. (D) DOX desorption from AuNP upon addition of competitive molecules ([Glu], [urea] = 45 mM, [GSH] = 182 μM.

DOX adsorption was not driven by electrostatic interaction, but rather by hydrophobic forces.

3.4.2 Identification of the molecular functionalities contributing to DOX AuNP interaction

To identify which DOX functional groups contribute to its adsorption, we studied the interaction between AuNP and compounds sharing structural similarities to DOX (Figure 3.6). These analogs include anthracene (ANT), 7-deoxy doxorubicin aglycone (DDA), D-glucose (Glu), Urea, decanoic acid modified DOX (DOX-M) and glutathione (GSH), a thiolated compound, for comparison. The results showed that even high concentrations (45 mM, ~10,000 times DOX concentration) of glucose and urea were unable to displace DOX from AuNP surfaces (Figure 3.5D), while comparable levels (μM level) of anthracene could replace DOX (Figure 3.7A). Adsorption kinetics experiments further confirmed ANT, DDA, and DOX-M all adsorbed on AuNPs (Figure 3.7B) with even higher affinities for AuNP surfaces than possessed by DOX. This clearly demonstrates the amine group does not contribute to DOX-AuNP interactions, which is in agreement with the characterization of DOX-AuNP conjugates with x-ray photoelectron spectroscopy (XPS).

As illustrated in Figure B.8, N 1s and C 1s XPS spectra for DOX-AuNP clearly show binding energy peaks at 402.11, 400.08 eV (Figure B.8A), and 285.40 eV (Figure B.8B) in the de-convoluted peaks, attributable to the free amine and C-N groups of DOX, but not Au-N coordination, as it is well established that the binding energy of N 1s decreases by 1-3 eV upon binding to metallic surfaces due to a transfer of electron density from nitrogen to metals (Li et al., 2004; Mondal et al., 2015). Taken together, we reason that

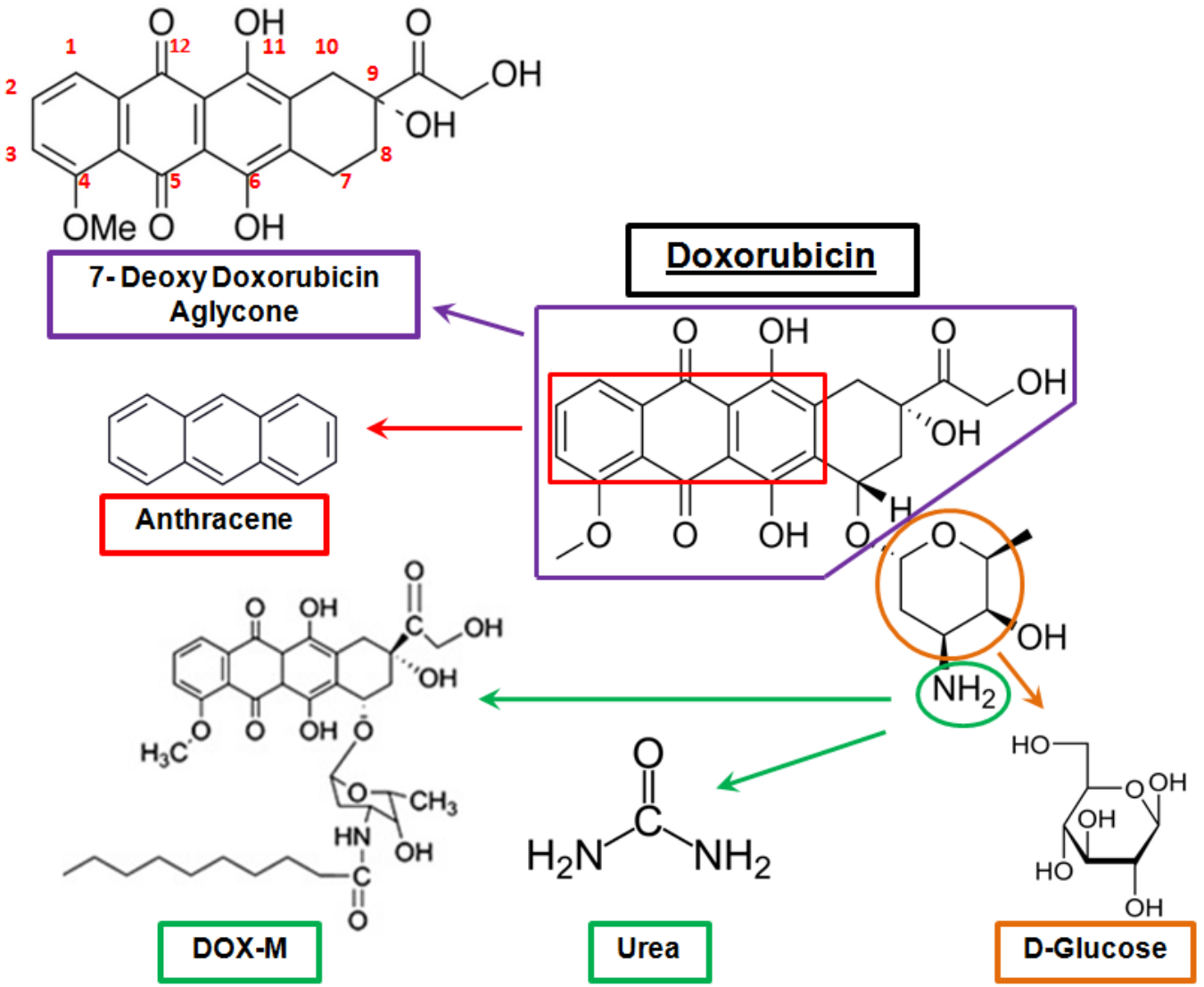

Figure 3.6 Chemical compounds used in this work mimicking potential DOX functional groups of interest in AuNP adsorption.

DOX adsorption onto AuNP surfaces is via the anthracene ring due to cation-π-interactions with the adsorbed Au^{+} on AuNP surfaces, similar to previous studies on the adsorption of benzene and anthracene onto AuNP surfaces (Kumar et al., 2002; Pagliai et al., 2012). $MgCl_2$ induced desorption (Figure B.7B) further strengthened this hypothesis since Mg^{2+} ions may create cationic competition for DOX. Although desorption is not highly pronounced, the result is reasonable since it is the hydrophobic force rather than cation-π- interaction that drives DOX to the AuNP surface.

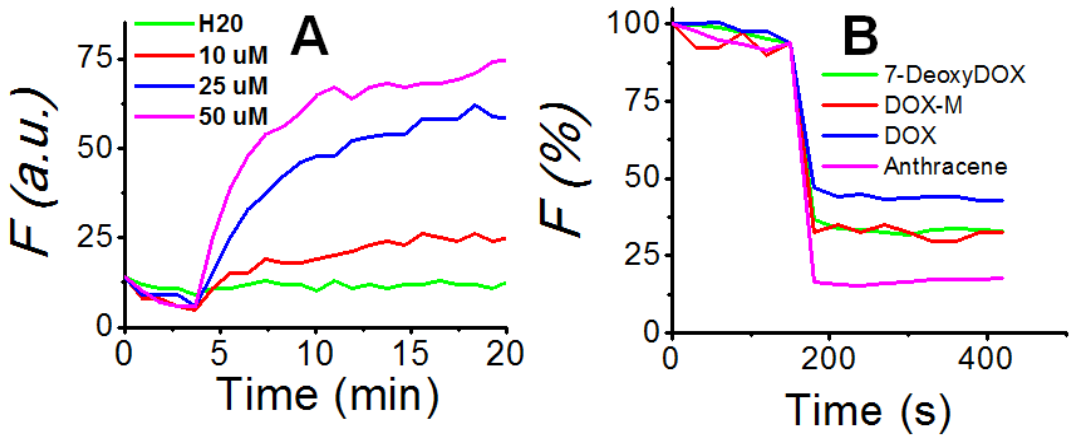

Figure 3.7 (A) Fluorescence intensity of DOX from DOX–AuNP conjugates upon addition of anthracene. (B) Fluorescence intensity of compounds structurally analogous or with relevant functional groups to DOX molecules upon addition of AuNP.

In addition, ethylenediaminetetraacetic acid (EDTA) was shown to inhibit DOX adsorption onto AuNPs (Figure B.7C), presumably due to the coordination of Au^{+} ions by EDTA, leaving less Au^{+} available for DOX to interact with. The use of EDTA in this context comes with limitations related to charge repulsion. The negative charge associated with EDTA makes it difficult for coordination with Au^{+} due to the negative citrate layer on AuNP. Nevertheless, the results of the $MgCl_2$ and EDTA experiments

support the cation-π- interaction theory. This hypothesis was further substantiated with modelling work.

3.4.3 Modelling of the DOX-AuNP Interaction

Theoretical models describing the interaction between AuNPs (assumed 0.5 nm in size to be relatively efficient with quantum mechanics modelling) and DOX were produced (Figure 3.8). The 0.5-nm AuNPs might underestimate the magnitude of the forces that govern the interaction between DOX and 13-nm AuNPs, but would not change the physiochemical nature of the interactions. DOX has 3 carbonyl groups in positions 7, 9 and 10 (Figure 3.8A) which contribute to the stabilization of the molecular conformation through formation of hydrogen bonds with nearby hydroxyl groups (e.g., at positions 9 and 42 as well as 10 and 43). The steric hindrance of C30 may favor hydrogen bonding between 7 and 44, or 7 and 40. Disruption of the proposed hydrogen bonds may increase the ionization potential of DOX, facilitating DOX adsorption to AuNPs (Figure 3.9B). An earlier study reported DOX interactions with nanoscale particles is mainly due to van der Waals forces forming a S-conformation DOX layer on the particle surface (meaning the ring structures are directly interacting with the chitosan particle),(Shan et al., 2014) which is generally consistent with our isotherm data (Figure 3.2A). However, functional groups driving the absorption of DOX were not definitively identified, and may differ when interacting with AuNPs from that with chitosan. To address these issues, we performed quantum molecular dynamics modelling to reveal the detailed mechanism of DOX-AuNP interaction (Figure B.9).

First, we calculated and compared the IR frequencies of DOX (with and without AuNPs) to explain the peak shift observed in FTIR spectra. Without AuNPs, the

stretching vibrational frequency of the carbonyl group of DOX is temperature independent between 200 - 400 °K (Figure 3.9A and B). In the presence of AuNPs, the carbonyl stretch peak shifted to a higher frequency (Figure 3.9C). In addition to this up-field frequency shift, the peak of the carbonyl stretch splits due to the different carbonyl functionalities, in other words, the carbonyls on the ring and on the ketone may interact with AuNPs differently. Further, the intensity of the carbonyl stretch in ketones decreased drastically, indicating the carbonyl groups (positions 7, 9 and 10 in Figure 3.8A) are involved in DOX-AuNPs interactions. Similarly, the shift of frequency-fingerprint of the C=C of the anthracene ring (~1600 cm^{-1}) demonstrates the involvement of the ring structure in the AuNP-DOX interaction (highlighted region in Figure 3.9). In contrast, the possibility of binding between the DOX amine group and AuNP via Au-N bonds is low, as evidenced by the low peak intensity of 386 cm^{-1}, the frequency of Au-N bond stretching.

To further identify the contribution of each DOX functional group to its adsorption onto AuNP, molecular dynamics (MD) and quantum mechanics (QM) were employed to model the ground state conformations of the DOX-AuNP system. We constructed three models to differentiate the contribution of the amine group in the sugar ring from that of the anthracene ring. In model 1, we compared the binding of DOX molecules with that of their analogue lacking the amine group. The model demonstrated an 8.3% probability that ring 5 (the sugar ring containing the amine group) bends toward AuNP surfaces, potentially forming an Au-N bond. However, this bending phenomena was persistent with the DOX analog lacking the amine group in ring 5, suggesting the bending of DOX is not due to the formation of an Au-N bond, but likely attributable to

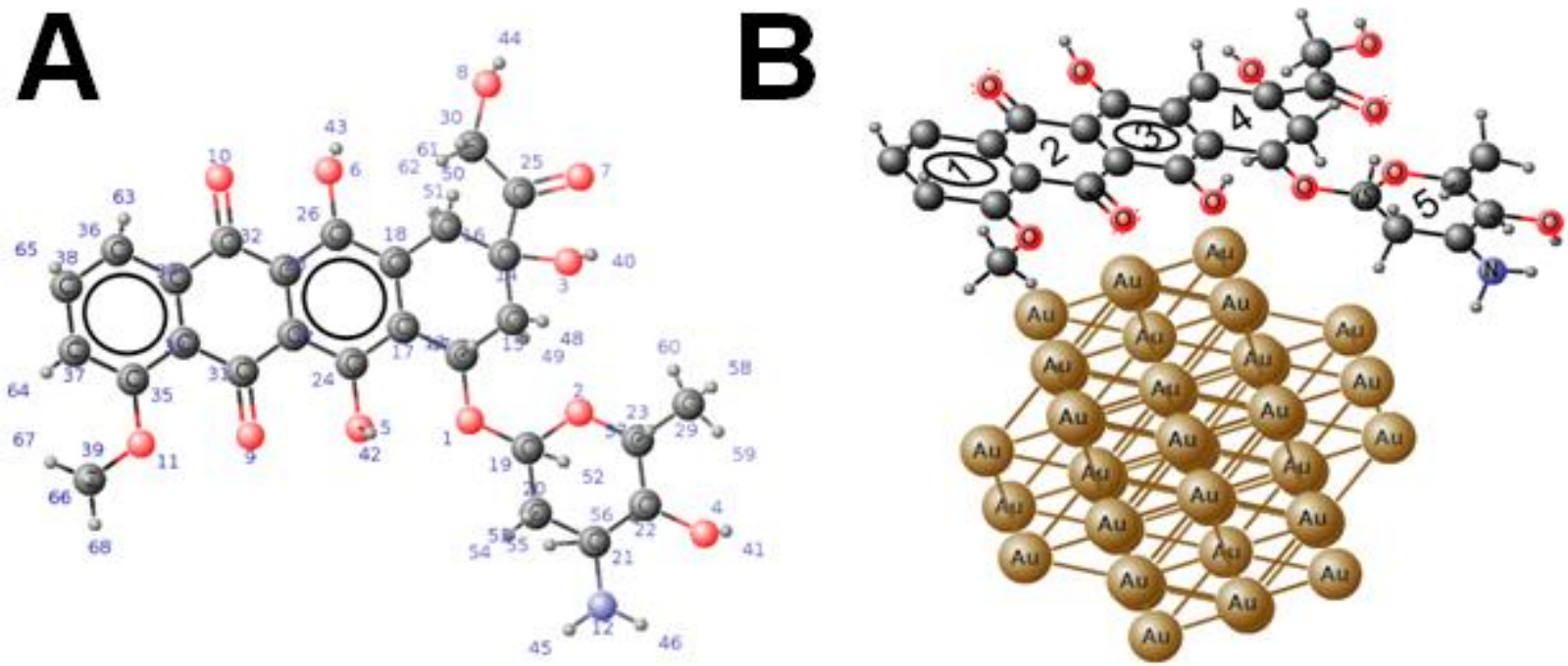

Figure 3.8 (A) Structure of doxorubicin and (B) Doxorubicin with gold nanoparticles.

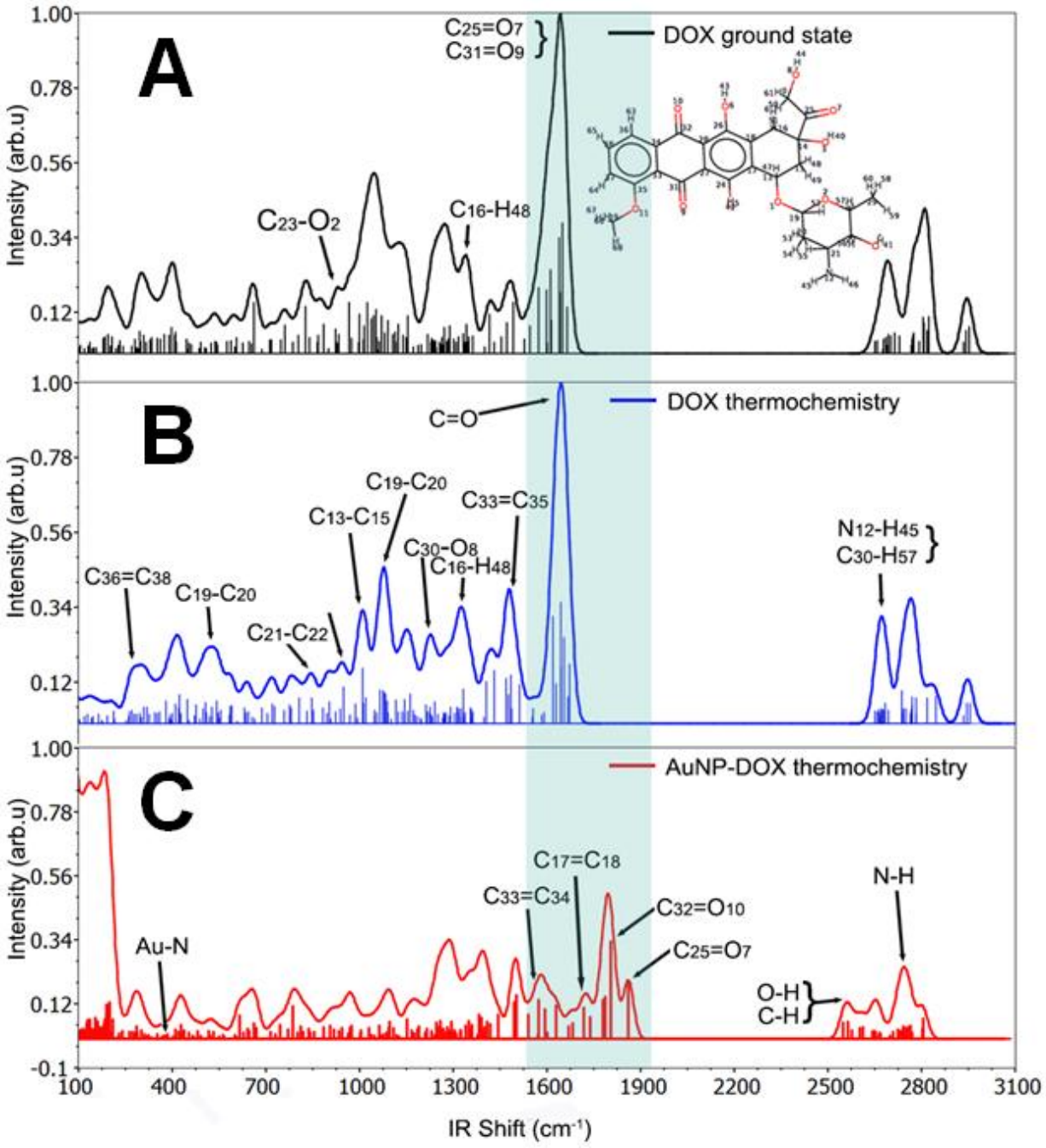

Figure 3.9 The IR spectrum showing the peak shifts in DOX in ground state at room temperature (A), excited state with increased temperature (B) and DOX–AuNP conjugates (C). Features are labelled in the figure.

π - σ attraction (where the σ bonds were from ring 5) that dominated the edge to face interaction (Hunter and Sanders, 1990).

In model 2, we evaluated the contribution from ring 5 and the carbonyl groups in ring 2 by applying a DOX analog lacking ring 5 to the AuNP (Figure B.10A); the results demonstrated electrostatic interaction between the carbonyl of ring 2 and the AuNP surface. Next we modelled how AuNPs interact with anthracene, a DOX analog with only the rings 1-3 (model 3). In this model, DOX interacted with AuNPs by cation - π interactions (Figure B.11) between the Au^{+} cations adsorbed on the AuNP surface, and anthracene rings 1 and 3. The AuNP–anthracene interaction appeared with low frequencies (< 400 cm^{-1}) and involved the puckering of the ring observed through the peak at ~680 cm^{-1}(Figure B.10B), where the =C-H bending appeared.

The DOX analog without ring 5 adsorbed on AuNP surface showed low carbonyl group stretching frequencies (Figure B.10A), attributable to the direct anchoring of the two carbonyl groups (located on ring 2) to the AuNP surface. The carbonyl-Au coordination facilitates the cation - π interaction of rings 1 and 3 on the AuNP surface, synergistically contributing to the overall force of the DOX–AuNP interaction.

Combining the experimental work and theoretical modelling, we conclude the main forces that contribute to DOX adsorption onto AuNPs consist of π-cation interactions and Au-carbonyl coordination chemistry (Figure 3.10C). Nevertheless, it is reasonable to expect contributions from intermolecular forces such as electrostatic attraction between DOX and residual citrate molecules (Figure 3.10A) and hydrogen bonding between several DOX molecules (Figure 3.10B). Considering the DOX

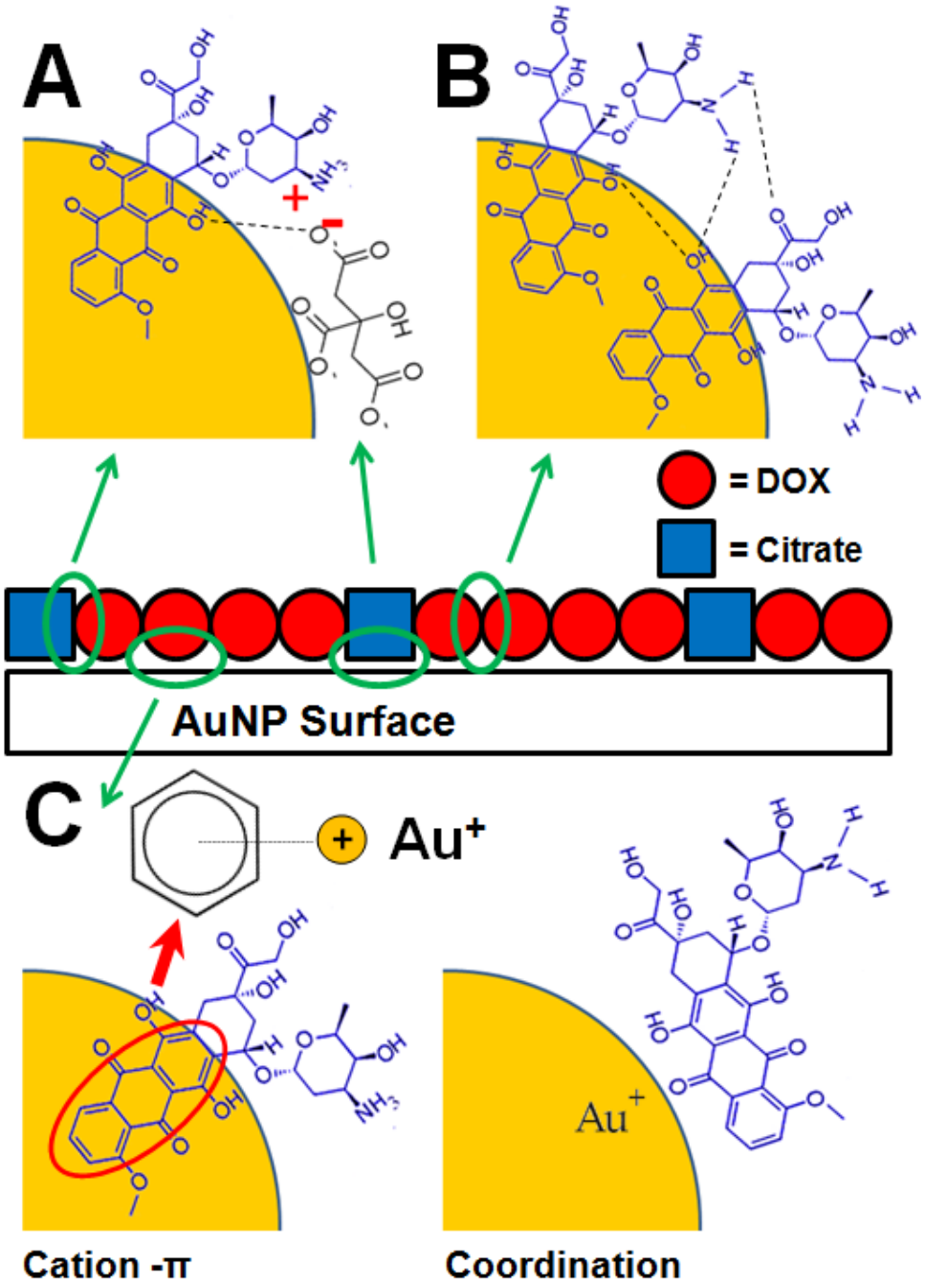

Figure 3.10 (A) Electrostatic interaction (+-) and hydrogen bonding (—) between adsorbed citrate and adsorbed DOX molecules on AuNP surfaces. (B) Hydrogen bonding between adsorbed DOX molecules on AuNP surface. (C) Cation–π and coordination chemistry between DOX and AuNP.

adsorption with intermolecular interactions, the adsorbed DOX and a small number of residual citrate molecules form an assembled monolayer structure, impairing the charge-based stabilization of AuNPs due to decreased net surface charge relative to the original citrate-capped AuNPs.

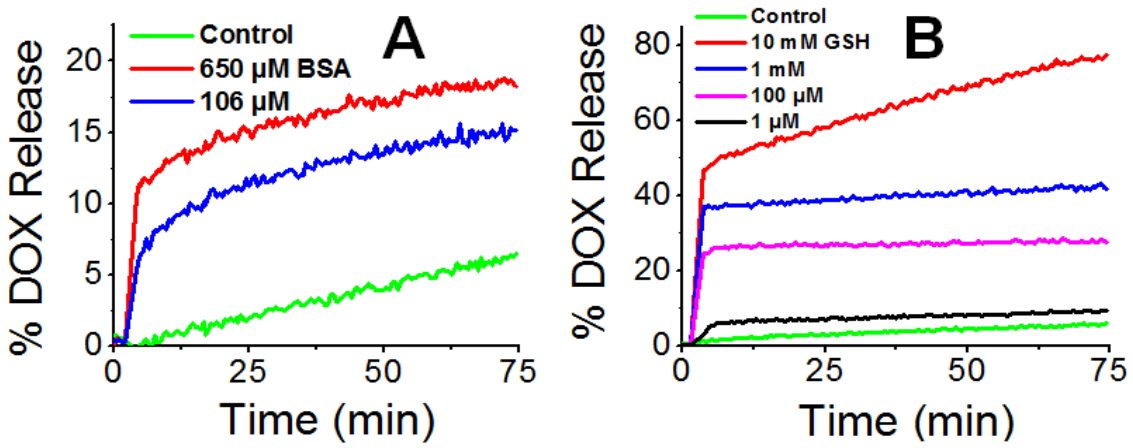

Figure 3.11 BSA (A) and GSH (B) induced DOX fluorescence signal increase via desorption from AuNP surface.

To examine the strength of the DOX-AuNP interaction, we evaluated DOX desorption in the presence of bovine serum albumin (BSA) and GSH, both of which are present in high concentration in blood and cytoplasm. BSA adsorbs on citrate-AuNPs through a mixed mechanism involving electrostatic, hydrophobic, and coordination chemistry while GSH adsorbs to AuNPs via thiol-gold bonds (Brewer et al., 2005; Gao et al., 2012). Our results demonstrate GSH could displace DOX rapidly and efficiently (~70% replacement over 60 min), demonstrating that the thiol-gold bond is stronger than the forces governing DOX-AuNPs interactions (Figure 3.11B, Figure 3.5D). BSA also facilitated DOX desorption, although not as efficiently as GSH with ~ 18% DOX desorbed in the presence of ~0.7 mM BSA over 50 min (Figure 3.11A). Such DOX

displacement by common blood-borne constituents are significant for *in vivo* drug delivery research, since the concentrations of GSH (μM level in blood and mM level in cytoplasm) and BSA (~ 0.7 mM in blood) used in this study were physiologically relevant.

3.5 Conclusions

In summary, for the first time, we provide both empirical and theoretical evidence demonstrating the mechanism of DOX adsorption onto AuNP is based on cation- π interactions and formation of a DOX monolayer on the nanoparticle surface. DOX adsorption is proposed as a two-step process where hydrophobic forces first drive DOX molecules toward the AuNP surface prior to cation–π interactions and coordination chemistry between DOX and the cationic surface of AuNP anchoring DOX to AuNP surface and replacing most of the citrate molecules. Contrary to the conventional understanding, the contribution of the amine group in DOX to AuNP adsorption is negligible, though together with the hydrogen bonding as an intermolecular force, it may contribute to the formation of an adlayer on AuNP with residual citrate. Physiologically-relevant molecules (GSH and BSA) were shown to rapidly desorb DOX from the nanoparticle surface at physiological concentrations, an important point to consider for *in vivo* drug delivery and controlled release studies. Despite the simplicity of the DOX-AuNP interaction for drug loading, the nanoconjugate remains vulnerable to these physiological conditions. Stabilization methods such as co-adsorption of DNA or PEG should be considered when employing simple DOX-AuNP chemistry. Considering the volume of research articles dedicated to DOX-AuNP delivery systems, detailed knowledge of the nature of this fundamental interaction may allow researchers to better

design delivery systems and estimate therapeutic drug loading and release parameters, therefore increasing anticancer drug efficiencies both *in vivo* and *in vitro*.

Chapter 4 Conclusions

This thesis furthers the field of nanotechnology by first providing a protocol to enhance the accuracy of doxorubicin quantification in drug delivery studies and second by investigating the interaction mechanism between doxorubicin and citrate-capped gold nanoparticles. Doxorubicin is commonly used as a model drug in cancer studies due to its high toxicity towards cancer cells and also due its ease of use in the laboratory. Having hydrophilic characteristics makes the drug water soluble and therefore easy to incorporate into many nanoscale systems, however, its hydrophobic character allows for non-specific interactions with plastic vessels and surfaces. These interactions, over the course of several minutes can impact quantification measurements of the drug, routinely completed using fluorescence spectroscopy. To solve the problem of non-specific adsorption and the erroneous drug loading values that result, we studied the effect of including trace amounts of polyethylene glycol in the measurement buffer. High molecular-weight polyethylene glycol was witnessed to inhibit non-specific adsorption of doxorubicin to plate well surfaces at trace concentrations, allowing for a rapid and simple method to accurately quantify the concentration of free drug in solution.

Gold nanoparticles have received immense research interest in the field of drug delivery and targeted cancer therapy. With this in mind, we aimed to shed light on the specific nature of the chemical interaction between doxorubicin and citrate-capped gold nanoparticles. As with many doxorubicin-nanomaterial interaction theories, the drug was conventionally thought to adsorb onto AuNPs mainly through electrostatic bridging interactions between the negative citrate capping agent used to synthesis and stabilize the

nanoparticles and the positively charged amine group of DOX. Experimental and theoretical results were presented in Chapter 2 which carefully uncovers DOX adsorption to gold as a rapid, multi-step process whereby hydrophobic forces drive the drug molecule to the surface of the nanoparticle before a combination of cation-π and coordination chemistry anchor the drug to the gold core.

In order for nanoscale-drug conjugates to be successful in animal-based models, several key features must first be optimized. First, the size of the nanoparticle complex must remain "nanoscale" if the delivery vehicle is going to make use of the EPR effect. To this point, the nanoparticle must be stable in the high ionic strength environments present in *in vivo* systems. Secondly, the drug must be anchored to the nanoparticle in a way that allows for controlled release at the target site. The simple adsorption of DOX onto citrate-capped gold nanoparticles provides issues with respect to size, stability and controlled release. Upon adsorption of high concentrations of DOX, AuNP aggregate irreversibly, signifying their instability. Additionally, the aggregated complexes lose their nanoscale character by clustering into large and non-uniform complexes. Despite these facts, much research activity is still devoted to a drug delivery platform utilizing both DOX and gold based-nanomaterials.

Recent advances such as the adsorption of DOX onto and into hollow gold nanoparticles have allowed for promising *in vivo* demonstrations. Still, as shown in Chapter 3, interactions relying solely on the simple adsorption chemistry described here provide problems related to controllable release of the therapeutic cargo. Small molecules such as GSH have been show to rapidly desorb DOX from the nanoparticle surface; considering the high concentrations of GSH and other thiolated compounds in the body,

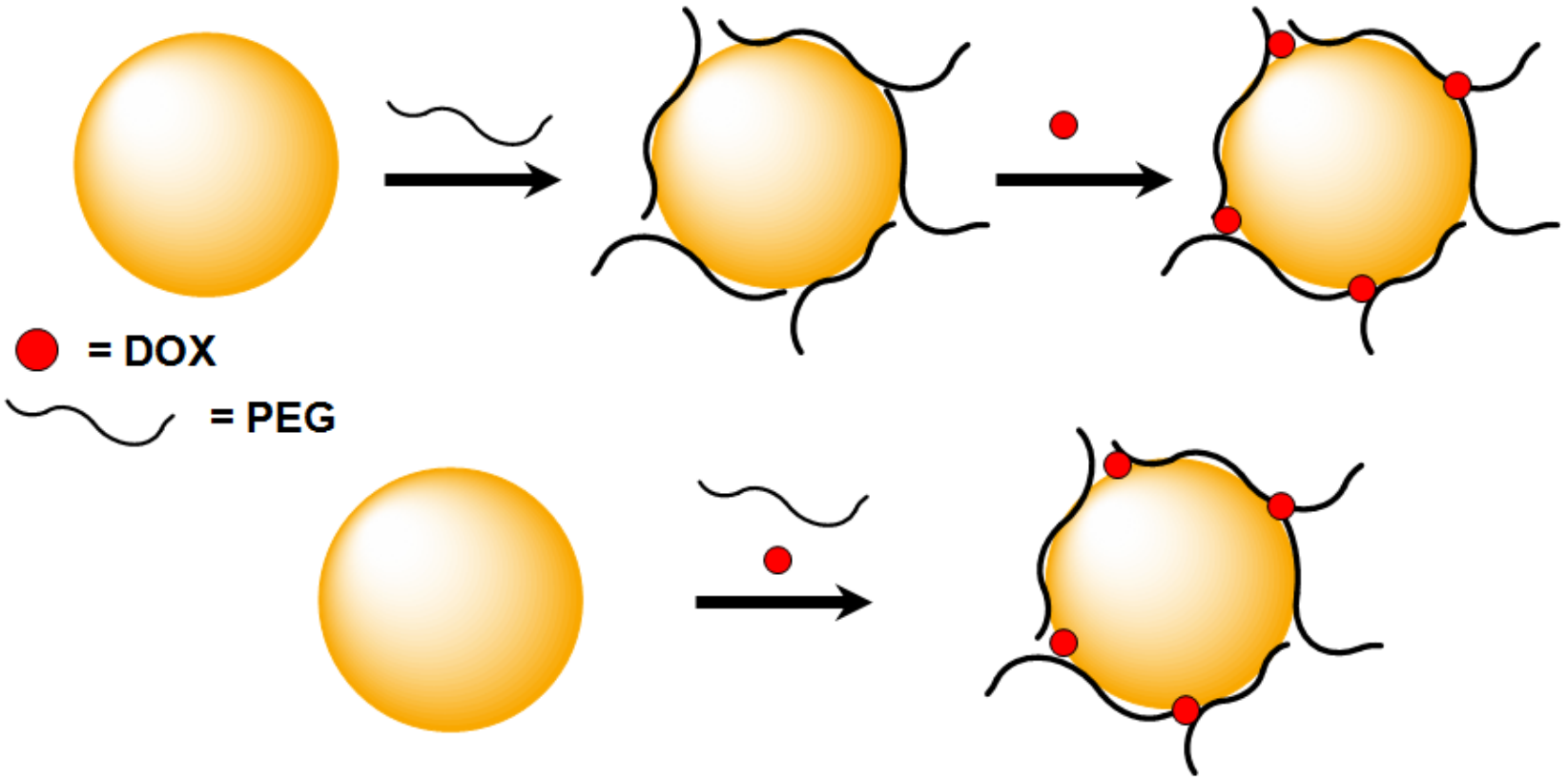

Figure 4.1 Effect of reagent addition order on DOX adsorption and DOX-AuNP stability.

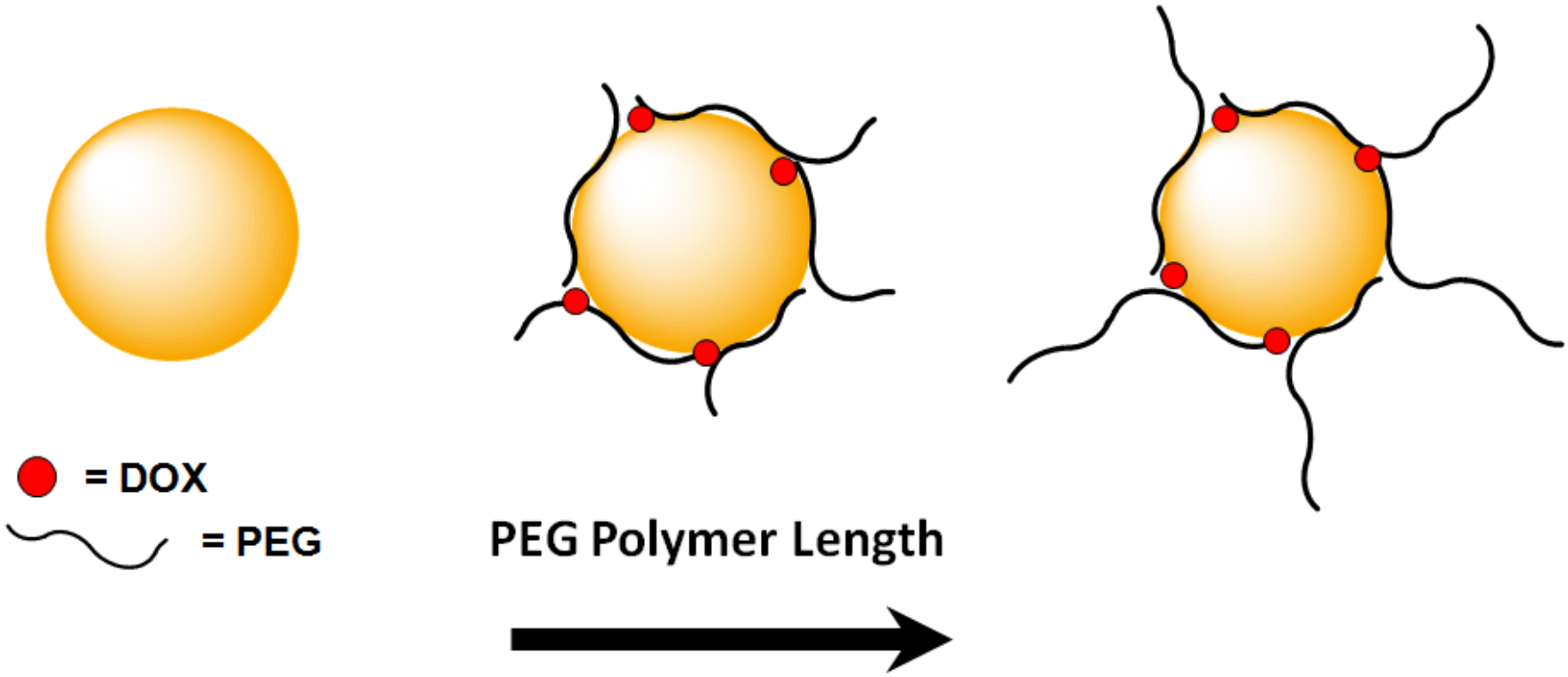

Figure 4.2 Effect of PEG polymer length on DOX adsorption and DOX-AuNP stability.

the controllable release at specific and targeted sites of interest, a major selling point for nanoscale drug delivery vehicles, becomes more difficult.

With these considerations in mind, several recommendations for future work may be made moving forward. First, if the simple DOX-AuNP interaction is to become successful in clinical settings, the problems associated with controlled release and nanoparticle aggregation must be solved. Previously mentioned work using hollow gold nanoparticles have touched on this through use of thiolated PEG and a stabilizing agent in photothermal-chemotherapy. Further investigations on thiolated PEG-AuNP vehicles for DOX delivery may prove useful. Systematic research investigating the effect of reagent addition order (Figure 4.1) and PEG polymer length (Figure 4.2) may allow for advances with respect to the extent to which controllable release is achievable.

Finally, the inclusion of nanoscale gold into a combinatory therapeutic approach to cancer may also prove beneficial from a clinical point of view. The advent of promising gold-based nanomaterials, such as biodegradable gold liposomes, may present an opportunity to include DOX into novel nano-systems, considering the ubiquitous nature of liposomal doxorubicin in cancer treatment today. Additionally, such innovative investigations may pave the way for researchers to translate combinational chemo, radio and photothermal therapies from the bench to the bedside.

References

Acharya, M.M., Christie, L.-A., Lan, M.L., Donovan, P.J., Cotman, C.W., Fike, J.R., Limoli, C.L., 2009. Rescue of radiation-induced cognitive impairment through cranial transplantation of human embryonic stem cells. Proceedings of the National Academy of Sciences 106, 19150-19155.

Agency, I.A.E., 2010. Radiation Biology: A Handbook for Teachers and Students.

Ahmad, I., Longenecker, M., Samuel, J., Allen, T.M., 1993. Antibody-targeted delivery of doxorubicin entrapped in sterically stabilized liposomes can eradicate lung cancer in mice. Cancer Research 53, 1484-1488.

Akiyama, Y., Mori, T., Katayama, Y., Niidome, T., 2009. The effects of peg grafting level and injection dose on gold nanorod biodistribution in the tumor-bearing mice. J Control Release 139, 81 - 84.

Allen, T.M., Cullis, P.R., 2004. Drug delivery systems: Entering the mainstream. Science 303, 1818-1822.

Allen, T.M., Martin, F.J., 2004. Advantages of liposomal delivery systems for anthracyclines. Semin Oncol 31, 5-15.

Allouche, A.-R., 2011. Gabedit—a graphical user interface for computational chemistry softwares. Journal of Computational Chemistry 32, 174-182.

Anderson, J.E., Hunt, J.M., Smith, I.E., 1981. Prevention of doxorubicin-induced alopecia by scalp cooling in patients with advanced breast cancer. British Medical Journal (Clinical Research ed.) 282, 423-424.

Arcamone, F., Cassinelli, G., Franceschi, G., Penco, S., Pol, C., Redaelli, S., Selva, A., 1972. Structure and physicochemical properties of adriamycin (doxorubicin), in: Carter, S., Marco, A.D., Ghione, M., Krakoff, I.H., Mathé, G. (Eds.), International Symposium on Adriamycin. Springer Berlin Heidelberg, pp. 9-22.

Arvizo, R., Bhattacharya, R., Mukherjee, P., 2010. Gold nanoparticles: Opportunities and challenges in nanomedicine. Expert Opinion on Drug Delivery 7, 753-763.

Aryal, S., Grailer, J.J., Pilla, S., Steeber, D.A., Gong, S., 2009. Doxorubicin conjugated gold nanoparticles as water-soluble and ph-responsive anticancer drug nanocarriers. Journal of Materials Chemistry 19, 7879-7884.

Bagalkot, V., Farokhzad, O.C., Langer, R., Jon, S., 2006. An aptamer-doxorubicin physical conjugate as a novel targeted drug-delivery platform. Angewandte Chemie (International ed. in English) 45, 8149-8152.

Bandak, S., Ramu, A., Barenholz, Y., Gabizon, A., 1999. Reduced uv-induced degradation of doxorubicin encapsulated in polyethyleneglycol-coated liposomes. Pharmaceutical Research 16, 841-846.

Barick, K.C., Nigam, S., Bahadur, D., 2010. Nanoscale assembly of mesoporous zno: A potential drug carrier. Journal of Materials Chemistry 20, 6446-6452.

Baumann, M., Krause, M., Overgaard, J., Debus, J., Bentzen, S.M., Daartz, J., Richter, C., Zips, D., Bortfeld, T., 2016. Radiation oncology in the era of precision medicine. Nat Rev Cancer 16, 234-249.

Beijnen, J.H., van der Houwen, O.A.G.J., Underberg, W.J.M., 1986. Aspects of the degradation kinetics of doxorubicin in aqueous solution. International Journal of Pharmaceutics 32, 123-131.

Bonnet, D., Dick, J.E., 1997. Human acute myeloid leukemia is organized as a hierarchy that originates from a primitive hematopoietic cell. Nat Med 3, 730-737.

Brewer, S.H., Glomm, W.R., Johnson, M.C., Knag, M.K., Franzen, S., 2005. Probing bsa binding to citrate-coated gold nanoparticles and surfaces. Langmuir 21, 9303-9307.

Chatterjee, K., Zhang, J., Honbo, N., Karliner, J.S., 2010. Doxorubicin cardiomyopathy. Cardiology 115, 155-162.

Chen, J., Spear, S.K., Huddleston, J.G., Rogers, R.D., 2005. Polyethylene glycol and solutions of polyethylene glycol as green reaction media. Green Chemistry 7, 64-82.

Chen, X., Gambhir, S.S., Cheon, J., 2011. Theranostic nanomedicine. Accounts of Chemical Research 44, 841-841.

Cheng, Y., C. Samia, A., Meyers, J.D., Panagopoulos, I., Fei, B., Burda, C., 2008. Highly efficient drug delivery with gold nanoparticle vectors for in vivo photodynamic therapy of cancer. Journal of the American Chemical Society 130, 10643-10647.

Cunningham, A.J., 2000. Adjuvant psychological therapy for cancer patients: Putting it on the same footing as adjunctive medical therapies. Psycho-Oncology 9, 367-371.

Curry, D., Scheller, H., Lu, M., Mkandawire, M., Servos, M.R., Cui, S., Zhang, X., Oakes, K.D., 2015. Prevention of doxorubicin sorptive losses in drug delivery studies using polyethylene glycol. RSC Advances 5, 25693-25698.

Daniel, M.-C., Astruc, D., 2004. Gold nanoparticles: Assembly, supramolecular chemistry, quantum-size-related properties, and applications toward biology, catalysis, and nanotechnology. Chemical Reviews 104, 293-346.

Darby, B.L., Le Ru, E.C., 2014. Competition between molecular adsorption and diffusion: Dramatic consequences for sers in colloidal solutions. Journal of the American Chemical Society 136, 10965-10973.

de Oliveira, C., Bremner, K.E., Pataky, R., Gunraj, N., Haq, M., Chan, K., Cheung, W.Y., Hoch, J.S., Peacock, S., Krahn, M.D., 2013. Trends in use and cost of initial cancer treatment in ontario: A population-based descriptive study. CMAJ Open 1, E151-158.

Doane, T., Burda, C., 2013. Nanoparticle mediated non-covalent drug delivery. Advanced Drug Delivery Reviews 65, 607-621.

Duggan, S.T., Keating, G.M., 2011. Pegylated liposomal doxorubicin: A review of its use in metastatic breast cancer, ovarian cancer, multiple myeloma and aids-related kaposi's sarcoma. Drugs 71, 2531-2558.

Dulkeith, E., Morteani, A.C., Niedereichholz, T., Klar, T.A., Feldmann, J., Levi, S.A., van Veggel, F.C.J.M., Reinhoudt, D.N., Möller, M., Gittins, D.I., 2002. Fluorescence quenching of dye molecules near gold nanoparticles: Radiative and nonradiative effects. Physical Review Letters 89, 203002.

Dykman, L., Khlebtsov, N., 2012. Gold nanoparticles in biomedical applications: Recent advances and perspectives. Chemical Society Reviews 41, 2256-2282.

Elbialy, N.S., Fathy, M.M., Khalil, W.M., 2014. Preparation and characterization of magnetic gold nanoparticles to be used as doxorubicin nanocarriers. Physica Medica 30, 843-848.

Fan, C., Zheng, W., Fu, X., Li, X., Wong, Y.-S., Chen, T., 2014. Strategy to enhance the therapeutic effect of doxorubicin in human hepatocellular carcinoma by selenocystine, a synergistic agent that regulates the ros-mediated signaling. Oncotarget 5, 2853-2863.

Farokhzad, O.C., Langer, R., 2009. Impact of nanotechnology on drug delivery. ACS Nano 3, 16-20.

Findlay, M., von Minckwitz, G., Wardley, A., 2008. Effective oral chemotherapy for breast cancer: Pillars of strength. Annals of Oncology 19, 212-222.

Frens, G., 1973. Controlled nucleation for the regulation of the particle size in monodisperse gold suspensions. Nature 241, 20-22.

Gabizon, A., Catane, R., Uziely, B., Kaufman, B., Safra, T., Cohen, R., Martin, F., Huang, A., Barenholz, Y., 1994. Prolonged circulation time and enhanced accumulation in malignant

exudates of doxorubicin encapsulated in polyethylene-glycol coated liposomes. Cancer Research 54, 987-992.

Gabizon, A., Shmeeda, H., Barenholz, Y., 2003. Pharmacokinetics of pegylated liposomal doxorubicin. Clinical Pharmacokinetics 42, 419-436.

Gabizon, A.A., 2001. Pegylated liposomal doxorubicin: Metamorphosis of an old drug into a new form of chemotherapy. Cancer Investigation 19, 424-436.

Gao, J., Huang, X., Liu, H., Zan, F., Ren, J., 2012. Colloidal stability of gold nanoparticles modified with thiol compounds: Bioconjugation and application in cancer cell imaging. Langmuir 28, 4464-4471.

Ghosh, P., Han, G., De, M., Kim, C.K., Rotello, V.M., 2008a. Gold nanoparticles in delivery applications. Advanced Drug Delivery Reviews 60, 1307-1315.

Ghosh, P.S., Kim, C.-K., Han, G., Forbes, N.S., Rotello, V.M., 2008b. Efficient gene delivery vectors by tuning the surface charge density of amino acid-functionalized gold nanoparticles. ACS Nano 2, 2213-2218.

Gottesman, M.M., Fojo, T., Bates, S.E., 2002. Multidrug resistance in cancer: Role of atp-dependent transporters. Nat Rev Cancer 2, 48-58.

Green, A.E., Rose, P.G., 2006. Pegylated liposomal doxorubicin in ovarian cancer. International Journal of Nanomedicine 1, 229-239.

Gupta, P.B., Onder, T.T., Jiang, G., Tao, K., Kuperwasser, C., Weinberg, R.A., Lander, E.S., 2009. Identification of selective inhibitors of cancer stem cells by high-throughput screening. Cell 138, 645-659.

Hall, E.J., Giaccia, A.J., 2012. Radiobiology for the radiologist. Wolters Kluwer Health.

Hall, P., Adami, H.-O., Trichopoulos, D., Pedersen, N.L., Lagiou, P., Ekbom, A., Ingvar, M., Lundell, M., Granath, F., 2004. Effect of low doses of ionising radiation in infancy on cognitive function in adulthood: Swedish population based cohort study. BMJ : British Medical Journal 328, 19-19.

Han, X., Goebl, J., Lu, Z., Yin, Y., 2011. Role of salt in the spontaneous assembly of charged gold nanoparticles in ethanol. Langmuir 27, 5282-5289.

Hanahan, D., Weinberg, R.A., 2000. The hallmarks of cancer. Cell 100, 57-70.

Hanahan, D., Weinberg, R.A., 2011. Hallmarks of cancer: The next generation. Cell 144, 646-674.

Helleday, T., Petermann, E., Lundin, C., Hodgson, B., Sharma, R.A., 2008. DNA repair pathways as targets for cancer therapy. Nat Rev Cancer 8, 193-204.

Herrmann, A., Pratsch, L., Arnold, K., Lassmann, G., 1983. Effect of poly(ethylene glycol) on the polarity of aqueous solutions and on the structure of vesicle membranes. Biochimica et Biophysica Acta (BBA) - Biomembranes 733, 87-94.

Hesketh, P.J., Sanz-Altamira, P., 2012. Aprepitant, dexamethasone, and palonosetron in the prevention of doxorubicin/cyclophosphamide-induced nausea and vomiting. Support Care Cancer 20, 653-656.

Hirano, A., Shiraki, K., Arakawa, T., 2012. Polyethylene glycol behaves like weak organic solvent. Biopolymers 97, 117-122.

Hirsch, L.R., Stafford, R.J., Bankson, J.A., Sershen, S.R., Rivera, B., Price, R.E., Hazle, J.D., Halas, N.J., West, J.L., 2003. Nanoshell-mediated near-infrared thermal therapy of tumors under magnetic resonance guidance. Proceedings of the National Academy of Sciences 100, 13549-13554.

Hojan, K., Milecki, P., 2014. Opportunities for rehabilitation of patients with radiation fibrosis syndrome. Reports of Practical Oncology and Radiotherapy 19, 1-6.

Hrubý, M., Koňák, Č., Ulbrich, K., 2005. Polymeric micellar ph-sensitive drug delivery system for doxorubicin. Journal of Controlled Release 103, 137-148.

Hu, Y., Xie, J., Tong, Y.W., Wang, C.-H., 2007. Effect of peg conformation and particle size on the cellular uptake efficiency of nanoparticles with the hepg2 cells. Journal of Controlled Release 118, 7-17.

Huang, X., El-Sayed, M.A., 2010. Gold nanoparticles: Optical properties and implementations in cancer diagnosis and photothermal therapy. Journal of Advanced Research 1, 13-28.

Hunter, C.A., Sanders, J.K.M., 1990. The nature of .Pi.-.Pi. Interactions. Journal of the American Chemical Society 112, 5525-5534.

Jans, H., Huo, Q., 2012. Gold nanoparticle-enabled biological and chemical detection and analysis. Chemical Society Reviews 41, 2849-2866.

Janssen, M.J.H., Crommelin, D.J.A., Storm, G., Hulshoff, A., 1985. Doxorubicin decomposition on storage. Effect of ph, type of buffer and liposome encapsulation. International Journal of Pharmaceutics 23, 1-11.

Jayasena, S.D., 1999. Aptamers: An emerging class of molecules that rival antibodies in diagnostics. Clinical Chemistry 45, 1628-1650.

Jean, S.R., Tulumello, D.V., Riganti, C., Liyanage, S.U., Schimmer, A.D., Kelley, S.O., 2015. Mitochondrial targeting of doxorubicin eliminates nuclear effects associated with cardiotoxicity. ACS Chemical Biology 10, 2007-2015.

Jeong, S., 2014. The combination of hyperthermia, radiation, and chemotherapy for tumor suppression using hollow gold nanoparticles. International Journal of Radiation Oncology • Biology • Physics 90, S804.

Judson, I., Verweij, J., Gelderblom, H., Hartmann, J.T., Schöffski, P., Blay, J.-Y., Kerst, J.M., Sufliarsky, J., Whelan, J., Hohenberger, P., Krarup-Hansen, A., Alcindor, T., Marreaud, S., Litière, S., Hermans, C., Fisher, C., Hogendoorn, P.C.W., dei Tos, A.P., van der Graaf, W.T.A., 2014. Doxorubicin alone versus intensified doxorubicin plus ifosfamide for first-line treatment of advanced or metastatic soft-tissue sarcoma: A randomised controlled phase 3 trial. The Lancet Oncology 15, 415-423.

Kalluri, R., Weinberg, R.A., 2009. The basics of epithelial-mesenchymal transition. The Journal of Clinical Investigation 119, 1420-1428.

Kataoka, K., Harada, A., Nagasaki, Y., 2001. Block copolymer micelles for drug delivery: Design, characterization and biological significance. Advanced Drug Delivery Reviews 47, 113-131.

Kim, D., Jeong, Y.Y., Jon, S., 2010. A drug-loaded aptamer−gold nanoparticle bioconjugate for combined ct imaging and therapy of prostate cancer. ACS Nano 4, 3689-3696.

Kim, E., Paeng, I.R., 2014. Advantageous sensitivity in the DNA homolog of the rna dopamine aptamer. Journal of Immunoassay & Immunochemistry 35, 83-100.

Knop, K., Hoogenboom, R., Fischer, D., Schubert, U.S., 2010. Poly(ethylene glycol) in drug delivery: Pros and cons as well as potential alternatives. Angewandte Chemie (International ed. in English) 49, 6288-6308.

Kobayashi, H., Watanabe, R., Choyke, P.L., 2014. Improving conventional enhanced permeability and retention (epr) effects; what is the appropriate target? Theranostics 4, 81-89.

Kong, F., Zhang, X., Hai, M., 2014. Microfluidics fabrication of monodisperse biocompatible phospholipid vesicles for encapsulation and delivery of hydrophilic drug or active compound. Langmuir 30, 3905-3912.

Kong, F., Zhang, X., Zhang, H., Qu, X., Chen, D., Servos, M., Mäkilä, E., Salonen, J., Santos, H.A., Hai, M., Weitz, D.A., 2015. Inhibition of multidrug resistance of cancer cells by co-delivery of DNA nanostructures and drugs using porous silicon nanoparticles@giant liposomes. Advanced Functional Materials 25, 3330-3340.

Kronowitz, S.J., Robb, G.L., 2009. Radiation therapy and breast reconstruction: A critical review of the literature. Plastic and Reconstructive Surgery 124, 395-408.

Kumar, A., Mandal, S., Mathew, S.P., Selvakannan, P.R., Mandale, A.B., Chaudhari, R.V., Sastry, M., 2002. Benzene- and anthracene-mediated assembly of gold nanoparticles at the liquid−liquid interface. Langmuir 18, 6478-6483.

Kwon, G., Naito, M., Yokoyama, M., Okano, T., Sakurai, Y., Kataoka, K., 1997. Block copolymer micelles for drug delivery: Loading and release of doxorubicin. Journal of Controlled Release 48, 195-201.

Lamm, A.F., Elaimy, A.L., Lamoreaux, W.T., Mackay, A.R., Fairbanks, R.K., Demakas, J.J., Cooke, B.S., Lee, C.M., 2013. A review of the clinical outcomes for patients diagnosed with brainstem metastasis and treated with stereotactic radiosurgery. ISRN Surgery 2013, 5.

Lasic, D.D., Needham, D., 1995. The "stealth" liposome: A prototypical biomaterial. Chemical Reviews 95, 2601-2628.

Li, D., Wang, Y., Wu, H., Lu, L., Zhang, H., Chang, J., Zhai, Z., Zhang, J., Wang, Y., Zhou, D., Meng, A., 2011. Mitigation of ionizing radiation-induced bone marrow suppression by p38 inhibition and g-csf administration. Journal of Radiation Research 52, 712-716.

Li, X., Ding, L., Xu, Y., Wang, Y., Ping, Q., 2009. Targeted delivery of doxorubicin using stealth liposomes modified with transferrin. Int J Pharm 373, 116-123.

Li, Z., Chen, H., Bao, H., Gao, M., 2004. One-pot reaction to synthesize water-soluble magnetite nanocrystals. Chemistry of Materials 16, 1391-1393.

Liang, C.H., Ye, W.L., Zhu, C.L., Na, R., Cheng, Y., Cui, H., Liu, D.Z., Yang, Z.F., Zhou, S.Y., 2014. Synthesis of doxorubicin alpha-linolenic acid conjugate and evaluation of its antitumor activity. Mol Pharm 11, 1378-1390.

Libutti, S.K., Paciotti, G.F., Byrnes, A.A., Alexander, H.R., Jr., Gannon, W.E., Walker, M., Seidel, G.D., Yuldasheva, N., Tamarkin, L., 2010. Phase i and pharmacokinetic studies of cyt-6091, a novel pegylated colloidal gold-rhtnf nanomedicine. Clinical Cancer Research : An Official Journal of the American Association for Cancer Research 16, 6139-6149.

Liu, B., Huang, P.-J.J., Zhang, X., Wang, F., Pautler, R., Ip, A.C.F., Liu, J., 2013. Parts-per-million of polyethylene glycol as a non-interfering blocking agent for homogeneous biosensor development. Analytical Chemistry 85, 10045-10050.

Liu, J., Liao, S., Diop-Frimpong, B., Chen, W., Goel, S., Naxerova, K., Ancukiewicz, M., Boucher, Y., Jain, R.K., Xu, L., 2012. Tgf-β blockade improves the distribution and efficacy of therapeutics in breast carcinoma by normalizing the tumor stroma. Proceedings of the National Academy of Sciences 109, 16618-16623.

Liu, Z., Sun, X., Nakayama-Ratchford, N., Dai, H., 2007. Supramolecular chemistry on water-soluble carbon nanotubes for drug loading and delivery. ACS Nano 1, 50-56.

Lomax, M.E., Folkes, L.K., O'Neill, P., 2013. Biological consequences of radiation-induced DNA damage: Relevance to radiotherapy. Clinical Oncology 25, 578-585.

Lu, W., Xiong, C., Zhang, G., Huang, Q., Zhang, R., Zhang, J.Z., Li, C., 2009. Targeted photothermal ablation of murine melanomas with melanocyte-stimulating hormone analog-conjugated hollow gold nanospheres. Clinical Cancer Research : An Official Journal of the American Association for Cancer Research 15, 876-886.

Luo, J., Borgens, R., Shi, R., 2002. Polyethylene glycol immediately repairs neuronal membranes and inhibits free radical production after acute spinal cord injury. Journal of Neurochemistry 83, 471-480.

Lv, S., Tang, Z., Li, M., Lin, J., Song, W., Liu, H., Huang, Y., Zhang, Y., Chen, X., 2014. Co-delivery of doxorubicin and paclitaxel by peg-polypeptide nanovehicle for the treatment of non-small cell lung cancer. Biomaterials 35, 6118-6129.

Ma, J., Waxman, D.J., 2008. Combination of antiangiogenesis with chemotherapy for more effective cancer treatment. Mol Cancer Ther 7, 3670-3684.

Maia, J.D.C., Urquiza Carvalho, G.A., Mangueira, C.P., Santana, S.R., Cabral, L.A.F., Rocha, G.B., 2012. Gpu linear algebra libraries and gpgpu programming for accelerating mopac semiempirical quantum chemistry calculations. Journal of Chemical Theory and Computation 8, 3072-3081.

Maruyama, K., Yuda, T., Okamoto, A., Kojima, S., Suginaka, A., Iwatsuru, M., 1992. Prolonged circulation time in vivo of large unilamellar liposomes composed of distearoyl phosphatidylcholine and cholesterol containing amphipathic poly(ethylene glycol). Biochim Biophys Acta 1128, 44-49.

Mayilo, S., Kloster, M.A., Wunderlich, M., Lutich, A., Klar, T.A., Nichtl, A., Kurzinger, K., Stefani, F.D., Feldmann, J., 2009. Long-range fluorescence quenching by gold nanoparticles in a sandwich immunoassay for cardiac troponin t. Nano Lett 9, 4558-4563.

Melancon, M., Lu, W., Yang, Z., Zhang, R., Cheng, Z., Elliot, A., Stafford, J., Olson, T., Zhang, J., Li, C., 2008. In vitro and in vivo targeting of hollow gold nanoshells directed at epidermal growth factor receptor for photothermal ablation therapy. Mol Cancer Ther 7, 1730 - 1739.

Meropol, N.J., Schrag, D., Smith, T.J., Mulvey, T.M., Langdon, R.M., Jr., Blum, D., Ubel, P.A., Schnipper, L.E., 2009. American society of clinical oncology guidance statement: The cost of cancer care. Journal of Clinical Oncology : Official Journal of the American Society of Clinical Oncology 27, 3868-3874.

Mirkin, C.A., Letsinger, R.L., Mucic, R.C., Storhoff, J.J., 1996. A DNA-based method for rationally assembling nanoparticles into macroscopic materials. Nature 382, 607-609.

Mirza, A.Z., Shamshad, H., 2011. Preparation and characterization of doxorubicin functionalized gold nanoparticles. European Journal of Medicinal Chemistry 46, 1857-1860.

Mohan, P., Rapoport, N., 2010. Doxorubicin as a molecular nanotheranostic agent: Effect of doxorubicin encapsulation in micelles or nanoemulsions on the ultrasound-mediated intracellular delivery and nuclear trafficking. Molecular Pharmaceutics 7, 1959-1973.

Mondal, S., Rana, U., Malik, S., 2015. Graphene quantum dot-doped polyaniline nanofiber as high performance supercapacitor electrode materials. Chemical Communications (Cambridge, England) 51, 12365-12368.

Newhouse, R.J., Wang, H., Hensel, J.K., Wheeler, D.A., Zou, S., Zhang, J.Z., 2011. Coherent vibrational oscillations of hollow gold nanospheres. The Journal of Physical Chemistry Letters 2, 228-235.

Nitiss, J.L., 2009. Targeting DNA topoisomerase ii in cancer chemotherapy. Nat Rev Cancer 9, 338-350.

Paciotti, G.F., Kingston, D.G.I., Tamarkin, L., 2006. Colloidal gold nanoparticles: A novel nanoparticle platform for developing multifunctional tumor-targeted drug delivery vectors. Drug Development Research 67, 47-54.

Pagliai, M., Caporali, S., Muniz-Miranda, M., Pratesi, G., Schettino, V., 2012. Sers, xps, and dft study of adenine adsorption on silver and gold surfaces. The Journal of Physical Chemistry Letters 3, 242-245.

Park, H., Yang, J., Lee, J., Haam, S., Choi, I.-H., Yoo, K.-H., 2009. Multifunctional nanoparticles for combined doxorubicin and photothermal treatments. ACS Nano 3, 2919-2926.

Park, J.-W., Shumaker-Parry, J.S., 2014. Structural study of citrate layers on gold nanoparticles: Role of intermolecular interactions in stabilizing nanoparticles. Journal of the American Chemical Society 136, 1907-1921.

Park, J.-W., Shumaker-Parry, J.S., 2015. Strong resistance of citrate anions on metal nanoparticles to desorption under thiol functionalization. ACS Nano 9, 1665-1682.

Prabaharan, M., Grailer, J.J., Pilla, S., Steeber, D.A., Gong, S., 2009. Gold nanoparticles with a monolayer of doxorubicin-conjugated amphiphilic block copolymer for tumor-targeted drug delivery. Biomaterials 30, 6065-6075.

Prados, J., Melguizo, C., Ortiz, R., Velez, C., Alvarez, P.J., Arias, J.L., Ruiz, M.A., Gallardo, V., Aranega, A., 2012. Doxorubicin-loaded nanoparticles: New advances in breast cancer therapy. Anti-cancer Agents in Medicinal Chemistry 12, 1058-1070.

Ramaswamy, S., Tamayo, P., Rifkin, R., Mukherjee, S., Yeang, C.-H., Angelo, M., Ladd, C., Reich, M., Latulippe, E., Mesirov, J.P., Poggio, T., Gerald, W., Loda, M., Lander, E.S., Golub,

T.R., 2001. Multiclass cancer diagnosis using tumor gene expression signatures. Proceedings of the National Academy of Sciences 98, 15149-15154.

Rappe, A.K., Casewit, C.J., Colwell, K.S., Goddard, W.A., Skiff, W.M., 1992. Uff, a full periodic table force field for molecular mechanics and molecular dynamics simulations. Journal of the American Chemical Society 114, 10024-10035.

Ren, Y., Wei, D., 2004. Quantification intracellular levels of oligodeoxynucleotide-doxorubicin conjugate in human carcinoma cells in situ. Journal of Pharmaceutical and Biomedical Analysis 36, 387-391.

Rengan, A.K., Jagtap, M., De, A., Banerjee, R., Srivastava, R., 2014. Multifunctional gold coated thermo-sensitive liposomes for multimodal imaging and photo-thermal therapy of breast cancer cells. Nanoscale 6, 916-923.

Saha, K., Agasti, S.S., Kim, C., Li, X., Rotello, V.M., 2012. Gold nanoparticles in chemical and biological sensing. Chemical Reviews 112, 2739-2779.

Servier, 2016. Servier medical art image bank http://www.Servier.Com/powerpoint-image-bank.

Shan, P., Shen, J.-W., Xu, D.-H., Shi, L.-Y., Gao, J., Lan, Y.-W., Wang, Q., Wei, X.-H., 2014. Molecular dynamics study on the interaction between doxorubicin and hydrophobically modified chitosan oligosaccharide. RSC Advances 4, 23730-23739.

Shukla, R., Bansal, V., Chaudhary, M., Basu, A., Bhonde, R., Sastry, M., 2005. Biocompatibility of gold nanoparticles and their endocytotic fate inside the cellular compartment: A microscopic overview. Langmuir 21, 10644 - 10654.

Singal, P.K., Iliskovic, N., 1998. Doxorubicin-induced cardiomyopathy. New England Journal of Medicine 339, 900-905.

Statistics, C.C.S.s.A.C.o.C., 2015. Canadian cancer statistics. Canadian Cancer Society, Toronto, ON.

Swain, S.M., Kim, S.-B., Cortés, J., Ro, J., Semiglazov, V., Campone, M., Ciruelos, E., Ferrero, J.-M., Schneeweiss, A., Knott, A., Clark, E., Ross, G., Benyunes, M.C., Baselga, J., 2013. Pertuzumab, trastuzumab, and docetaxel for her2-positive metastatic breast cancer (cleopatra study): Overall survival results from a randomised, double-blind, placebo-controlled, phase 3 study. The Lancet Oncology 14, 461-471.

Tomlinson, E., Malspeis, L., 1982. Concomitant adsorption and stability of some anthracycline antibiotics. Journal of Pharmaceutical Sciences 71, 1121-1125.

Veiseh, M., Gabikian, P., Bahrami, S.B., Veiseh, O., Zhang, M., Hackman, R.C., Ravanpay, A.C., Stroud, M.R., Kusuma, Y., Hansen, S.J., Kwok, D., Munoz, N.M., Sze, R.W., Grady, W.M., Greenberg, N.M., Ellenbogen, R.G., Olson, J.M., 2007. Tumor paint: A

chlorotoxin:Cy5.5 bioconjugate for intraoperative visualization of cancer foci. Cancer Research 67, 6882-6888.

Voulgari, A., Pintzas, A., 2009. Epithelial–mesenchymal transition in cancer metastasis: Mechanisms, markers and strategies to overcome drug resistance in the clinic. Biochimica et Biophysica Acta (BBA) - Reviews on Cancer 1796, 75-90.

Wang, F., Liu, B., Ip, A.C.F., Liu, J., 2013. Orthogonal adsorption onto nano-graphene oxide using different intermolecular forces for multiplexed delivery. Advanced Materials 25, 4087-4092.

Wang, F., Wang, Y.-C., Dou, S., Xiong, M.-H., Sun, T.-M., Wang, J., 2011. Doxorubicin-tethered responsive gold nanoparticles facilitate intracellular drug delivery for overcoming multidrug resistance in cancer cells. ACS Nano 5, 3679-3692.

Weinberg, R.A., 2014. The biology of cancer, 2nd ed. Garland Science, Taylor & Francis Group, LLC, New York.

Williams, S.C.P., 2013. Spherical nucleic acids: A whole new ball game. Proceedings of the National Academy of Sciences 110, 13231-13233.

Wood, M.J., Irwin, W.J., Scott, D.K., 1990a. Photodegradation of doxorubicin, daunorubicin and epirubicin measured by high-performance liquid chromatography. Journal of Clinical Pharmacy and Therapeutics 15, 291-300.

Wood, M.J., Irwin, W.J., Scott, D.K., 1990b. Stability of doxorubicin, daunorubicin and epirubicin in plastic syringes and minibags. Journal of Clinical Pharmacy and Therapeutics 15, 279-289.

Wu, D.C., Ofner, C.M., 3rd, 2013. Adsorption and degradation of doxorubicin from aqueous solution in polypropylene containers. AAPS PharmSciTech 14, 74-77.

Yang, H.-W., Liu, H.-L., Li, M.-L., Hsi, I.W., Fan, C.-T., Huang, C.-Y., Lu, Y.-J., Hua, M.-Y., Chou, H.-Y., Liaw, J.-W., Ma, C.-C.M., Wei, K.-C., 2013. Magnetic gold-nanorod/ pnipaamma nanoparticles for dual magnetic resonance and photoacoustic imaging and targeted photothermal therapy. Biomaterials 34, 5651-5660.

You, J., Zhang, G., Li, C., 2010. Exceptionally high payload of doxorubicin in hollow gold nanospheres for near-infrared light-triggered drug release. ACS Nano 4, 1033 - 1041.

Zhang, X.-Q., Xu, X., Lam, R., Giljohann, D., Ho, D., Mirkin, C.A., 2011. Strategy for increasing drug solubility and efficacy through covalent attachment to polyvalent DNA–nanoparticle conjugates. ACS Nano 5, 6962-6970.

Zhang, X., Liu, B., Dave, N., Servos, M.R., Liu, J., 2012a. Instantaneous attachment of an ultrahigh density of nonthiolated DNA to gold nanoparticles and its applications. Langmuir 28, 17053-17060.

Zhang, X., Servos, M.R., Liu, J., 2012b. Instantaneous and quantitative functionalization of gold nanoparticles with thiolated DNA using a pH-assisted and surfactant-free route. Journal of the American Chemical Society 134, 7266-7269.

Zhang, X., Servos, M.R., Liu, J., 2012c. Surface science of DNA adsorption onto citrate-capped gold nanoparticles. Langmuir 28, 3896-3902.

Zhao, C.T., Liu, Z.B., 2014. Application of gold nanoparticles in cancer therapy. Zhongguo yi xue ke xue yuan xue bao. Acta Academiae Medicinae Sinicae 36, 324-329.

Appendix A Supporting Information For Chapter 2

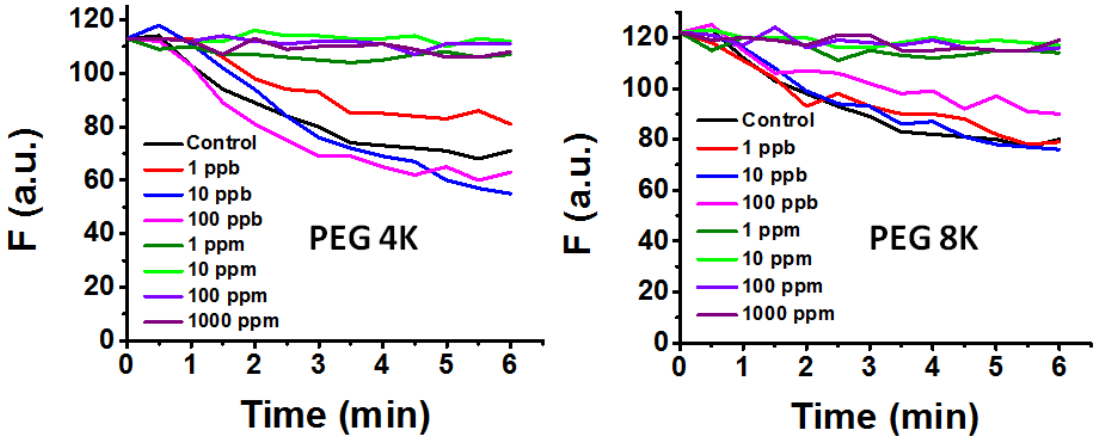

Figure A.1 The effect of PEG 4K and PEG 8K (various concentrations) on DOX adsorption to plate-well surfaces. In control wells, no chemicals other than DOX aqueous solution were added.

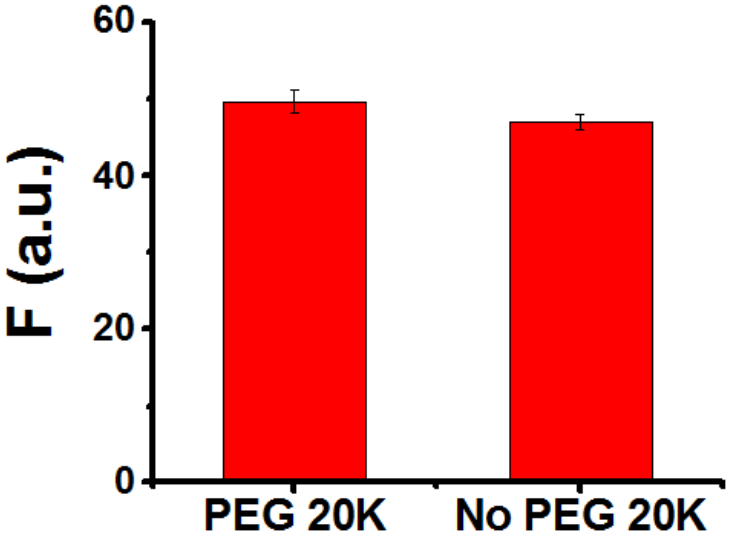

Figure A.2 Comparison of DOX adsorption onto AuNP in the presence and absence of 10 ppm PEG 20K. AuNP-DOX conjugates were dissolved with 2 uL of 1 M KCN solution into 100 uL of AuNP-DOX solution with released DOX quantified by fluorescence. The data demonstrate no significant impact of PEG 20K on DOX loading to AuNP (p=0.065; one-way ANOVA).

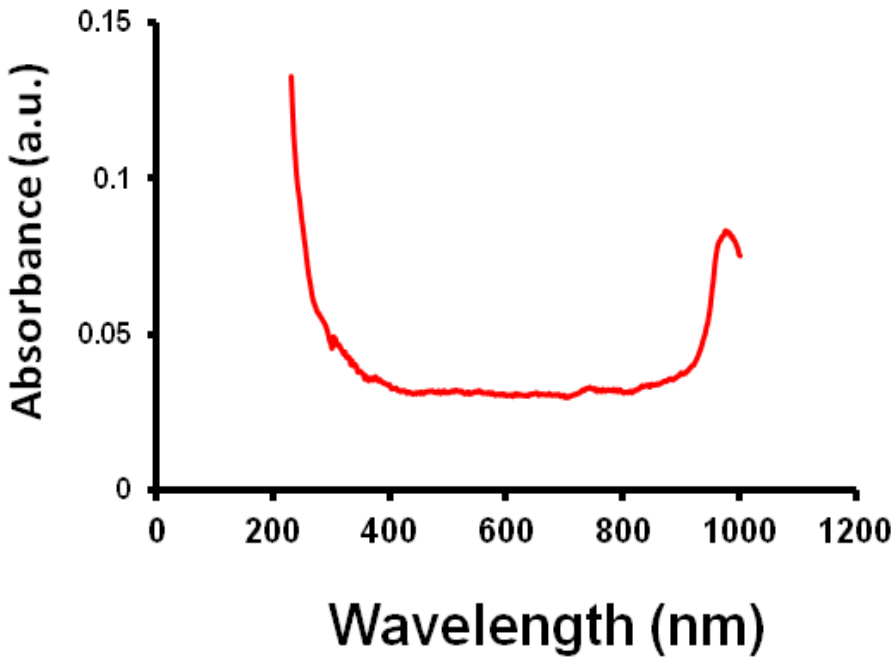

Figure A.3 Optical absorbance of 1% PEG 20K in 5 mM HEPES buffer.

Appendix B Supporting Information for Chapter 3

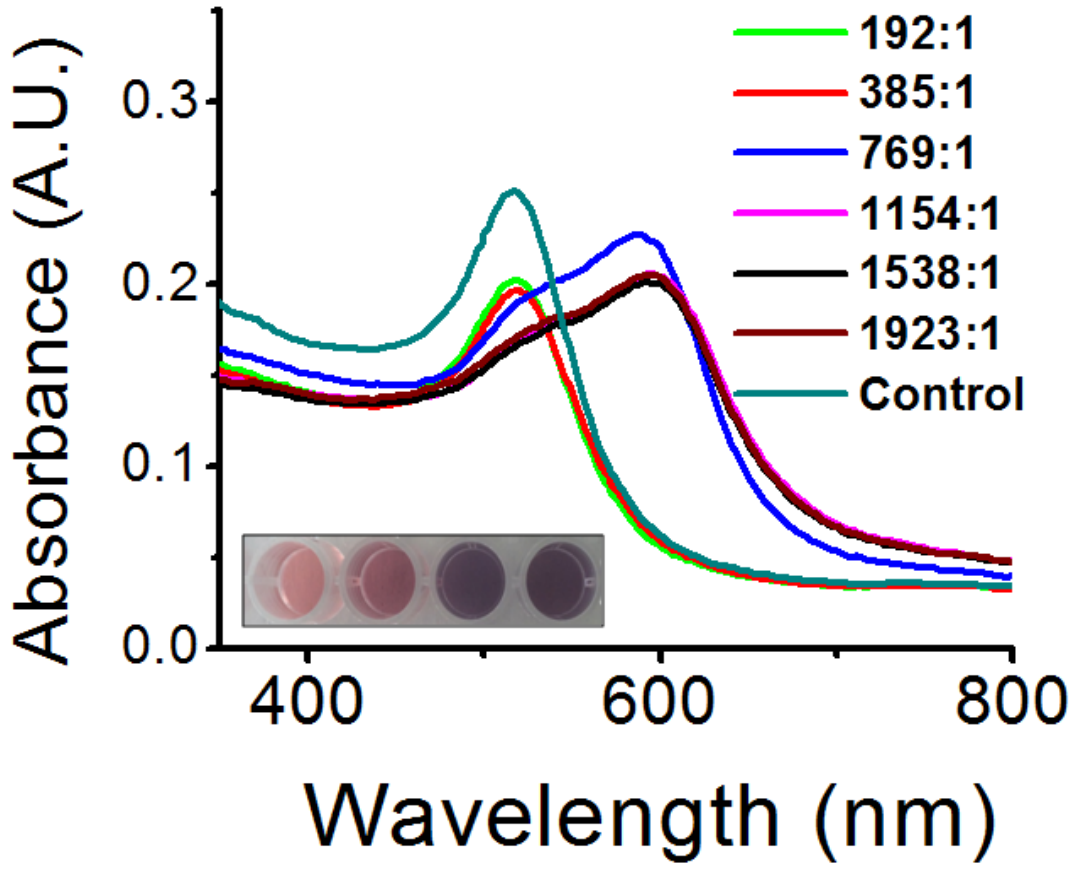

Figure B.1 AuNP absorbance spectra upon addition of increasing [DOX] (Inset: AuNP color change upon addition of DOX, DOX:AuNP molar concentration ratio from right to left: 0, 385, 769, 1538).

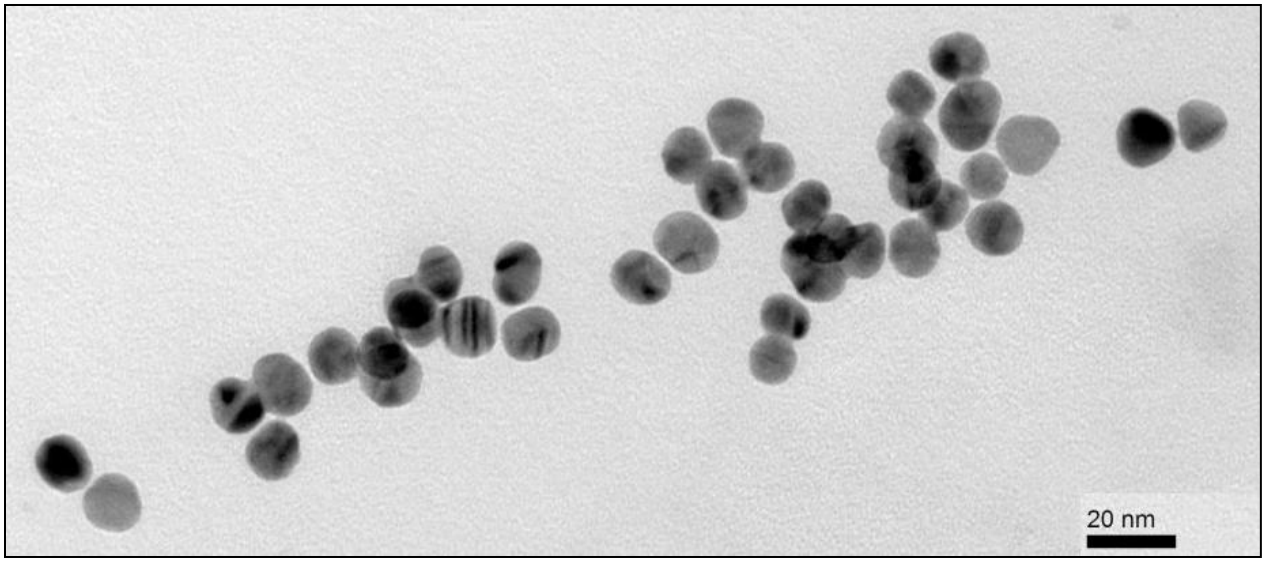

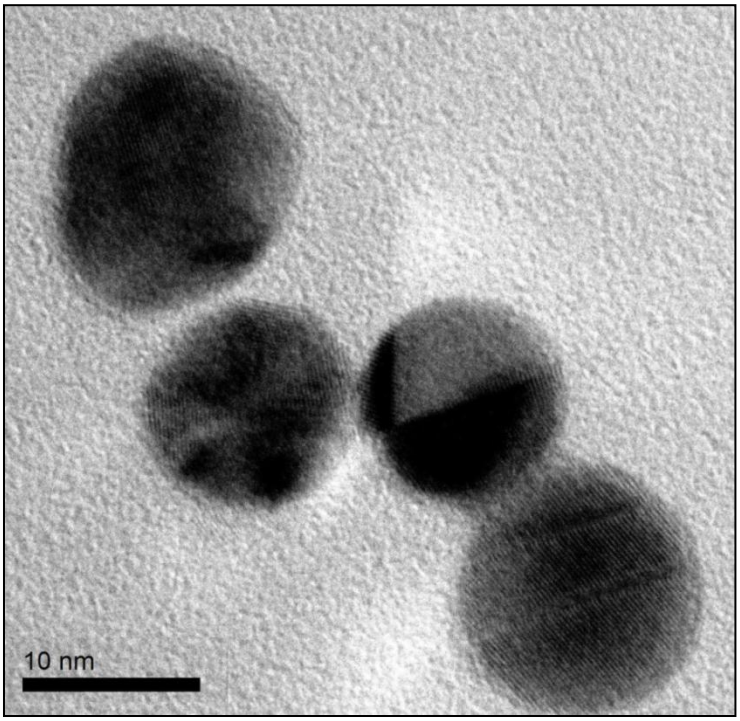

Figure B.2 TEM micrograph of ~13 nm citrate-capped AuNP used in this work using TEM (above) and HR-TEM (bottom). (Scale bars included in figures).

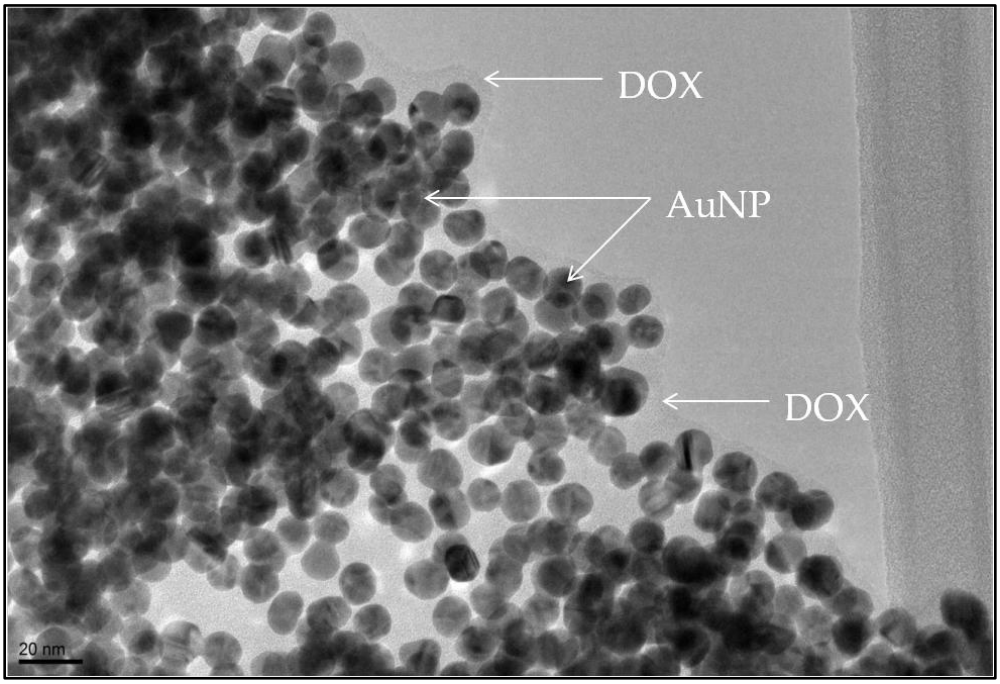

Figure B.3 TEM micrograph of DOX-AuNP conjugates. DOX:AuNP molar concentration ratio = 307:1 (Scale bar: 20 nm).

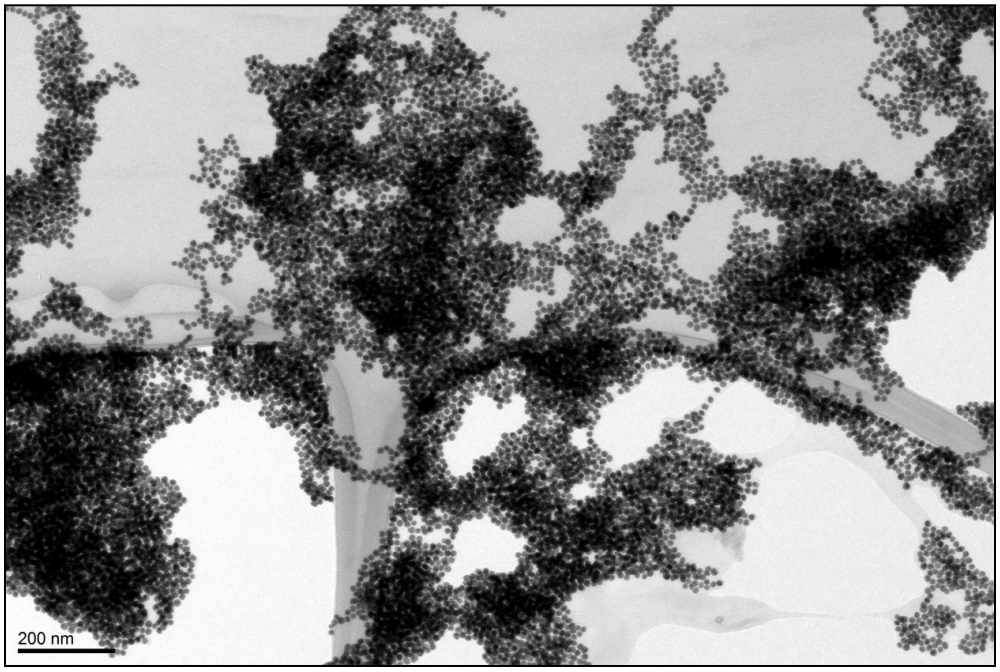

Figure B.4 TEM micrograph of DOX-AuNP conjugates. DOX:AuNP molar concentration ratio = 307:1 (Scale bar: 200 nm).

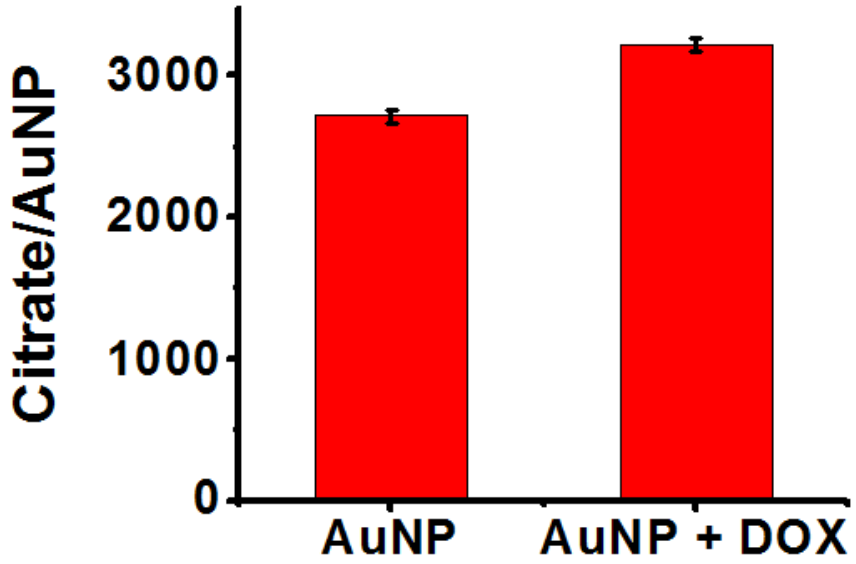

Figure B.5 Citrate displaced per AuNP quantified via DOX fluorescence signal measured in supernatant solution ($p<0.5$).

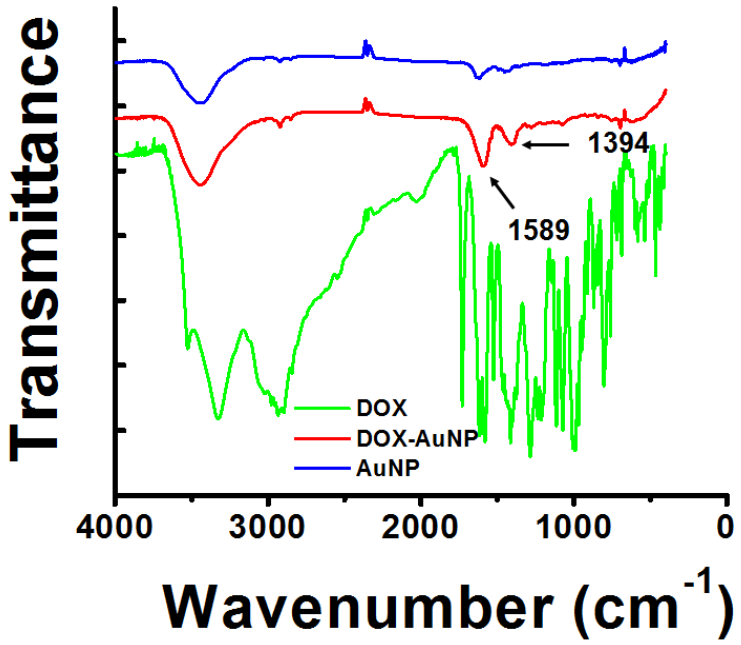

Figure B.6 FTIR spectra of DOX-AuNP conjugate and AuNP.

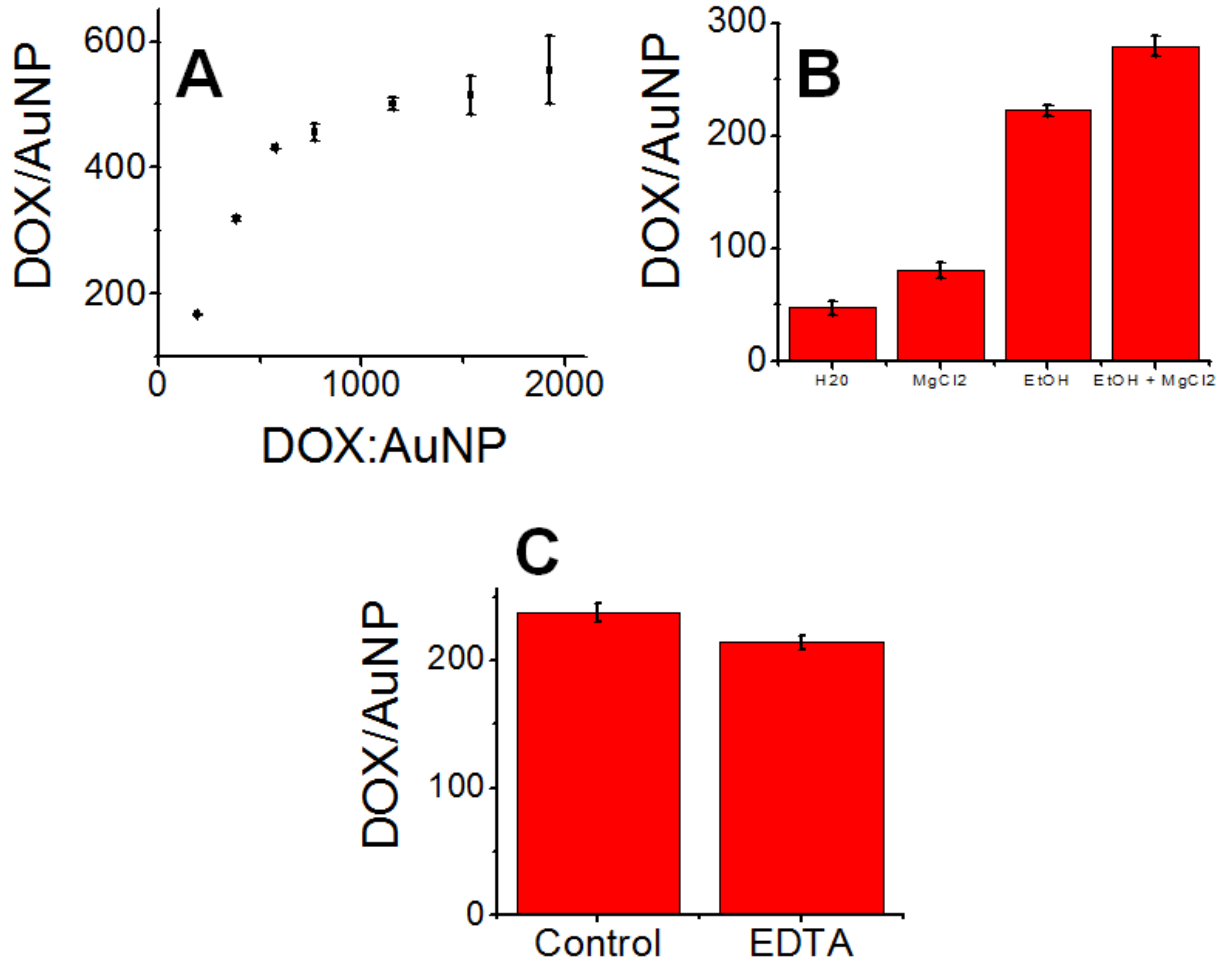

Figure B.7 (A) Original DOX-AuNP loading isotherm including standard error bars. (B) Desorption of DOX from AuNP surface after treatment with MgCl2 ([62.5 mM]), EtOH (31.25% v/v) and EtOH-MgCl2. DOX:AuNP ratio = 317:1. (C) Adsorption of DOX to AuNP surface after EDTA ([3.84 µM]) treatment of AuNP. DOX:AuNP ratio = 308:1.

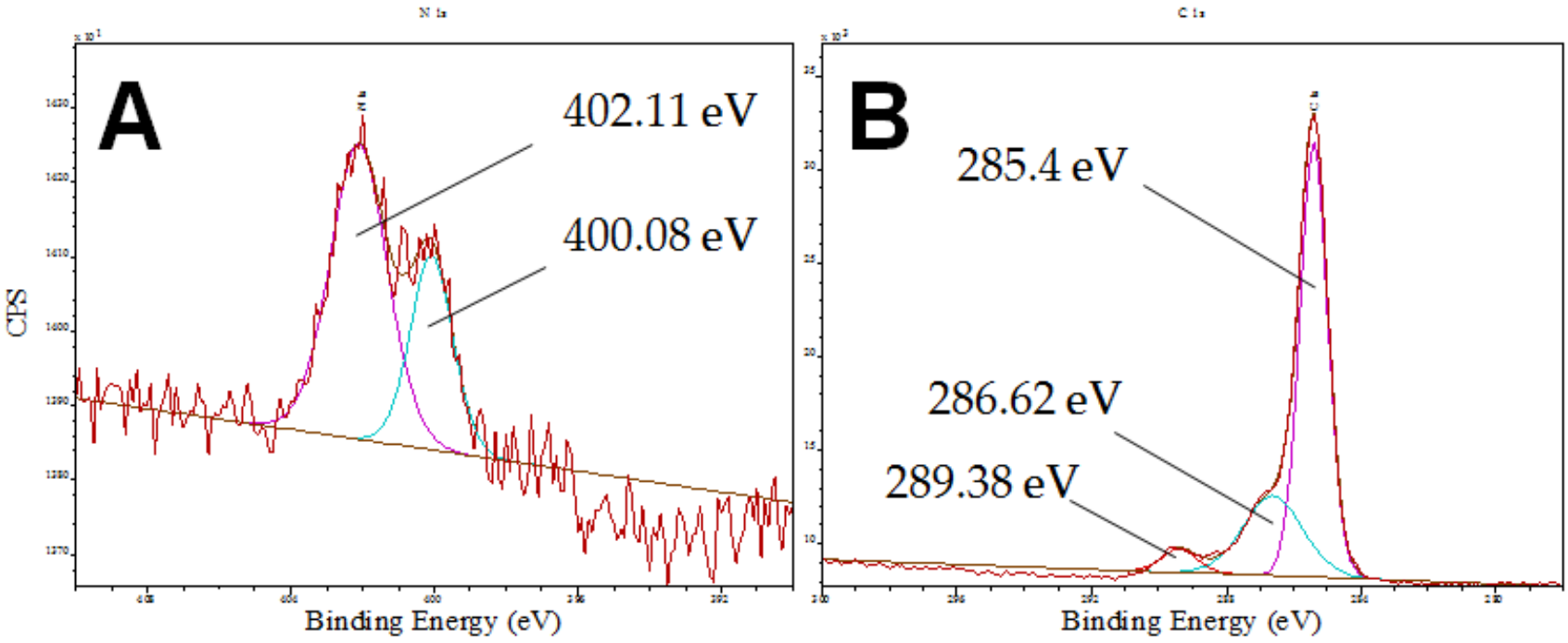

Figure B.8 XPS N 1s (A) and C 1s (B) deconvoluted spectra for DOX-AuNP conjugate solutions.

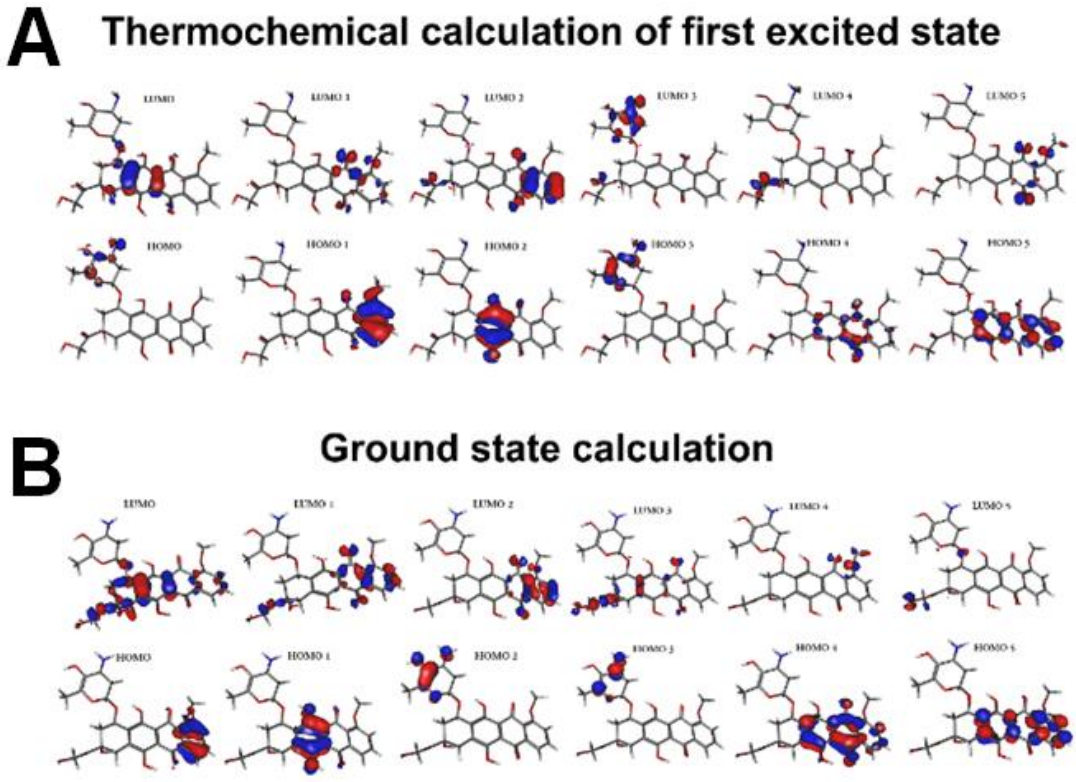

Figure B.9 Molecular orbital (MO) of DOX showing localized electron sites in (A) first excited and (B) ground states. The first excited state is sampled between 200 - 400 °K at the PM7 level of theory in MOPAC2012 with PCM water. The first 6 energy level state of the alpha orbital are displayed. The ground state MO of the HOMO is located at the first benzene ring, which is the highly hydrophobic region of DOX. In contrast, the MO of LUMO is delocalized around the hydrophobic site of DOX. At HUMO 1, the -OH group is involved in MO while in HUMO 4 the carbonyl contributed to the delocalization of the MO. In LUMO 1, the MO was delocalized from the ring 4 containing -OH to the ring 1. However, LUMO 4 MO does not involve a hydrophobic electronic site. This suggests a possible transition that involves either the carbonyl or the hydroxyl functional group. Regarding the particular transition of HOMO 1 to LUMO 1, the MO migrated from -OH site to C=O site. Moreover, the delocalisation of the MO of the hydrophobic site (ring 30) to the acceptor hydrophobic site at the rings 1 and 2. However, HOMO 4 showed a migration of MO from hydrophobic electronic transition to a localized highly electrophilic site. The HOMO 5 displayed the MO delocalised around the hydrophobic electronic sites in ring 1, 2 and 3 towards HOMO 5 localized electrophilic site. The main observation was the absence of MO in ring 5 ground state HOMO to LUMO 5. The thermochemistry calculation demonstrated the contribution of the ring 5 (ether) in the electronic transition is an intra-thermochemistry reaction that involved the amine functional group. As for the ground state, the hydrophobic electronic transitions are partially delocalized.

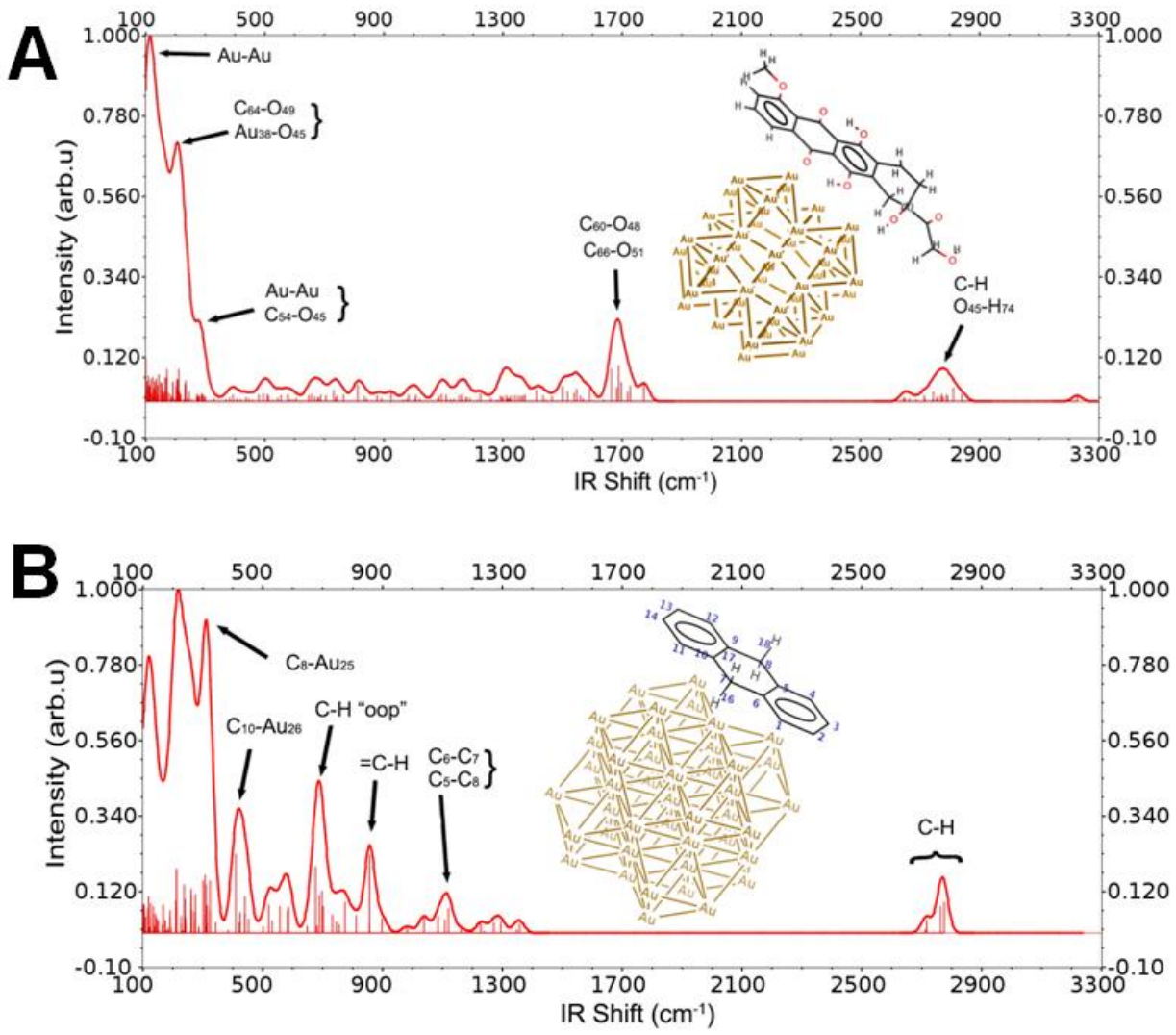

Figure B.10 (A) Modelling of IR spectrum of DOX without ring 1 connected to amine moiety with a 0.5 nm AuNP. (B) Modelling of IR spectrum of the DOX-like anthracene with 0.5 nm AuNP.

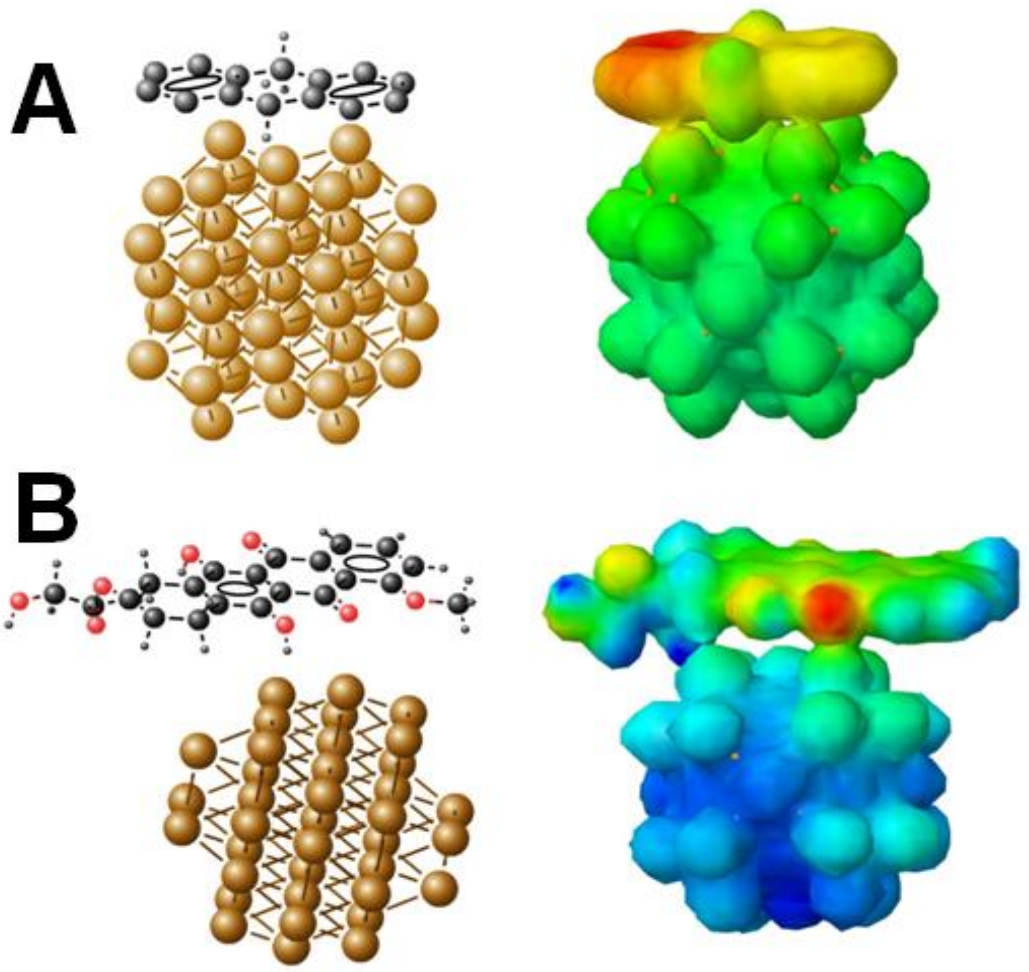

Figure B.11 Calculation of electrostatic potential of the surface at PM7 level of theory: (A) DOX-like anthracene-AuNP, and (B) DOX without ring 1-AuNP. The potential energy surface of the last 1 ns of 12 ns MD demonstrated DOX bent and formed an Au-N bond (Model 1). Further QM calculation of DOX alone with high level of theory in gas phase as well as with continuum water (B3LYP/6-31G(d)) had depicted a bent formation. Increasing the theory level did not change the bend. This highlights the hypothesis that the bent formation between ring 5 containing N and the ring 1 to 4 may be due to the π - σ attraction that dominated the edge to face interaction (Hunter and Sanders, 1990). Therefore, the bending of ring 5 is likely to be independent of the presence of AuNP. To refine the interaction mechanism between DOX – AuNP, we further analyzed two models, model 2 was DOX lacking ring 5, which provided insight of the carbonyl interaction with the AuNP surface.